
Dual Comb Spectroscopy

Birgitta Bernhardt



München 2011

Dual Comb Spectroscopy

Birgitta Bernhardt

Dissertation
an der Fakultät für Physik
der Ludwig–Maximilians–Universität
München

vorgelegt von
Birgitta Bernhardt
aus Erlangen

München, den 20.06.2011

Erstgutachter: Theodor W. Hänsch

Zweitgutachter: Robert Huber

Tag der mündlichen Prüfung: 26.7.2011

Contents

Zusammenfassung	vii
Abstract	viii
List of publications	ix
Conference contributions	x
1. Introduction	1
2. Frequency combs and spectroscopy	5
2.1. The noise equivalent absorption coefficient - a key parameter for comparison	6
2.2. Traditional Fourier transform spectroscopy	7
2.2.1. Principle of Fourier transform spectroscopy	7
2.2.2. Advantages and drawbacks of the traditional Fourier transform spectroscopy	9
2.3. Current topics in spectroscopy	11
2.3.1. Fundamental issues in molecular physics	11
2.3.2. Atmospheric investigations	12
2.3.3. Applications in biology and industry	13
2.3.4. Prevailing requirements in summary	13
2.4. Frequency combs and enhancement cavities	14
2.4.1. Frequency comb principle	14
2.4.2. Different realizations	16
2.4.3. Enhancement cavities	17
2.4.4. Spectroscopy with frequency combs	23
3. Dual comb spectroscopy	27
3.1. Principle	27
3.1.1. The interferogram	29
3.1.2. The interplay between down-conversion, resolution and acquisition time	33
3.2. Initial realization with two erbium frequency combs	36
3.2.1. Setup	36

3.2.2.	Stabilization	39
3.2.3.	Results and discussion	43
3.2.4.	Comparison with traditional Fourier transform spectroscopy	51
4.	Cavity enhanced dual comb spectroscopy in the infrared region	55
4.1.	Improving the sensitivity	55
4.2.	Experimental setup	56
4.2.1.	The ytterbium lasers	57
4.2.2.	The ytterbium amplifier	58
4.2.3.	The enhancement cavity	61
4.3.	Results and discussion	66
5.	Dual comb spectroscopy in the mid-infrared region	71
5.1.	The mid infrared - the molecular fingerprint region	71
5.2.	Experimental Setup	72
5.2.1.	The Cr ²⁺ :ZnSe lasers	73
5.3.	Results and discussion	75
6.	Towards frequency comb Fourier transform spectroscopy in the XUV	79
6.1.	The extreme ultra-violet wavelength region	79
6.1.1.	XUV sources and their spectroscopic applications	80
6.2.	XUV frequency combs via high harmonic generation	82
6.2.1.	The perturbative regime: multi-photon ionization	82
6.2.2.	The non-perturbative regime: the three step model	82
6.2.3.	Scaling laws	84
6.3.	Experimental setup	87
6.3.1.	Second harmonic generation	89
6.3.2.	The green enhancement cavity	90
6.3.3.	The detection apparatus	100
6.4.	Results and discussion	102
6.4.1.	The XUV spectrum	102
6.4.2.	Conclusion	106
7.	Summary and outlook	113
A.	Specifications of the infrared cavity mirrors	117
B.	Specifications of the green cavity mirrors	119
	Curriculum Vitae	138
	Acknowledgments	139

Zusammenfassung

Die vorliegende Arbeit erkundet die Spektroskopie mit zwei Frequenzkämmen (*Dualkamm-spektroskopie*) und demonstriert deren Potential in verschiedenen Wellenlängenbereichen. Dieser neuartige Ansatz verbindet die Eigenschaften optischer Frequenzkämme mit dem Leistungsvermögen klassischer Fouriertransformspektroskopie (FTS), dem bislang vorherrschenden Verfahren in der Molekülspektroskopie.

Ein Dualkammspektrometer basiert auf der Kombination zweier Frequenzkämme mit leicht gegeneinander verstimmter Pulswiederholrate, die in einem interferometrischen Aufbau überlagert werden. Im Gegensatz zu etablierten wellenlängenaufgelösten Messmethoden verzichtet diese neuartige Technologie auf bewegliche Komponenten und erlaubt so eine hohe spektrale Auflösung bei gleichzeitig unerreicht kurzen Messzeiten. Darüber hinaus ermöglicht die Kohärenz und die große spektrale Breite der Frequenzkämme breitbandige Analysen mit gutem Signal-zu-Rausch-Verhältnis ohne zeitliches Mitteln zu erfordern. Optische Frequenzkämme haben aufgrund ihrer möglichen extremen Genauigkeit und Stabilität die Präzisionsspektroskopie revolutioniert. Die Dualkammspektroskopie erlaubt nun erstmals diese Eigenschaften in der Molekülspektroskopie zu nutzen.

Im Rahmen dieser Arbeit wurde ein Dualkammspektrometer basierend auf Erbiumfaserlasern realisiert, das das typische Auflösungsvermögen klassischer FTS von einigen GHz erreicht, obwohl die benötigte Messzeit nur etwa ein Millionstel des dort üblichen Wertes beträgt. Mit der Stabilisierung der Frequenzkämme auf einen Frequenzstandard und durch gezielte Kontrolle der Offsetfrequenz wurde eine Auflösung von 1 MHz erreicht, die für klassische FTS bislang außer Reichweite liegt. Um eine hohe Detektionsempfindlichkeit zu erreichen, wurde der Einsatz eines Überhöhungsresonators demonstriert, der die Wechselwirkung zwischen Laser und gasförmiger Probe erheblich steigert. Dieser Überhöhungsresonator in Kombination mit zwei Ytterbiumfrequenzkämmen erlaubte aufgrund der erreichten Detektionsempfindlichkeit zum ersten Mal die Auflösung der schwachen $3\nu_1$ Oberschwingungen in Ammoniak. Die hier vorgestellten Resultate sind den bisher modernsten Cavity-Ringdown Spektroskopieexperimenten sowohl im Hinblick auf die Empfindlichkeit (etwa 20-fach) und der benötigten Messdauer (etwa ein Hundertstel) erheblich überlegen und lassen die Dualkammspektroskopie so zu einem vielversprechenden Ansatz in der Spurengasanalyse werden.

Für die Untersuchung der starken Molekülgrundschrwingungen, die im mittleren Infrarotbereich liegen, wurde ein weiteres Dualkammspektrometer realisiert, das auf zwei bei 2.4 μm emittierenden $\text{Cr}^{2+}:\text{ZnSe}$ Lasern basiert.

Aus Ermangelung geeigneter Lichtquellen wurde der ultraviolette (UV) Bereich des elektromagnetischen Spektrums bei bisherigen Untersuchungen im wesentlichen ausgeklammert, obwohl er für Moleküle von großem Interesse ist. Um die Fähigkeiten der Dualkammspektroskopie auch in diesem bisher vernachlässigten Wellenlängenbereich anwenden zu können, wurde in der vorliegenden Arbeit ein UV-Frequenzkamm entwickelt, der auf der Erzeugung hoher Harmonischer in einem Überhöhungsresonator beruht. Diese erste Demonstration eines „grünen“ Überhöhungsresonators hat sich als zuverlässige Quelle für UV-Strahlung um 104 und 173 nm im μW -Leistungsbereich erwiesen, die eine kompakte Alternative zu Synchrotronquellen darstellt und ihren baldigen Einsatz als Quelle für Dualkammspektroskopie im UV in Aussicht stellt.

Abstract

This thesis explores *dual comb spectroscopy* and demonstrates its potential in different wavelength regions. This innovative approach combines the properties of optical frequency combs with the capabilities of Fourier transform spectroscopy (FTS), the hitherto leading tool of molecular spectroscopy.

A dual comb spectrometer relies on the combination of two broadband frequency combs with slightly detuned repetition rates joined in an interferometric setup. This novel technique enables the simultaneous achievement of high resolution and short measurement times by abandoning any moving component, so far being a universal necessity for broadband wavelength resolved spectroscopy. Furthermore, the broadband and coherent output of frequency combs also permits high signal-to-noise ratios over the full spectral bandwidth in short measurements without averaging. Optical frequency combs revolutionized precision spectroscopy with their exceptional performance in accuracy and stability. Dual comb spectroscopy for the first time allows the transfer of these unique characteristics to broadband molecular spectroscopy.

An erbium-laser based dual comb spectrometer was realized that achieved typical resolutions of several GHz one million times faster than conventional FTS. Further exploitations of the comb stabilization and controlled tuning of the offset frequency allowed to push the resolution to 1 MHz thereby outperforming any Michelson-based Fourier transform spectrometer. To improve the detection sensitivity, an enhancement cavity was set up that strongly increases the path length the laser interacts with the gas sample under study. The combination of two ytterbium frequency combs with one ring resonator filled with the dilute gas samples achieved an advanced detection sensitivity that for the first time allowed to resolve the weak $3\nu_1$ overtone transitions of ammonia. Outperforming the hitherto state-of-the-art experiment based on cavity ringdown spectroscopy in both sensitivity (20-fold improvement) and measurement time (100-fold improvement), dual comb spectroscopy qualifies therefore for trace gas detection.

Frequency combs primarily emit in the near infrared region where weak overtone bands of molecules are located. The first realization of a dual comb spectrometer with two $\text{Cr}^{2+}:\text{ZnSe}$ lasers emitting at $2.4\ \mu\text{m}$ succeeded in shifting the innovative technique also to the mid infrared region where strong fundamental rovibrational lines are found.

Due to the lack of suitable laser sources for spectroscopy, the ultra violet (UV) wavelength range is rather unexplored. In order to extend dual comb spectroscopy also to this wavelength region, a UV frequency comb has been realized via high harmonic generation in an external build-up resonator. The first implementation of a green enhancement cavity efficiently yielded UV radiation on the μW level at 104 nm and 173 nm, thus presenting a compact alternative to synchrotron sources and holding promise for tabletop UV dual comb spectroscopy in the near future.

Publications during the course of this thesis

Mid-infrared dual-comb spectroscopy with 2.4 μm $\text{Cr}^{2+}:\text{ZnSe}$ femtosecond lasers

B. Bernhardt, E. Sorokin, P. Jacquet, R. Thon, T. Becker, I. T. Sorokina, N. Picqué and T. W. Hänsch, Applied Physics B - Lasers and Optics, Vol. **100**, 3 - 8 (2010)

Cavity-enhanced dual comb spectroscopy

B. Bernhardt, A. Ozawa, P. Jacquet, M. Jacquy, Y., T. Udem, R. Holzwarth, G. Guelachvili, T. W. Hänsch and N. Picqué, Nature Photonics, Vol. **4**, 55-57 (2010)

Power scaling of a high-repetition-rate enhancement cavity

I. Pupeza, T. Eidam, J. Rauschenberger, B. Bernhardt, A. Ozawa, E. Fill, A. Apolonski, Th. Udem, J. Limpert, Z. A. Alahmed, A. M. Azzeer, A. Tünnermann, T. W. Hänsch and F. Krausz, Optics Letters, Vol. **35**, No. 12 (2010)

Implementation and characterization of a stable optical frequency distribution system

B. Bernhardt, T. W. Hänsch and R. Holzwarth, Optics Express, Vol. **17**, 16849–16860, (2009)

Precision spectroscopy of the 3s-3p fine-structure doublet in Mg^+

V. Batteiger, S. Knünz, M. Herrmann, G. Saathoff, H. A. Schüssler, B. Bernhardt, T. Wilken, R. Holzwarth, T. W. Hänsch and Th. Udem, Physical Review A, Vol. **80**, No. 2, (2009)

Towards a precision test of time dilation at high velocity

C. Novotny, B. Bernhardt, D. Bing, G. Ewald, C. Geppert, G. Gwinner, G. Huber, S. Karpuk, H.-J. Kluge, T. Kühl, W. Nörtershäuser, S. Reinhardt, G. Saathoff, D. Schwalm, T. Stöhlker, and A. Wolf, Canadian Journal of Physics, Vol. **87**, 749-756, (2009)

Sub-Doppler laser spectroscopy on relativistic beams and tests of Lorentz invariance

C. Novotny, G. Huber, S. Karpuk, S. Reinhardt, D. Bing, D. Schwalm, A. Wolf, B. Bernhardt, T. Hänsch, R. Holzwarth, G. Saathoff, Th. Udem, W. Nörtershäuser, G. Ewald, C. Geppert, T. Kühl, T. Stöhlker and G. Gwinner, Physical Review A, Vol. **80**, No. 2, (2009)

Absolute frequency measurements and comparisons in iodine at 735nm and 772nm

S. Reinhardt, B. Bernhardt, C. Geppert, R. Holzwarth, G. Huber, S. Karpuk, N. Miski-Oglu, W. Nörtershäuser, C. Novotny and Th. Udem, Optics Communications, Vol. **274**, 354-360, (2007)

Experimental test of special relativity by laser spectroscopy

C. Novotny, C. B. Bernhardt, G. Ewald, C. Geppert, G. Gwinner, T.W. Hänsch, R. Holzwarth, G. Huber, S. Karpuk, H.-J. Kluge, T. Kühl, W. Nörtershäuser, S. Reinhardt, G. Saathoff, D. Schwalm, T. Udem and A. Wolf, Hyperfine Interactions Vol. 171, 57-67

Conference contributions presented by the author

Applications of CEP lasers in spectroscopy: Dual comb spectroscopy (invited talk)

Journée de formation scientifique "Lasers femtoseconde avec contrôle de la phase entre la porteuse et l'enveloppe", Laboratoire Charles Fabry de l'Institut d'Optique, Palaiseau, France (2011)

Green enhancement cavity for frequency comb generation in the extreme ultraviolet (talk)

Conference on Lasers and Electro-Optics (CLEO) 2011, Baltimore, USA, Paper: QTuF3 (2011)

Frequency combs in the XUV (invited talk)

IV International Conference FNP - Frontiers of Nonlinear Physics, Nizhny Novgorod - St. Petersburg, Russia (2010)

Frequency comb Fourier transform spectroscopy with enhancement cavities (invited talk)

PAMO JSM - Colloque commun de la Division Physique, Atomique, Moléculaire et Optique de la Société française de Physique et des Journées de Spectroscopie Moléculaire, Orsay, France (2010)

Trace gas detection with frequency comb Fourier transform spectroscopy (talk)

Conference on Lasers and Electro-Optics (CLEO) 2010, San Jose, USA Paper: CTuS4 (2010)

2.4 μm dual-comb spectroscopy (talk)

Conference on Lasers and Electro-Optics (CLEO) 2010, San Jose, USA Paper: CMJ2 (2010)

Static Fourier transform spectrometers with laser frequency combs (invited talk)

CNES Workshop "New Concepts of high Performance Spectrometers", Toulouse, France (2009)

Frequency comb generation in the XUV regime using a Yb-fiber laser and amplifier system (talk)

Conference on Lasers and Electro-Optics (CLEO) 2009, Baltimore, USA paper: CMN3 (2009)

Enhancement resonators for XUV frequency comb generation (poster)

International Wilhelm and Else Heraeus Summerschool Optical Supercontinua and Frequency Combs, Wittenberg, Germany (2007)

Chapter 1

Introduction

Optical frequency combs revolutionized the field of metrology by enabling the first direct and phase coherent link between measurable radio frequencies (RF) and ultrafast optical frequencies ($\approx 10^{13} - 10^{16}$ Hz) which in contrast have hitherto been too high for detectors or other measuring devices. Since the atomic cesium clock, today's mostly prevalent frequency standard, operates in the RF domain, any arbitrary optical frequency can now be measured and compared with the accuracy of the involved frequency standard¹ permitting unprecedented results in precision spectroscopy [2], time-keeping [3] and satellite navigation [4].

One decade after the invention of the meanwhile highly honored frequency combs (Nobel prize in physics 2005, see [5]), the number of their applications is still growing with the effect of expanding their versatility even further: for example, astronomers are also profiting of the stability and accuracy of the combs in the search for distant earth-like planets in our universe [6]. Another important research field for which frequency combs have become an indispensable tool is spectroscopy, the investigation of interactions between light and matter. It permits conclusions about the (energetic) structure of atoms and the vibrational and rotational behavior of molecules.

Because of its elegant method of down-converting the fast optical frequencies, a technique called Fourier transform spectroscopy has been established for more than 40 years, not only in physics but also in chemistry and environmental research. This essential tool of broadband spectroscopy can record multi-octave spanning spectra with simultaneous high resolution and an accuracy (on the order of 10^{-9}) that up to now had been sufficient for the majority of applications in molecular spectroscopy. With its assistance, a plurality of

¹In the case of the cesium clock, a standard accuracy of 10^{-15} can be obtained. The implementation of optical clocks as general frequency standards would even enable an advanced accuracy of 18 digits [1].

molecular lines of most different species could be obtained in most different wavelength ranges. This made the collection of the high-resolution transmission molecular absorption database (HITRAN) possible, a multitude of molecular line transitions and cross-section data [7]. However, traditional Fourier transform spectroscopy has hardly evolved in the last four decades and is, hence, decreasingly acceptable for today's demands of molecular spectroscopy (see chapter 2).

Because of the incoherent and weak light source that is generally used in conventional devices, the sensitivity of the spectroscopic measurements usually suffer. This was overcome by replacing the white light source of a traditional Fourier transform spectrometer with a frequency comb [8]. Due to the higher brightness of the frequency comb, the recording time of the combined new device could be two orders of magnitude shorter in order to get to the same results as with the traditional setup.

In this proof of principle experiment, the measurement time of 45 minutes was still relatively long and entirely limited by the moving mirror in the setup, which also determined the resolution and the mechanical stability of the device. It is preferable to have a spectrometer with all its noted benefits of broad spectral bandwidth, high resolution and high accuracy but which is additionally fast without the expense of its other features.

This thesis contributed to the development of an innovative spectroscopic tool, the dual comb spectrometer, that shall meet the current requirements of molecular spectroscopy. Chapter 3 explains the new approach including the frequency comb technique and shows how it brings benefits in recording time and resolution.

Chapter 4 explores how it is possible to introduce advanced sensitivity to the novel method by using an enhancement cavity that stores the light pulses for a large amount of round trips and consequently could increase the path length the laser is interrogating with the gas sample.

Frequency combs primarily emit in the near infrared wavelength region (NIR, about 800 - 2000 nm) where weak overtone rovibrational bands of molecules are located. However, traditional Fourier spectroscopy is mainly done in the mid infrared wavelength region (MIR, between 2 and 20 μm) where the strong, fundamental rovibrational molecular lines are located. Chapter 5 summarizes an experiment that aimed for shifting the new dual comb approach to this wavelength region.

The vacuum ultraviolet (VUV, 100 nm - 200 nm) and the extreme ultraviolet wavelength (XUV, 10 nm - 100 nm) range has not yet been explored as much as the NIR and the

MIR wavelength range due to the lack of convenient tabletop laser sources. It is desirable to extend the applicability of the new dual comb spectroscopy technique also to this rather unprobed region. Because of that, a VUV/XUV frequency comb source has been realized within the scope of this thesis in order to establish the innovative new technique of frequency comb Fourier transform spectroscopy in the uncharted high-energy region. The obtained results concerning the VUV/XUV frequency comb source are presented in chapter 6.

Chapter 7 summarizes how the innovative dual comb spectrometer outperforms the traditional technique in terms of measurement time, resolution, accuracy and sensitivity with all results that have been achieved in this thesis and gives a suggesting perspective for future improvements of the existing experiments but also for new implementations in the different wavelength ranges that could be realized in prospective experiments.

Chapter 2

Frequency combs and spectroscopy

The long-established field of spectroscopy could be defined as the research devoted to the interaction of light and matter. Spectroscopy provides numerous possibilities to observe and to understand both chemical and physical phenomena. Spectroscopic experiments help to understand the kinetics of chemical reactions and to comprehend energy propagation through matter.

The huge variety of different spectroscopic techniques (there exist approaches like fluorescence, Raman or nuclear magnetic resonance spectroscopies to mention only a few) prove the importance of this investigative method in physics. One of the oldest and widespread techniques among them is the so-called absorption spectroscopy which compares the power of a light beam before and after the interaction with a sample in a wavelength-resolved manner. Since absorption occurs only when the energy of the photons of the probing light beam matches the energy difference between two states of the material, this method can reveal the energy structure and the composition of matter.

Within the particular scope of this thesis, attention is mainly turned to molecular absorption spectroscopy. In a variety of applications, molecular spectroscopy is playing a crucial role, like in the investigation of atmospheric phenomena. The collection of molecular spectra has a strong assisting impact to all applications that include spectroscopic methods.

Fourier transform spectroscopy has been the fundamental tool in molecular spectroscopy for more than four decades. Since this traditional technique forms the working horse of molecular spectroscopy so far, all technical advancements have originated from this technique and hence, should be compared to it. For a reasonable and generally accepted comparison, a key parameter has to be used for all approaches that takes the most important technical features of the different realizations into account. The so-called noise equivalent absorption coefficient at one second averaging became this parameter since it simultaneously considers such crucial values like signal-to-noise ratio, acquisition time and resolution. After this es-

sential quantity will have been defined in the following chapter, it is followed by a detailed description of the working principle of the traditional Fourier transform spectroscopy with its assets and drawbacks and standard performances. The subsequent section will give some examples that depict some current challenges in molecular spectroscopy which can be overcome by the novel methods that have been developed within the scope of this thesis. The objective of those examples is to highlight why the further development of the traditional technique to new approaches became necessary but it is not an exhaustive discussion about the current challenges. The thesis rather focuses on the innovative developments involving frequency combs (and optional enhancement cavities) whose illustration of their operation and usage conclude this chapter.

2.1 The noise equivalent absorption coefficient - a key parameter for comparison

Before different approaches of absorption spectroscopy will be exemplified, a shared basis has to be found that enables the comparison of the various experiments. The important parameter of the sensitivity is an appropriate candidate for this reference.

The absorption in gases is described by the law of Beer-Lambert. The attenuation of the light is given by the absorbance of the gas sample:

$$I_t(f) = I_i(f) e^{-\alpha(f)L} \quad (2.1)$$

f is the optical frequency, I_i and I_t are the incident and the transmitted intensities, respectively. $\alpha(f)$ is the frequency-dependent absorption coefficient and L is the absorption length, i.e. the effective path length the light is interacting with the gas sample. Assuming only weak absorption allows a Taylor expansion of first order:

$$I_i - I_t \cong I_i \alpha L \quad (2.2)$$

The sensitivity is generally designated as the minimum detectable absorption coefficient α_{min} of a spectral measurement. This coefficient is approximately:

$$\alpha_{min} \cong \frac{1}{L \cdot \frac{S}{N}} \quad (2.3)$$

with $\frac{S}{N}$ being the signal-to-noise ratio: S is the measured signal, equal to I_i and N the noise level. The α_{min} coefficient is generally given in cm^{-1} . The smaller this important value gets the superior is the achieved sensitivity. For an improvement, two solutions exist: first, one can try to increase the absorption length without decreasing the signal-to-noise

ratio. The second attempt would decrease the noise during the data acquisition. In this thesis, the expression *sensitivity* addresses the minimum detectable absorption coefficient α_{min} .

However, the sensitivity, like it just was defined, does still not allow to check different methods of spectroscopy against each other efficiently. This definition does not take into account the different acquisition times that are needed to achieve certain sensitivities. Additional essential characteristic features like the width of the investigated spectral domain or the resolution of the obtained spectra are also missing in this consideration.

A more appropriate way to compare different spectroscopic methods is to look at the so-called *noise equivalent absorption coefficient at a time-averaging of one second* NEA. This parameter is normally given in the units of $\text{cm}^{-1}\text{Hz}^{-1/2}$ and is calculated via the formula:

$$\text{NEA} = \alpha_{min} \cdot \sqrt{T} = \frac{1}{L \cdot \frac{S}{N}} \cdot \sqrt{T}. \quad (2.4)$$

T is the acquisition time of the measurement given in seconds. Even though the NEA includes the detection limit, the measurement time and the investigated spectral width, it does not allow a judgment about the quality or the complexity of the method. Hence, this indicator cannot be considered as the absolute reference for comparison.

2.2 Traditional Fourier transform spectroscopy

The principle of Fourier transform spectroscopy was invented in the late 1950s while its basis, the Michelson interferometer traces back to 1887 [9]. Due to its characteristics, Fourier spectroscopy truly revolutionized the world of scientific instrumentation in the second half of the 20th century. Up to now it is the only approach in spectroscopy that provides broad spectra and high resolution at the same time. Fourier spectroscopy is utilized in all disciplines that deal with the identification of elements or with the understanding of the structure of matter. It allows the implementation of a variety of techniques as for example hyper-spectral imaging, time-resolved or selective spectroscopy. Today, several companies provide commercial Fourier spectrometers that are robust and very user-friendly.

2.2.1 Principle of Fourier transform spectroscopy

The principle of Fourier transform spectroscopy is usually based on a Michelson interferometer as it is depicted in Figure 2.1. By means of this instrument, the high optical frequencies are down-converted to a much lower frequency domain what enables the direct frequency measurement. The reference book *Fourier Transform Infrared Spectrometry* [10] explains the utilized instrument in more detail.

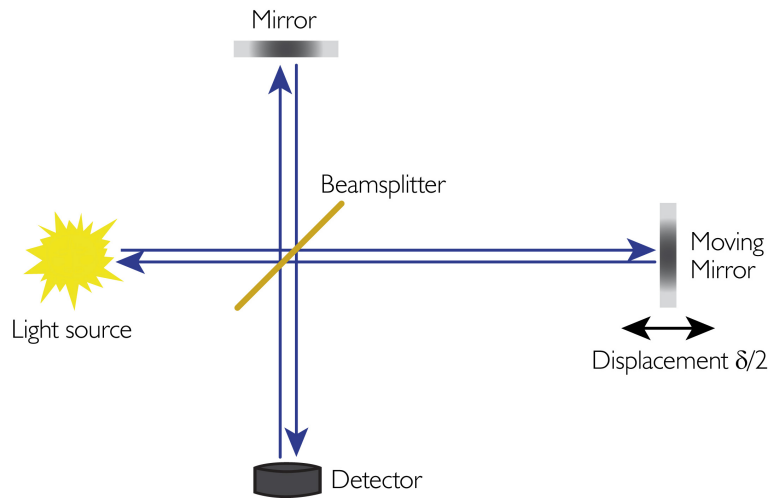


Figure 2.1: Michelson Interferometer. A beamsplitter separates the ray of a light source into two parts. One part is reflected by a fixed mirror, the second part is sent back by a moving mirror. The two beams are recombined again by the beamsplitter. The signal on the subsequent detector is recorded as a function of the mirror displacement δ .

The Fourier spectrometer's principle mode of operation can be explained quickly: The light of a collimated source¹ is split into two parts of equal intensity by a beamsplitter. One of the beams is reflected by a fixed mirror, the second beam is sent back by a mirror on a movable stage. The auxiliary effect of the down-conversion which enables the direct optical frequency measurement occurs due to the Doppler effect induced by the scanning mirror: The part of the light that is reflected by the moving mirror experiences a frequency-shift depending on its energy. Since the Doppler shift is linear with frequency, the red, low energetic fraction of the light is frequency-shifted to a greater extent than the blue, high energetic fraction. The frequency-shifted part is then overlapped by a beamsplitter with the un-shifted part that was reflected by the fixed mirror and sent to a detector that catches the interference signal. This signal is the beat signal between the two arms of the interferometer and hence consists of their difference frequencies that are located in the audio range (since the scanning speed of the mirror is on the order of \approx cm/s) and which are directly accessible with common photo detectors. The spectral characteristics of the incident light can be analyzed by studying the detected interferences as a function of path difference, usually called the interferogram.

For the case of a polychromatic light source, this interferogram can mathematically be

¹This light source is usually an incoherent light source.

represented by the integral

$$I(\delta) = \int_0^{+\infty} \frac{B(f)}{2} [1 + \cos(2\pi f\delta)] df \quad (2.5)$$

Thus, the intensity $I(\delta)$ on the detector is dependent of the mirror displacement δ . $B(f)$ is the spectral intensity of the source and f is the associated optical frequency. In more detail, the interferogram includes a constant part and a fraction that varies with the mirror displacement. The knowledge of the modulated part of the interferogram given by $I'(\delta) = \int_0^{+\infty} \frac{B(f)}{2} \cos(2\pi f\delta) df$ enables to determine the spectrum of the light source by applying the inverse Fourier transformation:

$$B(f) = \int_{-\infty}^{+\infty} I'(\delta) \cos(2\pi f\delta) d\delta. \quad (2.6)$$

In practice, the extension of the optical path difference δ is limited. If we call the maximum path difference δ_{max} , the result obtainable in practice would now be

$$B'(f) = \int_{-\delta_{max}}^{+\delta_{max}} I'(\delta_{max}) \cos(2\pi f\delta) d\delta. \quad (2.7)$$

This limited possibility in mirror displacement results in a finite resolution. The equation (2.7) can equally be written as a convolution:

$$B'(f) = B(f) * F(f) \quad (2.8)$$

while $F(f)$ is the so called instrumental line shape function, the instrument function, or the apparatus function that is in theory proportional to $\text{sinc}(2\pi f\delta)$. The resolution is given by the full width at half maximum of this function, which is $\frac{1}{2\delta_{max}}$. It should be mentioned that the sinc function is inconvenient for spectroscopy because of its large amplitude at frequencies well away from its maximum. These side lobes can perturb the measurement of weak spectral lines. One possibility to circumvent this problem is the use of apodization functions: multiplying the apodization function with the interferogram before the Fourier transformation reduces the amplitude of the side lobes, however, at the expense of the resolution.

2.2.2 Advantages and drawbacks of the traditional Fourier transform spectroscopy

Fourier transform spectroscopy became immediately a real success compared to other approaches like the conventional dispersive spectroscopy because it presents numerous advantages that prove its supremacy. One advantage is the achievable spectral resolution:

with Fourier transform spectrometers (FTS) of good quality the resolving power, i.e. the ratio between the measured optical frequency and the resolution, can reach several millions. This ratio is 10 to 100 times better than for dispersive spectrometers.

Already in 1977 good resolutions of 27 MHz have been demonstrated with an interferometer with a maximum path difference of 6 m [11]. This resolution could be achieved with a reasonable structural dimension because the instrument used a multi-passage system in both interferometer arms. The second advantage is the larger geometrical through-put. Linked to the area of the entrance and exit apertures of the instrument, it gives information on the amount of light transmitted through the instrument. With the Fourier spectrometer, the geometric through-put is increased by a factor of 10 to 100 compared to that which is allowed by a grating spectrometer.

Fourier transform spectrometers also have the multiplex advantage: they allow the measurement of a spectrum with a single detector. The simultaneous recording of millions of spectral elements (= spectral span divided by the optical resolution, $M = \frac{\Delta\nu}{\delta\nu}$) holds a benefit in the signal-to-noise ratio compared to dispersive instruments for similar acquisition times when the noise arising from the detector is dominant. This brings also an advantage of consistency since all spectral elements are measured at the same time interval.

On top of that, also the precision is an essential convenience: since all spectral elements across the entire spectrum are measured simultaneously, the spectrometer allows an uniform calibration of the frequency scale. Moreover, systematic effects induced by the spectrometer are precisely known [12–14].

It shall likewise be mentioned that the Fourier spectrometer has also been utilized for time-resolved spectroscopy (first realization [15]), recording spectra of a broad spectral width with a resolution of $2.5 \times 10^{-3} \text{ cm}^{-1}$ and a temporal resolution of 2 ns [16].

Traditional Fourier transform spectroscopy has become a dominant tool in molecular spectroscopy because of its mentioned advantages, however, its technique has poorly evolved since its invention. The limitation of the Fourier spectrometer is its maximum possible resolution. In theory, the resolution can be arbitrarily fine - but in practice, it depends on the displacement the movable mirror in the interferometer can maximally be scanned. Today most of the FTS are used for vibrational spectroscopy and reach maximum mirror displacements of decimeters in molecular spectroscopy labs. The spectrometers have to reach high enough mirror displacements to resolve the rovibrational lines of the molecules in the gas phase. In the near infrared, less than one meter is enough for the moving mirror to obtain a spectrum with high resolution, i.e. already a Doppler-limited resolution. However, in the far infrared, several meters are necessary. Commercially available spectrometers can provide path differences of up to 10 m (see for instance model *IFS 125HR*

by *Bruker Optics* enabling a resolution of < 30 MHz).

Traditional spectrometers are using incoherent light sources (Halogen, tungsten lamps, etc.). As a result, the sensitivity is limited and hence acquisition times of several minutes to several hours are necessary to record spectra with a high resolution and a higher signal-to-noise ratio of more than 1000.

The investigation of molecules of low energy requires the ability to measure spectra with high resolution. The industrial applications need to be sensitive and compact (for onboard applications on airplanes or satellites for trace gas detection). But because of the geometric through-put of the rays of the incoherent source it is difficult to reach high mirror displacements with a concurrent demand on the instrument's dimensions.

One solution to improve the sensitivity is to increase the interaction between the light and the gas sample. Experiments that work with incoherent light sources often use White-type multi-pass cells [17]. The optical pathlength can reach several tens of meters [18] and sensitivities on the order of 10^{-7} cm^{-1} per spectral element are possible in the mid infrared [19]. However, the improvement of the absorption length in relation to the length of the multi-pass cell stays minor because of the incoherent light source. The resulting large dimensions make the setup inappropriate for onboard applications and, additionally, involve several inconveniences like difficult temperature and pressure controlling of the studied gas.

Today, current developments focus on new means that permit an enhancement of the sensitivity of spectral measurements. The best solution is the implementation of a more powerful light source like using a laser.

2.3 Current topics in spectroscopy

2.3.1 Fundamental issues in molecular physics

Fourier transform spectrometers have yielded significant results in molecular physics, thanks to the increasingly detailed studies of high resolution in all spectral ranges between the ultraviolet and the microwave region. From the fundamental point of view, molecular spectroscopy has a primary objective to investigate the wave functions and energy levels of molecules. The analysis of the spectra (intensity, position, broadening and shape of the lines) can improve the knowledge of the intrinsic structure of molecules and their energy levels. It thus allows to improve, validate or invalidate the existing theoretical models [20]. Molecular physics allows to test the fundamental laws of quantum mechanics on simple and well controlled systems but also to study and understand some of their mechanisms [21–23]. The validation of the symmetrization postulate and of the spin-statistics connection is another example for a possible fundamental test [24–26]. For the evidence of a potential

violation of these postulates, actually forbidden transitions have to be detected which requires a high-grade sensitivity and a broad spectral range. Several experiments already exist trying to demonstrate a physical system in a state of symmetry violating the symmetrization postulate [27, 28].

For these applications, the spectroscopic approaches have to be very sensitive and well-adapted for studying a wide variety of systems. Tunable lasers are generally utilized for these experiments, because they are the most sensitive approaches. However, some spectral regions remain inaccessible due to the technology of tunable lasers and especially the very complex approaches usually cannot investigate different forbidden transitions at the same time. The development of new simple approaches that combine sensitivity, accuracy and other advantages of Fourier spectroscopy would increase the chances of detecting one or more forbidden transitions.

2.3.2 Atmospheric investigations

Planetary atmospheres can also be investigated with the means of spectroscopy. For the interpretation of the atmospheric observations, it is necessary to obtain precise data of the absorption lines but also of the evolution of the line shapes with pressure and temperature. A good example of both an experimental and theoretical problem which has not yet been solved and directly concerns the global warming is the issue of the water vapor continuum [29, 30]. Several explanations exist, however, none of them is yet able to account for all contributing properties of the water vapor continuum [31–33]. In order to progress in understanding the water vapor and to improve the theoretical models, it is necessary to be able to study the profiles of the molecular transitions in the laboratory on a meticulous basis [34]. The various narrow lines can only be detected and distinguished with high resolutions. Since the continuum itself is weak, advanced sensitivities and accuracies in the intensity scale are needed which call for high stability in the measurement.

However, the current most sensitive implementations are unable to produce fast results of broad spectra. Compared to laser spectroscopy, traditional Fourier spectroscopy is either not sensitive enough or quite difficult to operate for the detection of very weak transitions and for the evaluation of their contributions. For example in [35], an effective path length of 800 m had to be utilized.

From a much more applied perspective, since for some years the environmental concerns are current topics of public discussions new projects are developed for the research and analysis of the reactivity of certain pollutants, aerosols or present particulate matter in the atmosphere [36]. These environmental preoccupations also lead to applications in the laboratory. The spectral characterization with high resolution of species such as CH_4 , N_2O ,

H₂O, NO but especially of CO₂ is essential, and a huge work in accumulation of precise and well-interpreted data is necessary. Spectroscopic instruments combining sensitivity, precision and spectral coverage are therefore necessary to accelerate this data accumulation. But also in this research field, the use of tunable lasers is not convenient to perform global studies on all the molecules of interest. On the other hand, the Fourier spectroscopy is not able to achieve the required detection sensitivity or precision in the measurement (for instance, for the CO₂ investigations, a precision in the concentration measurement of 0.3% (1 ppm) is required [37]).

2.3.3 Applications in biology and industry

Besides the applications in fundamental research and planetary investigations, there also exists a variety of applications that are interesting for everyday life. Breath analysis for example is a consolidating term that means the detection of respiratory diseases [38]. The measurement of concentration of ethylene released fruit during storage [39] or the detection of biological agents and explosives [40] could bring helpful insights. From an industrially interesting perspective, impurities in the manufacture of semiconductors can also be detected [41]. These applications benefit from the development of sensitive approaches in laser spectroscopy such as tunable optical parametric oscillators [42] and quantum cascade lasers [43]. As a result of the utilized laser sources and their restricted spectral output, the number of different molecular species that can be analyzed at once is very limited. However, the probe of a human breath, for example, contains over 1000 different biomarkers. Since they are present only in very small amounts, they are susceptible to yield different results about the possible disease. The tools of Fourier spectroscopy are in turn unable to achieve sufficient detection sensitivity. There is currently no spectroscopic method that fulfills all requirements at once. New tools are necessary that allow the trace detection of molecules over a wide spectral range, while they additionally must remain simple to use, not bulky and not expensive to be used multivariably.

2.3.4 Prevailing requirements in summary

In the past decades, the available spectroscopic instruments based on Fourier spectrometers or tunable lasers have helped to meet many requirements, particularly in the field of molecular physics. However, as can be seen in the previous summary of the variable existing applications, the increasingly ambitious demands can no longer be fulfilled by the spectroscopic tools of today. Especially, the simultaneous implementation of the different requirements of sensitivity, accuracy, spectral coverage but also in terms of size, weight and cost makes the evolution of the devices a difficult task.

Overall, for the ideal instrument for a global analysis, there exist a few absolutely indispensable criteria: since a global analysis is of interest, the explorable width of the spectral range is a very important feature. The broader it is, the more different species can be investigated and/or the more different energy levels of one given species can be probed. The instrument should also favor a high resolution. This allows high distinction between the different surveyed species. Another aspect is the sensitivity of the device enabling the detection of very weak transitions or small concentrations. Accuracy of the instrument in terms of frequency and intensity would allow unambiguous identification of the surveyed species and would enable the determination of their concentrations. The ideal spectrometer would furthermore be able to record temporal phenomena, such as the investigation of transient species during chemical reactions. This becomes possible with very short recording times.

As already indicated earlier, frequency combs spread more and more in spectroscopic applications because they seem to meet the mentioned criteria. Before it is possible to completely evaluate their suitability for the current challenges in spectroscopy, the frequency comb principle should be summarized which is the subject of the following section. An overview about different realizations of frequency combs and their spectroscopic implementations, partly including enhancement cavities, will complete the chapter.

2.4 Frequency combs and enhancement cavities

In this work, the optical frequency comb plays an essential role since it is part of each realized experiment that is presented in this thesis. Hence, it is worth to give a description of its working principle in this subchapter. The high number of frequency comb realizations will show how much these lasers are advancing. Recently developed applications will illustrate that the frequency comb became an indispensable tool for laser spectroscopy, especially, the combination of frequency combs with enhancement cavities led to several impressive results.

2.4.1 Frequency comb principle

The development of harmonic frequency chains enabled the first phase-coherent measurement of visible light in 1996. These tools permit to phase-coherently compare an optical signal with a very high frequency (> 100 THz) into the radio frequency domain (MHz) where it can be read out by electronic counters [44]. These frequency chains had two serious drawbacks: first, they could easily fill several laboratories due to their complexity and they could be used to measure only one optical frequency. Both problems were solved with

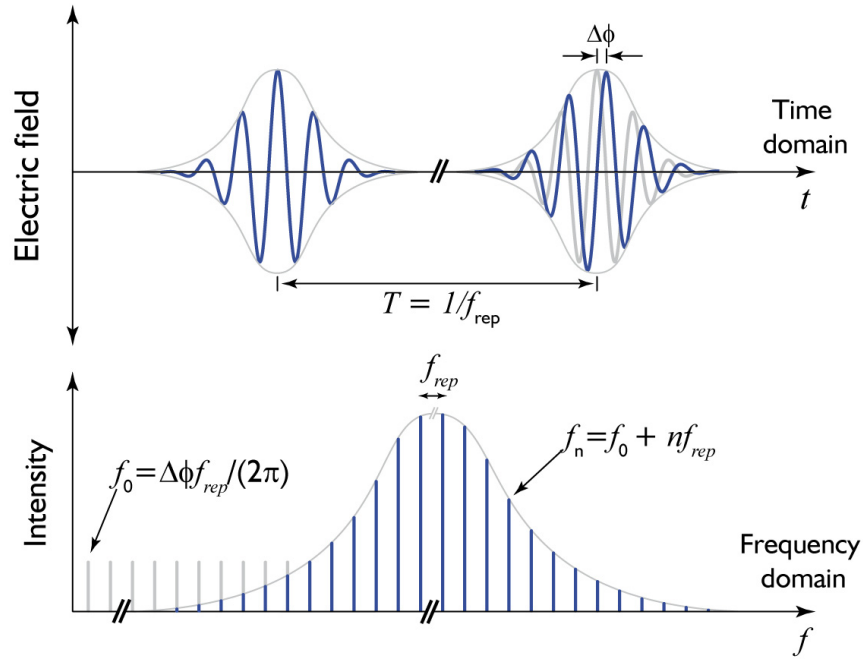


Figure 2.2: The frequency comb: A mode locked laser emits a train of coherent pulses. The pulses are separated by the round trip time T . Two subsequent pulses show a phase shift $\Delta\phi$ between the pulse envelope and the electric field of the pulse. In the frequency domain, the resulting spectrum consists of a large number of equidistant modes separated by the inverse of the round trip time $\frac{1}{T} = f_{rep}$. The phase slippage $\Delta\phi$ causes an offset $f_0 = \frac{\Delta\phi}{2\pi T}$ of the whole comb from zero.

the invention of optical frequency combs because their broad spectral output made out of narrow lines [45, 46].

A single pulse forms a continuous spectrum in the frequency domain. An infinite long train of coherent pulses generates a discrete spectrum reminding of the teeth of a comb in the frequency domain (see figure 2.2). These modes of the frequency comb are equidistant and their interspace equates to the pulse repetition rate f_{rep} [47, 48]. The spectrum of a frequency comb is fully determined if in addition the so called carrier envelope offset frequency f_0 is known. This offset frequency is the result of a constant pulse-to-pulse phase shift between the electric field and the pulse envelope. It shifts the whole frequency comb by a constant factor offset from zero. Hence, each mode of the frequency comb can be expressed by the simple equation:

$$f_n = f_0 + n f_{rep} \quad (2.9)$$

n is a large number of the order of 10^6 . By this equation, two countable radio frequencies f_0 and f_{rep} are linked to an optical frequency f_n .

For a finer grasp of the mode structure of a frequency comb, one can assume a pulse with a carrier frequency f_c circulating in a laser resonator having the length L . The amplitude modulation $A(t)$ of the carrier wave defines the pulse repetition time $T = \frac{1}{f_{rep}}$ by the condition $A(t) = A(t + T)$ while T can be calculated via the group velocity v_g : $T = \frac{2L}{v_g}$. Due to the periodicity of the pulse envelope, the electric field at the laser's output can be written as

$$E(t) = A(t) e^{-i(2\pi f_c)t} + c.c. \quad (2.10)$$

with $c.c.$ being the complex conjugate. Since the envelope function $A(t)$ is periodic, it can be illustrated as Fourier expansion:

$$A(t) = \sum_{m=-\infty}^{\infty} A_m e^{-im(2\pi f_{rep})t} \quad (2.11)$$

Consequently, the electric field (2.10) can be expressed as

$$E(t) = \sum_{m=-\infty}^{\infty} A_m e^{-i2\pi(f_c+m f_{rep})t} + c.c. \quad (2.12)$$

The carrier frequency f_c can be decomposed in l integer multiples of f_{rep} and an offset f_0 (see equation 2.9). This results with a renumeration $n \equiv l + m$ in

$$E(t) = \sum_{k=-\infty}^{\infty} A_k e^{-i2\pi(f_0+n f_{rep})t} + c.c. \quad (2.13)$$

This equation finally represents the electric field of the coherent pulse train that is transmitted by an optical frequency comb. The Fourier transformation of this equation would reveal the shape of the corresponding spectrum in the frequency domain where it forms a comb of laser frequencies separated by f_{rep} . Since frequency combs link radio frequencies with optical frequencies, the accuracy of radio frequency standards like atomic clocks can be transferred to the optical part of the electromagnetic spectrum.

2.4.2 Different realizations

The number of different frequency comb realizations is still growing what proves the importance of this technique which was even honored with the Nobel prize in physics in 2005 [5]. Until recently, Kerr-lens mode-locked Ti:sapphire lasers have been the mostly widespread

frequency comb sources (see for example [47, 48]). Because of their broad emission spectrum (> 300 nm centered at 800 nm), they provide the shortest pulses (< 7 fs). Besides of their high costs, especially for the required pump laser in the green region, the mechanical instability of such lasers is inconvenient for many applications. Moreover, their output power is limited due to thermal lensing effects in the crystal but also by the restricted availability of powerful pump sources.

Fiber lasers are a very special version of bulk lasers that provide a much higher stability [49]. Their setup is more robust and in addition to that, the conversion efficiency of fiber lasers is very attractive (efficiency depending on the doping ratio of the gain fiber; Yb-doped fibers can reach 85 %). Er/Yb-fibers can be pumped by long-living high-power diode lasers what, in combination with the optimum large surface against heating of the fibers, enables higher output power of such fiber based oscillator amplifier combinations compared to the Ti:sapphire precursors. The most popular fiber lasers are erbium and ytterbium-doped fiber lasers emitting around 1550 nm and 1030 nm, respectively. Both models find more and more applications, especially since they are commercially available as user-friendly turn-key systems.

Since frequency combs are versatile devices in laser physics, their field of application should not be only limited to the near infrared region. Hence, both Ti:sapphire and fiber lasers are used to generate frequency combs for instance in the ultra-violet region by high harmonic generation (see for example [50, 51]).

There exist also other bulk materials that are used as the gain media for fs lasers emitting in the mid infrared region. The first realization of a sub-ps oscillator succeeded with a $\text{Cr}^{2+}:\text{ZnSe}$ crystal with a spectrally broad output at $2.4 \mu\text{m}$ [52]. Also other techniques are used for the extension of frequency combs into the mid-infrared region: difference frequency generation [53] or optical parametric oscillation [54].

Finally, there has to be mentioned a quite recent approach of the smallest frequency comb source so far: the so-called micro-toroids [55, 56]. By injecting a cw laser beam into the micro-resonator, a frequency comb is generated due to the very strong confinement of the light inside the resonator that allows the generation of nonlinear effects. These tiny frequency combs can have a broad spectral output of more than 500 nm in the near infrared.

2.4.3 Enhancement cavities

One very important component that was used in one of the presented experiments is the enhancement cavity described in section 4.2.3. This high finesse cavity was mainly used for an improvement of sensitivity in the measurement by increasing the effective pathlength of the laser light inside the chamber. An enhancement cavity can also be used

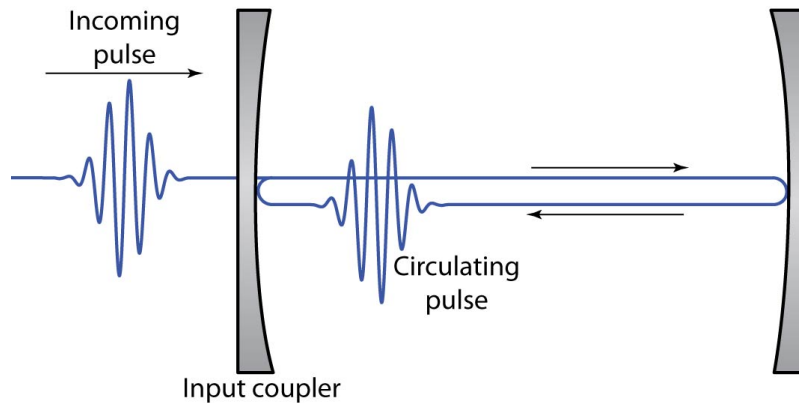


Figure 2.3: For an enhancement inside the cavity, the circulating pulses have to constructively interfere with the incoming pulses. For this purpose, three conditions have to be met at the same time (see text below for details).

for enhancing the laser intensity by introducing a tight focus inside the cavity, for high harmonic generation for instance². This second utilization is described in more detail in chapter 6.

An enhancement cavity mainly consists of well-aligned mirrors causing a closed beam path so that a build-up of the laser light is enabled inside the cavity. One of the mirrors has to be partially transmissive for coupling the driving laser into the cavity. Only certain frequencies and spatial modes are supported by the cavity, generally denoted as longitudinal and transversal cavity modes, respectively. These cavity modes have to be matched well with the optical frequencies of the fs laser in order to get constructive interferences and thereby the build-up in the cavity. Due to e.g. mechanical vibrations, both the laser and the cavity experience permanent changes in their cavity lengths which result in changes in their round-trip phases and hence in their frequency eigenmodes.

Because of the constant exterior disturbances in the laboratory, the frequencies of the laser have to be actively controlled to match the eigenmodes of the cavity, or vice versa. For this purpose, an active feedback loop has to be installed (see section 4.2.3 for its implementation in the experiment). For femtosecond pulses this has already been demonstrated [58]. As already mentioned above, the seeding pulses have to constructively interfere with the pulses already circulating inside the cavity (see figure 2.3) to get the passive enhancement. For an **optimum build-up of the pulses inside the cavity**, three conditions have to be met at once:

1. The pulse shape of the incoming pulses and the pulse shape of the circulating pulses have to be in conformity.

²High finesse cavities can also be found in other applications, as reference cavities for example [57].

2. The incoming pulses have to hit the input coupler at the same time as the circulating pulses are reaching the input coupler.
3. The phase of the electric field of the incoming pulses must be in accordance with the phase of the circulating pulses.

In the frequency domain, one can express these three conditions for **matching the cavity eigenfrequencies to the laser frequencies** the following:

1. The cavity has to feature equidistant frequency eigenmodes.
2. The separation of the cavity eigenmodes and the separation of the frequency comb modes have to be equal.
3. The entire comb has to be shifted properly to overlap with the cavity eigenfrequencies.

These conditions are depicted in figure 2.4. The comb line spacing corresponds to the repetition frequency f_{rep} of the seeding laser. The distances between the cavity eigenmodes are given by the inverse of the cavity round trip time $\frac{1}{T_r}$ and hence also by the length of the cavity. The shift of the entire comb can be accomplished by changing the offset frequency f_0 of the seeding laser. Equidistance of the cavity eigenmodes indicates that the round trip time of the cavity is independent of the laser frequency. This can only be true for zero intra-cavity dispersion. Therefore the three conditions can be fulfilled by the following **checklist for femtosecond enhancement cavities**:

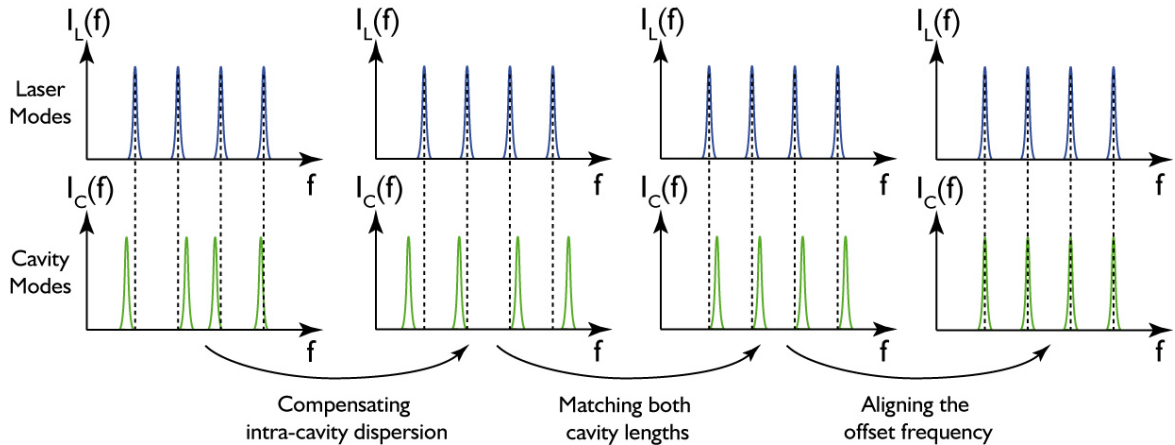


Figure 2.4: The frequency comb modes (blue) and the cavity eigenmodes (green). Three parameters have to be controlled to obtain broadband resonance: Compensating the dispersion of the enhancement cavity results in equidistant cavity eigenmodes. Aligning the cavity length to the length of the laser conforms the mode separation. Adjusting the offset frequency of the seeding laser finally matches all the respective modes.

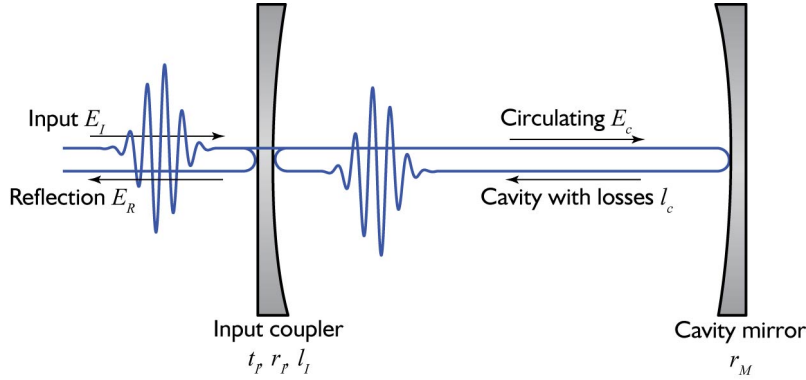


Figure 2.5: Simple cavity consisting of an input coupler and a high reflecting mirror. The field amplitudes of the seeding beam and of the reflected beam are denoted as E_I and E_R , respectively. The laser light is injected into the cavity via an input coupler with a transmission t_I , a reflection r_I and a loss of l_I . Inside the cavity, the field amplitude E_C is decreased after one round trip by a certain amount depending of the cavity losses l_c and the reflectivity of the second cavity mirror r_M .

1. The intra-cavity dispersion has to be zero.
2. The repetition rate f_{rep} of the seeding laser has to be matched to the inverse of the cavity round trip time, $\frac{1}{T_r}$.
3. The offset frequency of the seed laser f_0 has to be adjusted.

Experimentally, the first point of the list can be met by an elaborate design of cavity mirrors that exhibit a dispersion as low as possible or by including chirped mirrors in the cavity that are custom-made in order to compensate for the introduced dispersion. The repetition rate can be controlled for example by a resonator mirror on a piezoelectric transducer and a phase-locked loop [59,60]. The offset frequency finally can be either tuned by the amount of material inserted into the cavity (e.g. by movable wedge plates) [61,62] or by modulating the pump power [63,64].

When all these conditions are satisfied, broadband enhancement is obtained because all frequency comb modes can be coupled into the cavity. A quantitative discussion helps to understand the cavity response in more detail and will give a better insight to the most important parameters of an enhancement cavity like the *impedance matching*, the *Finesse* and the *power enhancement* itself.

For a basic model of a femtosecond enhancement cavity, the most simple case of a two-mirror-cavity is considered (see figure 2.5). The input coupler has a field transmission of

t_I , a field reflection of r_I and a field loss of l_I . Energy conservation predicts that

$$t_I^2 + r_I^2 + l_I^2 = 1 \quad (2.14)$$

must be satisfied. In the following, E_I is the incident field amplitude in front of the cavity, E_C is the field directly behind the input coupler inside the cavity and E_R is the field amplitude reflected by the input coupler, respectively. The field E_C behind the input coupler experiences losses l_C inside the cavity after each roundtrip. After one round trip, its amplitude is decreased to $l_C r_M r_I E_C$. For sake of simplicity, we introduce a factor r that collects - besides all possible cavity losses l_C - also the ones that originate from the high reflector with reflectivity r_M but also the ones caused by any additional cavity mirror besides the input coupler, to only one parameter in order to have a rather general cavity setup. With this new parameter, the field amplitude simplifies to $rr_I E_C$ after one round trip.

In addition, the field is also affected by any dispersive element inside the cavity³. This dispersion affects the round trip phase shift $\phi(f)$ in the cavity:

$$\phi(f) = \frac{2\pi f L_{cav}}{c} + \delta\phi(f) \quad (2.15)$$

L is the cavity length and f the laser frequency, respectively. $\phi(f)$ is separated into two parts: the phase-shift due to free space propagation $\frac{2\pi f L}{c}$ and an additional term $\delta\phi(f)$ that accounts for the possible dispersion inside the cavity. As already mentioned and depicted in the left part of figure 2.4, the cavity dispersion, more precisely the group delay dispersion (GDD) of the cavity, prevents the cavity resonances of being equidistant. This will result in a bandwidth limitation of the cavity enhancement.

Including the general phase information including potential GDD, the field after one round trip decreases to $rr_I e^{i\phi(f)} E_C$. The steady state operation is achieved when the circulating amplitude does not change from one round trip to another, so that

$$E_C = rr_I e^{i\phi(f)} E_C + E_I t_I \quad (2.16)$$

The **power enhancement factor** Q is wavelength dependent and defined to be the ratio between the intra-cavity power and the incident power:

$$Q \equiv \frac{|E_C|^2}{|E_I|^2} \quad (2.17)$$

³Besides any intra-cavity optical component, any introduced gas or the cavity mirrors themselves will also contribute to the total cavity dispersion.

With the conversion of equation (2.16) to $E_I = \frac{E_C}{t_I}(1 - rr_I e^{i\phi(f)})$, the power enhancement Q can also be written as

$$Q = \left| \frac{t_I}{1 - rr_I e^{i\phi(f)}} \right|^2 = \frac{|t_I|^2}{1 + r^2 r_I^2 - 2rr_I \cos(\phi(f))}. \quad (2.18)$$

The power enhancement function forms an Airy-shaped resonance spectrum dependent of the phase shift $\phi(f)$. This phase shift is proportional to the frequency f when the dispersion of the cavity can be neglected. Thus, the Airy-function describes the spectral response of the cavity (the power enhancement function (2.18) is plotted in figure 2.6 with arbitrary mirror parameters). The power enhancement is periodically modulated and it is in resonance when the phase shift is an integer of 2π . On resonance, maximum enhancement can be achieved.

The maximum achievable enhancement does not only depend on the round trip phase but can strongly vary with the choice of the input coupler. The input coupler is characterized by two parameters out of the threesome t_I , r_I and r_I since equation (2.14) determines the input coupler completely. On resonance ($\phi(f) = 0$), equation (2.18) simplifies to

$$Q = \frac{|t_I|^2}{1 + r^2 r_I^2 - 2rr_I} = \frac{|t_I|^2}{(1 - rr_I)^2}. \quad (2.19)$$

In the case of a lossless input coupler, this function has its maximum for

$$T_{IM} \equiv |t_I|^2 = 1 - r^2. \quad (2.20)$$

This means in a simple phrase, maximum enhancement is achieved if the input coupler compensates with its transmission $|t_I|^2$ for all other losses inside the cavity. This favorable case is called **impedance matching**. The impedance matched value for the enhancement factor gets:

$$Q_{IM} = \frac{|1 - r^2|}{(1 - r^2)^2} = \frac{1}{T_{IM}}. \quad (2.21)$$

Besides the power enhancement factor, the so-called **cavity finesse** \mathcal{F} is a widely used characteristic parameter because it quantifies the number of interfering beams inside a cavity and hence the enhancement resonator's performance. It is defined to be the ratio of the free spectral range FSR (i.e. the frequency separation between two resonances $\omega_{FSR} = \frac{2\pi c}{L}$) and the full width at half maximum of a resonance peak $\omega_{FWHM} = 2\pi f_{FWHM}$ (see figure 2.6):

$$\mathcal{F} \equiv \frac{\omega_{FSR}}{\omega_{FWHM}} \quad (2.22)$$

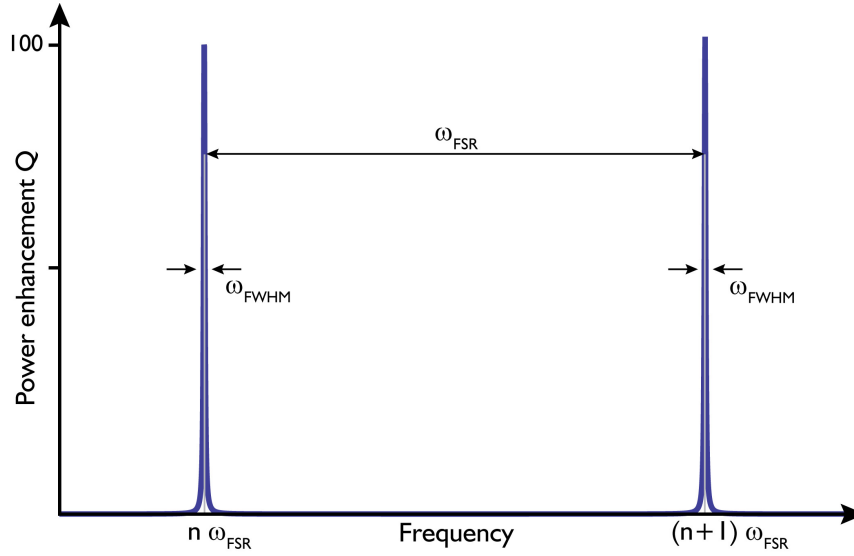


Figure 2.6: The cavity finesse is defined to be the ratio between the cavity's free spectral range ω_{FSR} and the full width at half maximum of the cavity resonances ω_{FWHM} . For the depicted plot, the power enhancement is calculated via formula 2.18 with the transmission/reflexion parameters $t_I = \sqrt{0.01}$ and $rr_I = 0.99$, respectively.

For the special case of an impedance matched high finesse cavity ($r\sqrt{1-t_I^2} \approx 1$), the finesse and the power enhancement factor have the following facile relation:

$$\mathcal{F} \approx \pi Q_{IM} \quad (2.23)$$

For applications that use a cavity as gas cell like it is done in the experiment described in chapter 4, the absorption length L increases compared to a single pass cell that would have the same length as the cavity L_{cav} ⁴:

$$L = Q_{IM} L_{cav} \approx \frac{\mathcal{F} L_{cav}}{\pi} \quad (2.24)$$

2.4.4 Spectroscopy with frequency combs

As already pointed out, frequency combs became essential not only for frequency metrology but also for absorption spectroscopy. The variable experiments in this field show the versatile usage of frequency combs.

⁴Here, a ring cavity is assumed. For the case of a linear cavity the formula would be $L = 2 \cdot Q_{IM} L_{cav} \approx 2 \cdot \mathcal{F} L_{incav} / \pi$, since the resonator length of the linear configuration is usually defined to be the mirror separation and not the round trip length.

As one of the first methods, linear spectroscopy has been realized in 2005 [65]. The principle of these experiments is identical to conventional methods of absorption spectroscopy at one photon, but, here, the innovation is to exchange the tunable laser by a broad frequency comb and to consider each comb mode as a single tunable laser whose frequency is well known. With the broad spectral range of the new source, a single acquisition provides a multitude of different measurements.

Two-photon spectroscopy has also been realized with frequency combs, for example for the study of cesium atoms [66]. As the name already suggests, photon pairs are used in this approach to excite the transition. If the center of the frequency comb is located at half the transition frequency, all comb modes can contribute to the excitation (see for example [67,68] for more details). Frequency combs provide much better accuracy compared to conventional approaches, in the special experimental case of [66], the transition frequencies were measured with a fractional frequency uncertainty of 5×10^{-11} what meant an improvement by a factor of 6 compared to previous results [69]. For two-photon spectroscopy, the use of a source of high spectral width is not as advantageous as for single-photon spectroscopy. Actually, it is preferable to even limit its spectral domain to avoid the detection of single-photon transitions.

Quite different from that, in cavity enhanced direct frequency comb spectroscopy experiments (CE-DFCS) it is tried to probe a broad spectral width. In these experiments, a frequency comb is injected into an enhancement cavity that is used as the gas cell. Since the cavity stores the circulating laser light, it advances the direct absorption of the laser light by the interaction with the gas probe. The higher the cavity finesse gets, the longer the interaction pathlength grows which in turn improves the sensitivity of the method. At the same time, it is favorable to have broadband cavity mirrors in order to expand the enhancing effect to the full range of the injected frequency comb to have the most possible information about the absorption of the probe. For a spectrally resolved measurement, an additional element has to be implemented behind the cavity that enables a wavelength-selected analysis. As a result, the measurement time can become quite long, especially for broad spectra and for high resolution measurements since spectrally resolved measurements usually involve scanning components.

One demonstration of the CE-DFCS was realized with the most simple wavelength-tuning element, a grating-based spectrometer [70]. This cavity ringdown spectroscopy experiment used a cavity with a finesse of 4500 what resulted in a theoretically possible simultaneous readout of 100 nm. But due to the utilized spectrograph, only a single-shot acquisition of a 15 nm broad spectrum at 25 GHz resolution was enabled. In addition to that, the ringdown decay was resolved by a scanning mirror that limited the acquisition time to 1.4 ms due to its scanning frequency of 355 Hz. This all together resulted in an α_{min} of

$6.3 \times 10^{-7} \text{ cm}^{-1}$ and a NEA of $2.4 \times 10^{-8} \text{ cm}^{-1}\text{Hz}^{-1/2}$, respectively.

The ensuing experiments aimed at improving the resolution in different ways (see for example [71,72]). The so-called comb Vernier spectrometer contains the same basic components, just adds time as a second dimension to increase the spectral resolution. An intentional mismatch of the laser's repetition rate and the cavity free spectral range FSR results in an effective filtering of the original comb structure [73]. This detuning of the cavity additionally circumvents the issue of the cavity dispersion. However, since also for this technique, a scanning component (detuning the cavity FSR against the laser repetition frequency) has to be implemented, the acquisition time is also in this case on the order of milliseconds (10 ms) while having a resolution of 30 GHz. The absorption sensitivity is $5 \times 10^{-6} \text{ cm}^{-1}$.

A realization with a virtually imaged phase array (VIPA) succeeded in exceeding previously reached resolutions [74]. By the combination of the VIPA and a grating, a resolution of 3 GHz was achieved.

Some already mentioned drawbacks of the traditional Fourier transform spectroscopy could also be overcome with the help of frequency combs: By exchanging the commonly used incoherent light source in the FT spectrometer by a frequency comb, the acquisition time, the signal-to-noise ratio and the detection sensitivity could be improved at once [8]. Additionally, the self-calibration of the frequency scale due to the reference laser feature of the comb is an additional benefit. However, the use of lasers as sources does not solve all limitations, the resolution and measurement time are still mainly determined by the moving mirror in the interferometer.

In fact, all the experiments presented here have scanning components in common that determine the acquisition time. The combination of two frequency combs (modulated by electro-optical modulators with different modulation frequencies proposed by Lee et al. in 2001 [75], or with slightly detuned repetition rates proposed by Schiller in 2002 [76]) revolutionized the acquisition time without affecting the other important parameters like broad bandwidth, compactness and resolution. In fact, the resolution could be even further improved. The following chapter enters into the innovations and improvements concerning the new spectroscopy method, often called multi-heterodyne spectroscopy [77].

Chapter 3

Dual comb spectroscopy

3.1 Principle

The combination of two frequency combs in an interferometric setup is a novel approach of Fourier transform spectroscopy that introduced a new generation of fast and sensitive high-resolution spectrometers with broad spectral bandwidth circumventing the requirement of scanning components for the spectral resolution. The novel method with two frequency combs has been proposed by Schiller in 2002 [76]. Like a traditional Fourier transform spectrometer, this approach is based on the principle of down-converting optical frequencies, but in a completely innovative static manner. The first realization succeeded in 2005 by Keilmann et al. in the mid-infrared region by the means of optical rectification. After that, a few experimental demonstrations followed between 2005 and 2008 [77–80], culminating in a resolution of the comb linewidth of 91 kHz [77]. In 2008, an implementation with two stabilized frequency combs was also accomplished within the collaboration of the group of Nathalie Picqué from the *Laboratoire de Photophysique Moléculaire du Centre National de la Recherche Scientifique, Orsay, France*, and the Laser Spectroscopy Division of Prof. Theodor W. Hänsch at the *Max-Planck-Institut für Quantenoptik* in Garching, Germany. The achieved resolution of the comb lines outperformed all precedented results so far by two orders of magnitude down to 2.3 kHz [81].

The principle of the experiment, shown schematically in figure 3.1, involves two sources of frequency combs with slightly different repetition frequencies. At least one of the two sources probes the gas sample under study. Afterwards, it is overlapped with the second frequency comb by a beam combiner. This produces a comb in the radio frequency domain which can be detected with a common photo diode. The signal of the detector output is a

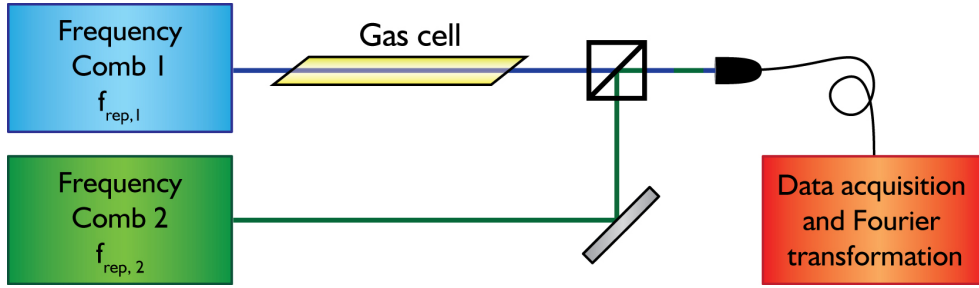


Figure 3.1: Principle of Fourier transform spectroscopy with two frequency combs: One frequency comb is sent through a gas cell filled with the sample and afterwards overlapped with a second frequency comb with a slightly different repetition rate. The interference down-converts the optical frequencies to radio frequencies that are measurable with a common photo diode. After data acquisition and Fourier transformation of the interferogram, the absorption spectrum of the gas is revealed.

function of time and is called the interferogram. The spectrum containing the absorption information of the gas sample is obtained by applying a Fourier transform algorithm to this signal.

Going more into detail will help to fully grasp the structure of the interferogram itself and its included spectral information about the gas sample.

The two utilized frequency combs possess slightly different repetition rates $f_{rep,1}$ and $f_{rep,2}$, respectively. As already shown in equation 2.9 in the subchapter 2.4.1, the modes of the frequency combs can be expressed with the simple relation $f_{n,k} = f_{0,k} + n f_{rep,k}$ with the numbering $k = [1, 2]$ representing either the first or the second frequency comb. The repetition rates are slightly detuned, let's assume $f_{rep,1} > f_{rep,2}$ for sake of simplicity. The relation of the repetition frequencies can be written as (see figure 3.2):

$$f_{rep,1} = f_{rep,2} + \delta \quad (3.1)$$

The overlap of the wave fronts on a photo detector generates a beating signal between all optical modes of both frequency combs. If only the beat signals between the teeth of the same order n are considered, the frequency of each beat can be written as

$$\begin{aligned} f_{n,1} - f_{n,2} &= [f_{0,1} + n f_{rep,1}] - [f_{0,2} + n f_{rep,2}] \\ &= [f_{0,1} - f_{0,2}] + n [f_{rep,1} - f_{rep,2}] \\ &= [f_{0,1} - f_{0,2}] + n \delta \end{aligned} \quad (3.2)$$

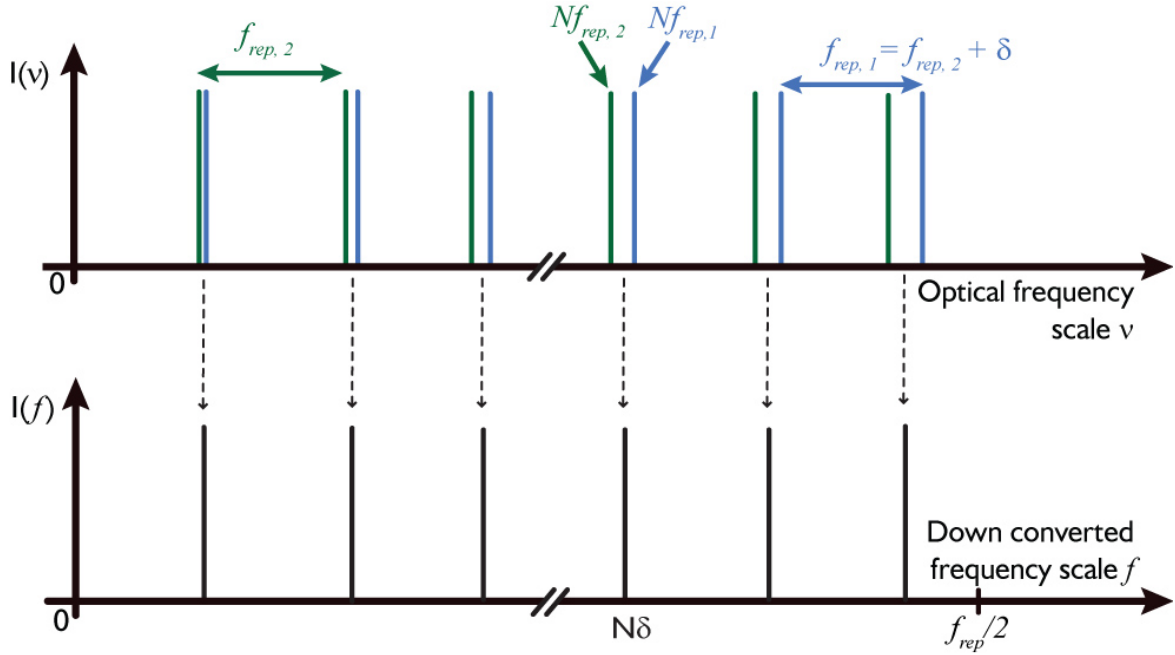


Figure 3.2: Downconversion of the optical frequencies. Two frequency combs with different repetition rates $f_{rep,1}$ and $f_{rep,2}$ are overlapped and form a beating signal that is a comb in the radio frequency domain. Hence, the optical frequencies are down-converted to radio frequencies by the scaling factor a that is dependent of the detuning of the combs' repetition rates.

The difference in repetition rates δ is chosen with the objective that all beat notes $f_{n,1} - f_{n,2}$ are lying in the radio frequency domain so that they can be detected with a photo diode with appropriate bandwidth. The down-conversion coefficient for the optical frequencies is usually called scaling factor and is given by:

$$\begin{aligned}
 a &= \frac{f_{rep,1} - f_{rep,2}}{f_{rep,1}} \\
 &= \frac{\delta}{f_{rep,1}}
 \end{aligned}
 \tag{3.3}$$

3.1.1 The interferogram

When the two frequency combs are superimposed and interact, many beat frequencies appear. In fact, each of the comb mode beats with each other comb mode, and generate a new frequency. One advantage of the frequency combs as light source for the spectrometer is the ability to control the frequency position of the comb modes. It is therefore possible

to choose the value of the down-converted frequencies. By that, an image of the optical spectrum of two lasers is produced in a field where the frequencies are easily measured using electronic instruments. As already noted in equation 2.13, the electric field of a frequency comb can be written as a superposition of plane monochromatic waves:

$$E_k(t) = \sum_n A_{n,k} e^{-i(2\pi f_{n,k})t} + c.c. \quad (3.4)$$

$A_{n,k}$ is the amplitude of the n -th mode of the comb source k and *c.c.* is the common abbreviation of the conjugate complex.

The first frequency comb passes through a gas cell and experiences both attenuation and phase shift due to absorption and dispersion in the gas sample. This interaction can be written as $e^{-\alpha(f)-i\phi(f)}$ where $\alpha(f)$ is the amplitude attenuation at the frequency f and $\phi(f)$ is the phase shift of the electric field, respectively. The electric field of the first frequency comb behind the gas cell is therefore:

$$E_1(t) = \sum_n A_{n,1} e^{-\alpha_{n,1}-i\phi_{n,1}} e^{-i(2\pi f_{n,1})t} + c.c. \quad (3.5)$$

Here, $\alpha_{n,1}$ and $\phi_{n,1}$ are the attenuation and the phase shift, respectively, that laser 1 experiences at a given frequency f_n . The two frequency combs are overlapped and the electric fields of the two sources sum up to:

$$E_1(t) + E_2(t) = \sum_n [A_{n,1} e^{-\alpha_{n,1}-i\phi_{n,1}} e^{-i(2\pi f_{n,1})t} + A_{n,2} e^{-i(2\pi f_{n,2})t}] + c.c. \quad (3.6)$$

The photo detector records a signal with the intensity:

$$S(t) \propto [E_1(t) + E_2(t)] \times [E_1(t) + E_2(t)]^* \quad (3.7)$$

This term is quite complex since all frequency comb modes of source 1 can beat with all modes of the source 2. For a better understanding of the different frequency components in the interferogram, we only consider a beat between only one comb tooth n of source 1 with one comb tooth n of comb 2 is considered:

$$\begin{aligned} S_{n,n}(t) &\propto \sum_n [A_{n,1} e^{-\alpha_{n,1}-i\phi_{n,1}} e^{-i(2\pi f_{n,1})t} + A_{n,2} e^{-i(2\pi f_{n,2})t}] \\ &\times [A_{n,1} e^{-\alpha_{n,1}+i\phi_{n,1}} e^{i(2\pi f_{n,1})t} + A_{n,2} e^{i(2\pi f_{n,2})t}] \\ &\propto \sum_n A_{n,1}^2 e^{-2\alpha_{n,1}} + A_{n,2}^2 + 2A_{n,1}A_{n,2} e^{-\alpha_{n,1}} \cos[2\pi(n\delta + f_{0,1} - f_{0,2})t + \phi_{n,1}] \end{aligned} \quad (3.8)$$

In this expression, only the last summand is of interest because it distinguishably contains all the spectral information of the surveyed sample (the first summand also contains the spectral information but the full information is projected onto zero frequency and is, hence, not resolvable). The sum over n of this term forms one sample of the interferogram at time t . These frequencies are the ones of the first optical frequency comb which probes the gas sample, down-converted by the factor a (since $a = \frac{\delta}{f_{rep,1}}$, see equation 3.3). Up to now, only the beating signal between the n -th modes of the two frequency combs have been considered.

Actually, not only the neighboring modes contribute to the beating signal: for instance, the beating signal between the $(n - 1)$ -th mode of the first comb source and the n -th mode of the second frequency comb source is proportional to:

$$S_{n-1,n}(t) \propto \sum_n A_{n-1,1}^2 e^{-2\alpha_{n-1,1}} + A_{n,2}^2 + 2A_{n-1,1}A_{n,2} e^{-\alpha_{n-1,1}} \cos[2\pi(n\delta + f_{0,1} - f_{0,2} + f_{rep,1})t + \phi_{n-1,1}] \quad (3.9)$$

Hence, the terms are almost equal to the previous case but modulated with the frequency $(\delta + \Delta f_0 + f_{rep,1})$ with $\Delta f_0 = f_{0,1} - f_{0,2}$. If one now considers the beating between the $(n + 1)$ -th mode of the first comb and the n -th mode of the second comb, this modulation frequency is $(f_{rep,1} - [\delta + \Delta f_0])$. So, by considering only the beatings between the $(n \pm 1)$ -th mode of the first frequency comb and the n -th mode of the second frequency comb, two spectra are obtained - images of each other located around the repetition rate of the first frequency comb $f_{rep,1}$. This could be continued for the next terms that are of even higher order. Nevertheless, the higher the order gets, the higher the down-converted frequencies get. Since all spectral information is included in the beat signal of the neighboring modes $S_{n,n}(t)$, it is sufficient to consider only this term, which is experimentally realized by a low-pass filter in the acquisition circuit (see figure 3.3). For this illustration, it has been assumed that the down-converted frequencies do not exceed $\frac{f_{rep,1}}{2}$ whose signification will become clear in the following subchapter.

Figure 3.4 shows a simulated interferogram. This signal consists of regularly spaced peaks whose repetition period is equal to the inverse of the difference in repetition frequency of the two lasers δ . Each burst corresponds to a simultaneous strike of one pulse of each comb source on the detecting photo diode, respectively. The signal is zero between the peaks, without the presence of an absorbent. When a sample is placed in the path of the lasers, as it is the case in the simulation of the interferogram in figure 3.4, a low amplitude

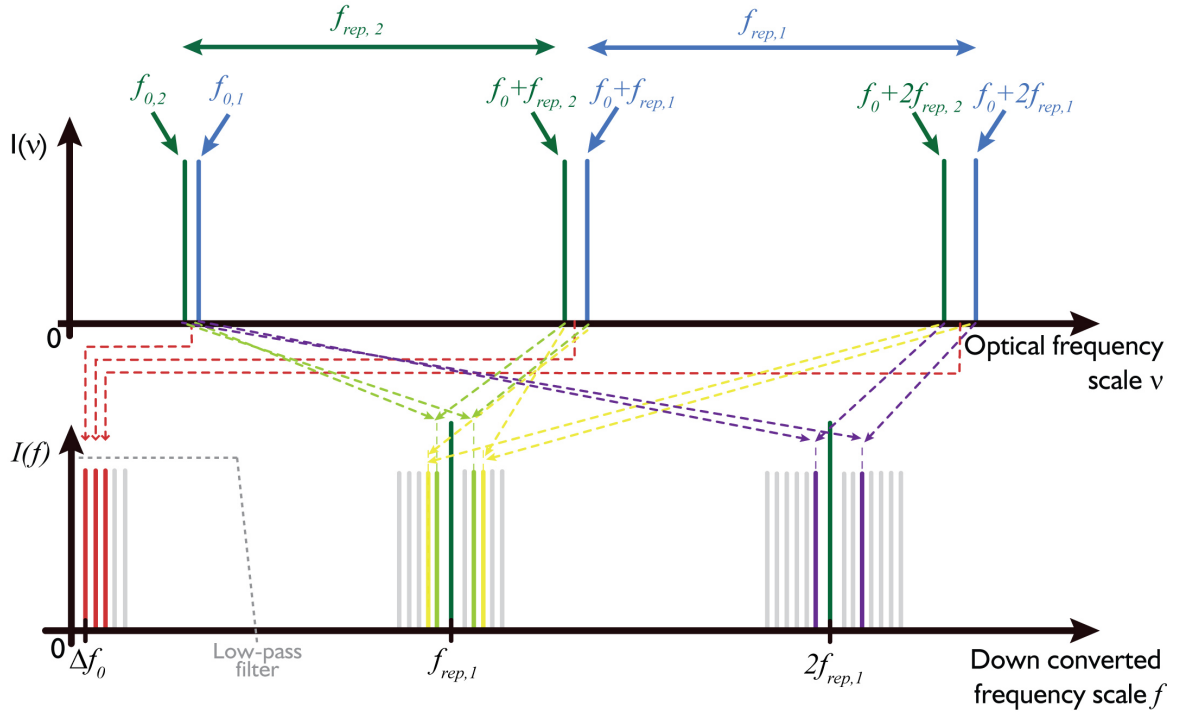


Figure 3.3: Detailed beating phenomenon of the two comb sources. Not only neighboring comb modes are beating like already depicted in figure 3.2. Actually, all modes of the first frequency comb form beat signals with all comb modes of the second frequency comb. For the sake of clearness, only the first, the second and the third comb modes are considered in this figure. The beatings between the neighboring modes are presented in light green and yellow, the beating of the next-nearest neighbors is enlightened in violet. The result of additional orders is just indicated by the weak gray comb modes in the lower part of the figure. Since the full spectral information is contained in the beat notes of the neighboring modes (red), it is sufficient to only observe those and to cut the higher frequencies corresponding to the beat notes of higher orders with a low-pass filter (indicated by the dashed gray line).

modulation appears. The Fourier transform of this signal gives a spectrum in the radio frequency domain depending on the value of δ . As a first approximation, the envelope of the obtained spectrum is the product of the envelopes of the spectra of the two lasers. The knowledge of the comb parameters $f_{0,k}$ and $f_{rep,k}$ can unambiguously re-determine the scale of the optical frequencies.

The special convenience should again be emphasized that a single detector is sufficient to record all the down-converted frequencies. Thus, this spectroscopic method based on two frequency combs is an approach to multiplex spectroscopy. The width of the spectral

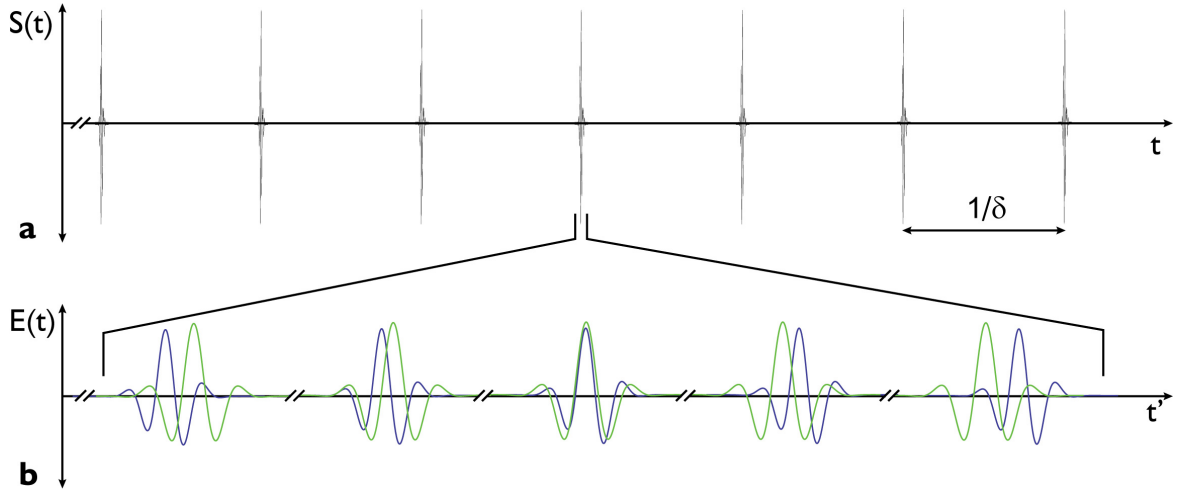


Figure 3.4: The interferogram: Because the two lasers have different repetition rates, the pulses of the two lasers are slowly sliding over each other (b). Here, the interaction of the first laser with the gas sample is indicated by a phase shift and attenuation of the corresponding pulse train (blue) in respect to the pulse train of the second laser (green). The bursts are generated when two pulses of each frequency comb, respectively, arrive at the detector at the same time (a). Between these incidents, there is almost no signal for a long time until the next two pulses arrive and form a burst. The period of the bursts is $\frac{1}{\delta}$.

range that can be simultaneously recorded is only limited by either the spectral range of the sources or the spectral response of the detector.

The value of the down-conversion factor does not only affect the frequencies of the down-converted spectra but has an additional impact on the signal-to-noise ratio of a measurement and on its required acquisition time for a given resolution.

3.1.2 The interplay between down-conversion, resolution and acquisition time

From the value of the spectral width $\Delta\nu$ that one wishes to acquire, it is possible to deduce the optimum difference between the repetition frequencies of the two lasers δ_{max} . At this value, no aliasing of the beat occurs and only the beat of the neighboring modes contribute to the interferogram. It can be derived by the Nyquist-Shannon sampling condition $\Delta\nu < \frac{f_{rep}}{2}$ [82]. Expressed in words, this means that the bandwidth of the down-converted comb should not exceed half of the repetition frequency for an unambiguous assignment of the comb modes. This constraint can easily be illustrated like it is done in figure 3.5.

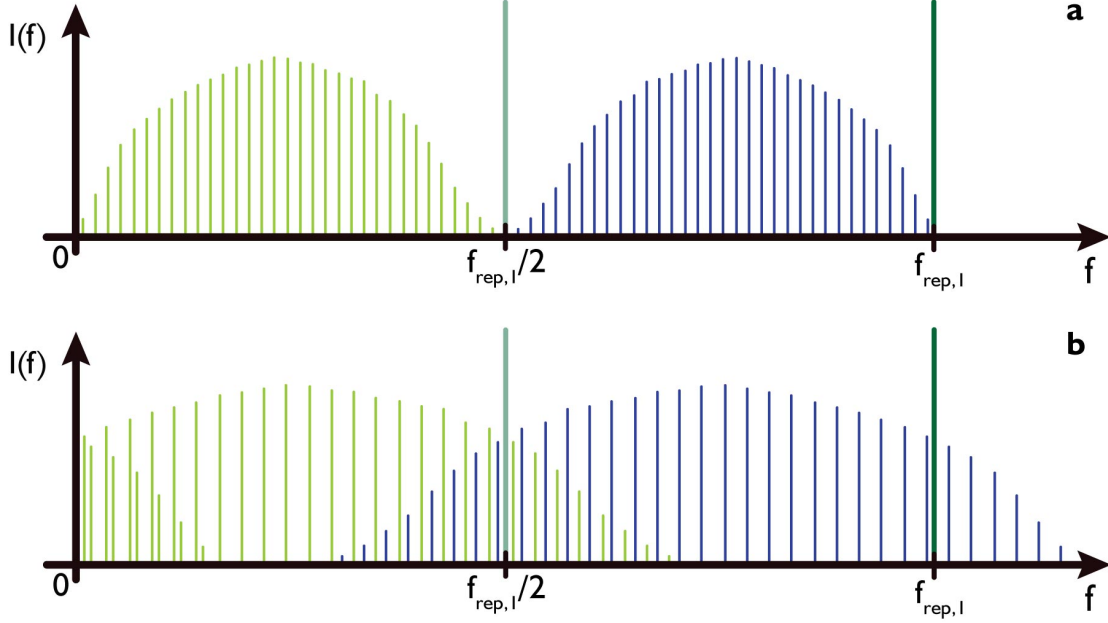


Figure 3.5: If the difference in repetition rate exceeds a certain value, aliasing starts to occur: the different beat notes merge and become ambiguous (b). The upper part of the figure shows the optimum case (a): The free spectral range is fully exploited while the acquisition time is ideal for a given resolution.

With increasing δ , the down-converted frequencies grow, what in addition means that the width of the down-converted spectrum expands further until it starts to overlap with itself and with the beatings of higher orders (see figure 3.5 b). Actually, a high value for δ is favorable because the higher δ gets, the higher the down-converted frequencies become which are decreasingly sensitive to noise ($\propto \frac{1}{f}$). A too low value of δ means that the spectrum range is not ideally exploited (ideal case shown in figure 3.5 a) and the acquisition time t_M also suffers since $t_M \propto \delta^{-1}$. These constraints all together determine the optimum down-conversion factor to

$$a_{max} = \frac{f_{rep,1}}{2\Delta\nu}. \quad (3.10)$$

The ideal difference in repetition rate can be calculated via equation (3.3) to $\delta = \frac{f_{rep,1}^2}{2\Delta\nu}$. As already mentioned in a previous chapter (2.2.2), the resolution of traditional Fourier transform spectroscopy is determined by the maximum path difference introduced by the interferometer. The longer it is, the better the resolution gets. It can principally become as

good as desired, the experimental limitations, however, are related to the size limitations of the measuring instrument and the geometric throughput of the source.

The Fourier transform spectrometer that is based on two frequency combs has no moving parts. Hence, the interferogram is just a function of time and the resolution is no more restricted by the maximum path difference but by the width of the frequency comb teeth as the gas is probed with the comb modes that have a given width in the optical domain. Experimentally, the spectral resolution is most often limited by the memory capacity of the acquisition tool that can record only a certain number of samples. Another limiting factor can be related to fluctuations of the comb parameters f_0 and f_{rep} during the acquisition but if the comb parameters are well stabilized, the resolution is after all limited by the width of the comb modes in the optical domain.

If the down-converted frequencies do not exceed $\frac{f_{rep,1}}{2}$, the sampling frequency at the detector output must be at least $f_{rep,1}$ in order to meet the Nyquist-Shannon sampling theorem. For an acquisition time t_M in seconds, the number of independent recorded samples is equal to $t_M \cdot f_{rep,1}$. The resolution of the down-converted spectrum is given in Hz by the equation:

$$\delta f(t) = \frac{\frac{f_{rep,1}}{2}}{t_M \cdot f_{rep,1}} = \frac{1}{2t_M} \quad (3.11)$$

Hence, also here the time-frequency uncertainty is retrieved that is true for any physical measurement. In the optical domain, the spectral resolution that can be obtained by:

$$\delta \nu(t) = \frac{1}{2t_M \cdot a_{max}} = \frac{\Delta \nu}{t_M \cdot f_{rep,1}} \quad (3.12)$$

Consequently, a long acquisition time, a high down-conversion factor, a narrow comb bandwidth and a high repetition frequency would all result in a good resolution.

Since in this application frequency combs are used, the issue of spectral sampling should be mentioned: With these sources, the sample is probed at discrete optical frequencies corresponding to the teeth of the frequency comb. In the time domain, this means that the molecular spectrum is sampled at the repetition rate of the laser source which probes the sample. As a result, the observed molecular lines may be concealed within the comb structure if the linewidth of the molecular transition is too small. To make sure that the repetition frequency of the interrogating comb is sufficient to sample the molecular transitions properly, the repetition rate of the comb source has to be chosen less than the half width of the molecular transition at half maximum. Otherwise, some transitions may not

be detected. Working with a frequency comb in the near infrared, a repetition rate of about 100 MHz means a sufficient sampling rate to do spectroscopy in the gas phase at room temperature. Indeed, in this spectral region (at 1550 nm), the full width at half maximum of a Doppler profile of a molecular transition is about 460 MHz (calculated for acetylene).

3.2 Initial realization with two erbium frequency combs

The first implementation of a dual comb spectrometer at the MPQ has been realized in 2008 as the first experiment of a fruitful collaboration with the group of Nathalie Picqué from the *Laboratoire de Photophysique Moléculaire (Orsay, France)*.

3.2.1 Setup

As the two sources of the dual comb spectrometer, two identical types of a commercial erbium fiber laser were utilized (model *C-Fiber Sync* by MenloSystems GmbH, principal setup and operation similar to [83]). These models have the option of a variable cavity length (tunable by 400 kHz) for the required flexibility in the difference in the repetition frequencies of the two combs.

The lasers emit about 25 mW of average power behind an included grating compressor providing pulse durations of about 70 fs. The repetition rates are about 100 MHz. The repetition rate is changed by varying the cavity length ($f_{rep} = \frac{c}{2L}$). This is realized by a mirror attached on a piezoelectric transducer (PZT, several kHz bandwidth for short and fast length changes) which is in turn sitting on a stepper motor (for long and slow drifts). The lasers are equipped with one fast photo diode each which together with the fast PZT and an external proportional plus integral controller allows the stabilization of the repetition frequency. Both lasers are operated in a manner that provides two outputs as similar as possible: similar pumping conditions, similar mode-locking regimes, similar adjustment of the compressors for equal pulse duration. The result is shown in figure 3.6. Both lasers emit a broad spectrum of 120 nm centered at 1550 nm with an equal pulse duration of 70 fs.

For the down-conversion of the optical frequencies, the two outputs of the lasers have to be superimposed on a detector which is done by a beam cube after the two beams are re-collimated by lenses (focal length = 5 mm) behind their fiber outputs. A combination

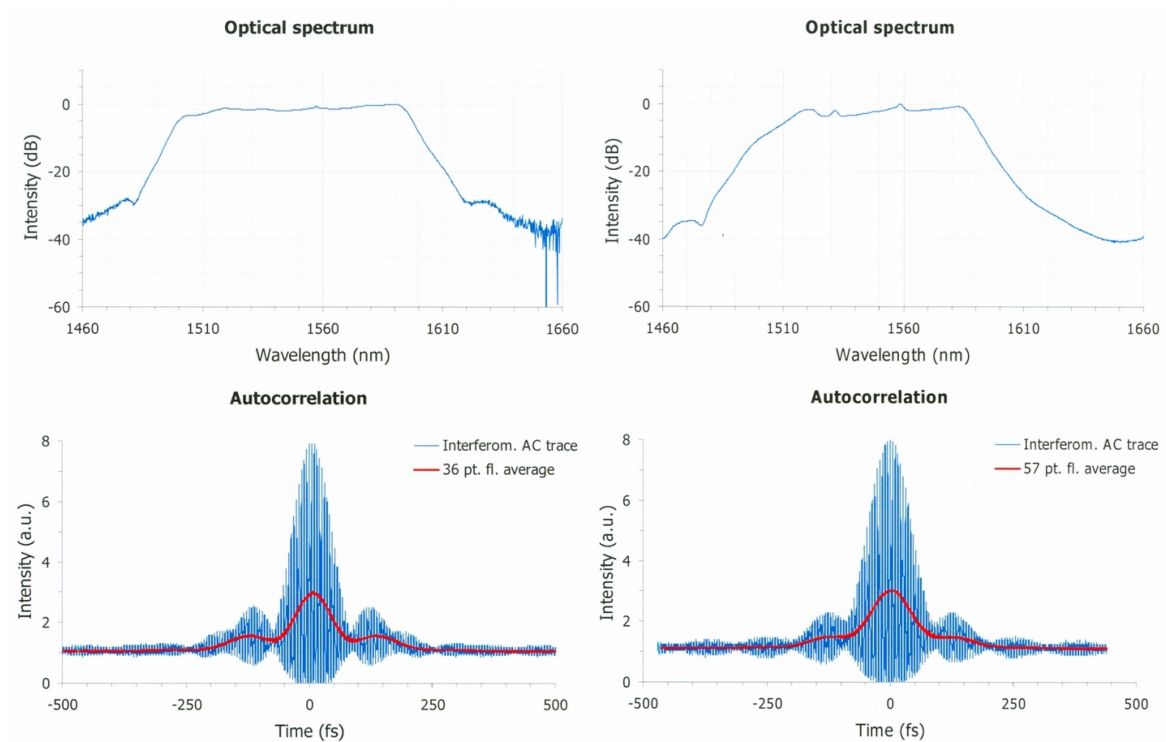


Figure 3.6: The output of the two erbium frequency combs. Both lasers are operated such that they cover the same optical spectrum (FWHM of 120 nm centered at 1550 nm). The compressors are also equally adjusted for a similar pulse shape of 70 fs long pulses. Picture taken from [84].

of a quarter waveplate, a half waveplate and a polarizing beam cube in each branch before the combining beam splitter provides a sensitive adjustment of the power of each laser contributing to the interferogram (see figure 3.7). In fact, a preferably balanced ratio in power results in an optimum amplitude modulation in the interferometric signal.

This balanced signal is detected by a fast photo diode. Since the repetition rates of the lasers are about 100 MHz, the generated beat signal consists of frequencies up to 50 MHz. Hence, the bandwidth of the used InGaAs detector should be above 50 MHz. On the other hand, the usage of a fast detector comes up with some inconvenience: generally, the higher the bandwidth of the detector, the smaller the detection area gets. Thus, sometimes a compromise between these two values has to be found. In the presented setup, the photodiode model 1623 by *New Focus* turned out to be well suited.

The output of the photo diode is filtered using a 50 MHz lowpass filter in order to keep only the signal of interest. This filter means also a protection against aliasing of the down-converted frequencies before sampling. The beat signal is then amplified using a

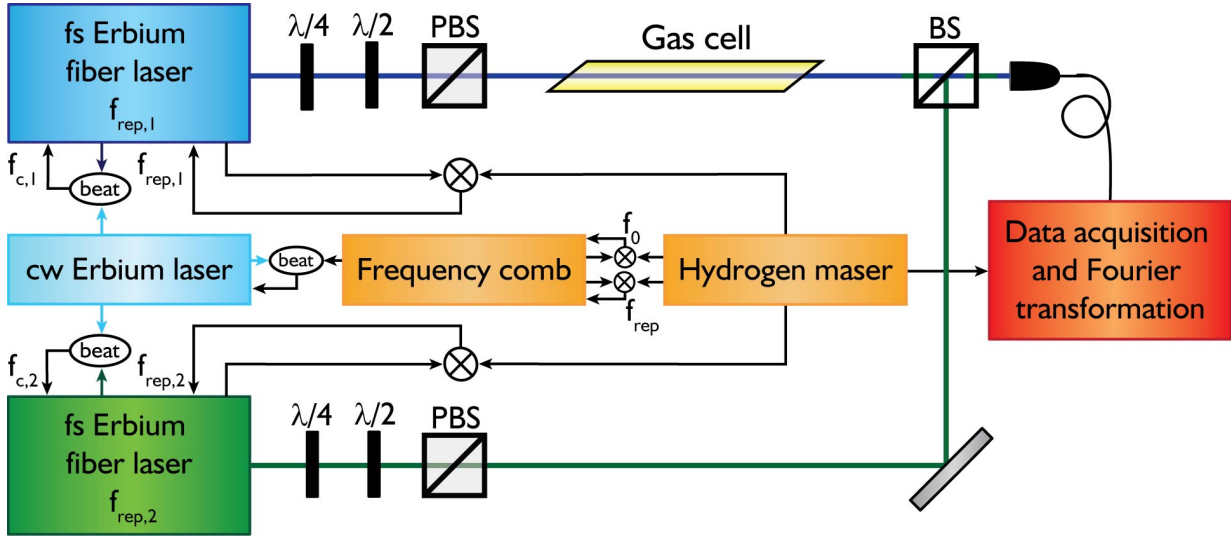


Figure 3.7: Sketch of the complete experimental setup of the dual comb spectrometer based on Erbium fiber lasers including a rough stabilization scheme for the frequency combs. Behind each frequency comb, a combination of a quarter waveplate, a half waveplate and a polarizing beamsplitter enables power adjustment of the laser outputs for a balancing of the interferometric signal. Both contributions are overlapped by a beam splitter and sent to a fast photo diode. The electric signal is filtered by a lowpass filter and led to a digitizing data acquisition board on a computer (not explicitly depicted in the figure) which is synchronized to a hydrogen maser as reference. Both degrees of freedom of each erbium comb are stabilized onto the same reference. The repetition rates $f_{rep,k}$ can be stabilized directly without a supporting optical tool. In contrast, the offsets of the combs are fixed in the comb center $f_{c,k}$ by a stabilization via a beat detection with a continuous wave erbium fiber laser emitting in the middle of the comb spectrum. This cw Erbium fiber laser is in turn stabilized on a frequency comb that is part of a reference frequency distribution system of the institute (indicated in orange, detailed description of the stabilization schemes in section 3.2.2).

commercial voltage amplifier of the company *Femto GmbH* (model DHPVA-200). The allowable gain ranges from 10 to 60 dB (corresponds to a factor in the signal amplitude of 3 to 1000) over a gain independent bandwidth of 200 MHz.

The amplified signal is then sent to a digitizing data acquisition board by *AlazarTech* (model ATS9462) which has a 16 bit resolution and a sampling frequency of 180 MHz. The data acquisition board is a PCI card implemented in a computer that saves the samples. A maximum number of 10^9 samples at the maximum sampling frequency can be recorded. The clock of the acquisition board is synchronized with the reference signal frequency of

10 MHz of the hydrogen maser at our institute to enable precisely regular data collection. To allow correct back-calculation of the down-conversion to the optical frequencies or enable even long measurements for high spectral resolutions, the two degrees of freedom of each frequency comb are also stabilized to the reference maser as it is explained in detail in the following subchapter.

3.2.2 Stabilization

Within the scope of this thesis, the important stabilization circuits for the frequency combs were implemented. The innovative spectroscopic method involving two frequency combs requires the determination of the repetition rate and the offset frequency of each comb in order to find back to the scale of optical frequencies. In addition, since the value of the down-conversion only depends of the differences $f_{rep,1} - f_{rep,2}$ and $f_{0,1} - f_{0,2}$, it has to be ensured that these two quantities do not vary during the acquisition time. If there were fluctuations during the recording, phase errors would occur that would distort the measured spectrum. Hence, the stabilization of the comb parameters should downsize the fluctuations to values that correspond to a cavity length change smaller than 1-10 nm. As already mentioned previously, in order to control the repetition frequency, the length of the laser cavity has to be varied because the repetition rate is dependent of the round trip time T by: $f_{rep} = \frac{1}{T} = \frac{c}{2L}$.

The offset frequency is given by $f_0 = \frac{\Delta\phi \cdot f_{rep}}{2\pi}$, hence, it is dependent of the phase shift between the pulse carrier and its envelope but it is also correlated to the repetition frequency. It can be controlled by adjusting the difference between the phase velocity and the group velocity of the waves propagating in the laser cavity. The pumping power influences the optical index of the amplifying medium, which impacts the phase shift but also the repetition rate. So, f_0 is modified by changes in the current of the pumping diode.

Regarding the fast method of the dual comb spectroscopy, the control of the comb parameters is useful but not always possible within the time required for recording the spectra. In practice, the bandwidth of the feedback systems usually is several kilohertz, often limited by the involved PZT, the bandwidth of the pumping power control is generally several hundred kilohertz. For a low resolution spectra that can be recorded within a few microseconds, it is difficult to control the comb on such a small time scale (in order to have a sufficient control during the acquisition times of μs , feedback loops with a bandwidth on the order of megahertz are necessary). However, advanced feedback controls with satisfactory bandwidth are in principle possible with faster electro-optic modulators or acousto-optics.

For spectra with higher resolution, for which the recording may take several milliseconds or seconds, it is useful and necessary to control and stabilize the comb parameters to keep the scaling factor constant and to minimize phase errors in the spectrum. As already noted in the previous chapter, all instruments of control and measurement are referenced to the same clock, a hydrogen maser. Its relative stability is specified to be $2 \cdot 10^{-13}$ in one second and $1 \cdot 10^{-15}$ in 90,000 seconds. The reference standard frequency delivered by the maser is $f_{maser} = 10$ MHz.

Also part of the stabilization scheme is an Erbium frequency comb that is fully stabilized to the hydrogen maser. This comb belongs to the group-internal distribution system of stable reference frequencies for different applications [85]. This stabilized comb becomes necessary for the second degree of freedom of the source of the dual comb spectrometer what will be explained after the stabilization of the first parameter, the repetition rate.

Control of the repetition rate

The feedback loop for controlling the repetition frequency of the first comb is depicted in figure 3.8 a. The signal of the photo diode that is implemented inside the commercial laser is mixed with a multiple signal (1 GHz) generated from the 10 MHz reference frequency of the maser. If the repetition rate is not stabilized, it will differ slightly from an exact value like $f_{rep} = 100 \text{ MHz} \pm \delta f$. By mixing the reference frequency of 1 GHz with the tenth harmonic of the repetition rate of the laser, the difference frequency at $10 \cdot \delta f$ is generated. Utilizing a harmonic of the repetition frequency reduces the phase noise by $\frac{1}{f^2}$. The signal at $10 \text{ MHz} \pm \delta f$ is isolated by a lowpass filter, amplified and sent to a proportional and integral controller (PI controller) that in turn generates the controlling voltage for the PZT inside the laser. The parameters of the PI controller such as gain and cutoff frequency have to be well chosen in order to tighten the error signal around zero for optimum stabilization. This arrangement allows to enslave the repetition rate directly to the maser reference but only by a round lot as 100 MHz as it is done for frequency comb 1. A frequency counter that is synchronized to the maser, exposes variations in the repetition frequency on the order of $\pm 10^{-2}$ Hz. They correspond to the precision of the measuring instrument that is also on the order of $\pm 10^{-2}$ Hz. Without active control of the repetition rate, the frequency is oscillating by several hertz on a minute time scale.

For the second frequency comb, a commercial feedback loop by MenloSystems is used whose operating principle is the same as for the first frequency comb. The important different feature of this circuit is the generation of 980 MHz out of the 10 MHz reference frequency of the maser (instead of 1 GHz). When this frequency of 980 MHz is mixed with the 10th harmonic of the repetition rate of the comb, a frequency of $20 \text{ MHz} \pm 10\delta f$ is generated (see figure 3.8b). A function generator synchronized to the maser creates a frequency around 20 MHz that is mixed with the frequency of $20 \text{ MHz} \pm 10\delta f$. As before, the resulting signal is isolated with a lowpass filter and fed to a PI controller. The error signal is sent to the PZT of the second comb. Selecting a deviation of the function generator δ' from 20 MHz determines now the important difference in repetition rates δ .

The two feedback loops turned out to be very sensitive to acoustic vibrations. To improve the quality and the duration of the locks, the laser sources have been isolated from the optical table with a suspension system. For optimizing the whole setup, different gain settings of the PI controllers were tried in combination with a set of different models of the involved RF components (mixers, amplifiers, couplers to branch off the signal for the counters). With the right choice, the repetition rates could be locked for several hours without the need of readjusting the stepper motors.

Control of the comb offset

Controlling only the repetition frequency of a comb is not sufficient in order to determine the position of the down-converted modes: The entire comb can still shift as a whole, also with a fixed tooth spacing. Hence, the comb has additionally to be pinned by stabilizing

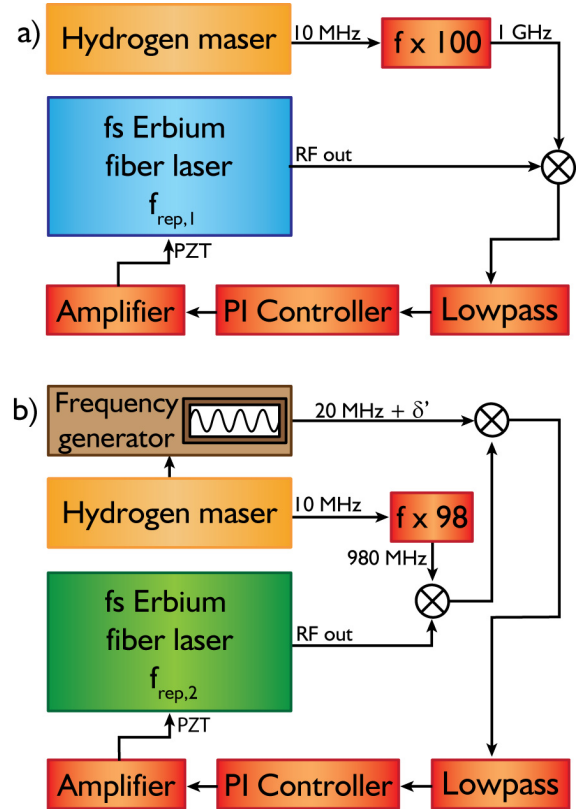


Figure 3.8: Scheme for the feedback control of the repetition rate for the first frequency comb (a). For the repetition frequency stabilization of the second comb, an additional function generator is necessary in order to adjust the difference in repetition rates of the two combs (b).

the position of any of the comb teeth.

The most common method is to constrain the first comb tooth, the offset frequency, by a so-called f - $2f$ -interferometer [86]. To measure and control the offset frequency, it is necessary to beat the frequency-doubled lower part of the comb, $2 \cdot f_n = 2 \cdot [f_0 + f_{rep}]$, with the part that is one octave higher, $f_{2n} = f_0 + 2nf_{rep}$. The beat signal bears the offset frequency: $2 \cdot f_n - f_{2n} = f_0$. Once measured, it can be stabilized on a reference by generating an error signal that controls the optical pumping power of the laser amplifying medium. For this generally used technique, an octave spanning spectrum is required what can be achieved by supercontinuum generation with nonlinear fibers which in turn can complicate the setup. Since there also exists a simpler method, the following alternative technique was chosen for this experiment: because it is enough to fix one of the comb modes, it is adequate to stabilize a comb tooth out of the center directly via a beat measurement with a stabilized continuous wave (cw) laser. This technique can provide a higher stability and is additionally simpler than the f - $2f$ method.

The cw laser that was used for the beat is an Erbium doped fiber laser centered at 1557 nm and specified to have a linewidth of 1 kHz for 120 μ s. The laser is temperature stabilized and a piezoelectric device can quickly fine-tune its wavelength. The cw laser itself is again stabilized to a frequency comb that is part of a stable frequency distribution system that provides the reference to several experiments in the institute (see orange boxes in figure 3.7 and [85]).

The electronic servo system developed to stabilize the teeth of the comb is shown schematically in figure 3.9. The laser beam with the single frequency beats with the comb source onto a photodiode. An electronic signal whose frequency is equal to the difference frequency is produced. The frequency of this signal is between 0 Hz and $\frac{f_{rep}}{2}$. It is then mixed with the signal generator synchronized to the 10 MHz reference frequency of the maser. Adjusting the value of this frequency generator changes the distance in frequency between the teeth of the comb and the cw

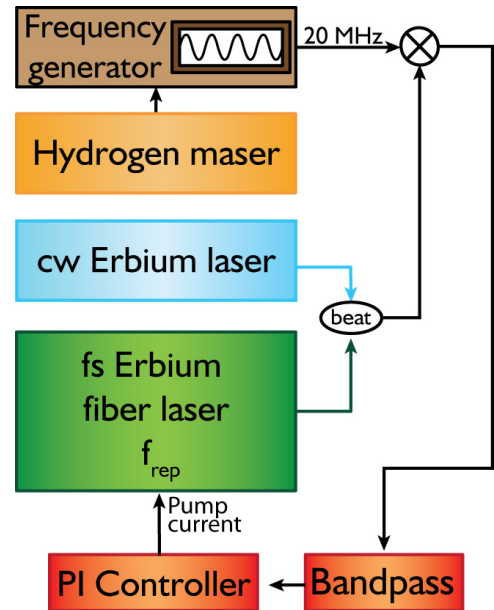


Figure 3.9: Servo loop for the offset control by stabilizing a comb mode of the center spectrum to a stabilized continuous wave (cw) laser.

laser. The generated low frequency

signal is isolated and sent to the PI controller, subsequently, the produced error signal is used to control the current of the diode pump source of the optical frequency comb. The two combs are controlled with identical devices and a single continuous wave laser. Similar to the control device proposed in [87], it can be shown that this feedback system does not influence the scaling factor: δ is insensitive to changes of the cw laser reference. Experimentally, the control of the second degree of freedom of the frequency comb is realized by changing the current of the laser diode that pumps the amplifying medium in the oscillator, once the repetition rate is stabilized. The fixation of the two degrees of freedom of the comb is very delicate: by adjusting the pump power to stabilize the second degree of freedom of the comb, the repetition rate is also changed. The settings of the servo loop control for the repetition rate should be strong enough to correct the changes induced by a change of the pumping power what was accomplished.

3.2.3 Results and discussion

In this subchapter, the experimental results obtained with the new spectrometer consisting of two Erbium frequency combs are presented. At first, the characteristic low acquisition time of the method is presented. Subsequently, the spectra with extreme resolution gained from the method of recording a longer interferogram sequence are introduced.

Real time spectroscopy

The first experiments with this setup allow the demonstration of the ability to record spectra with extremely short acquisition times. For this, the difference in repetition frequencies is set to $\delta = 91$ Hz. For the short acquisition times of this experiment, it is sufficient to only lock the repetition frequencies of the two lasers. As already frequently mentioned, a gas sample is installed behind one of the two combs. Acetylene was chosen to be investigated and was thus filled in a 70 cm long gas cell with a pressure of 127 mbar. The sampling frequency of the spectrum is 180 megasamples per second. Figure 3.10 shows the observed interferogram and the spectrum obtained after the Fourier transformation. Since the important information about the absorption spectrum appears only very briefly after each burst (blue box in figure 3.10), it is sufficient to Fourier transform only this short part which means an acquisition time of 42 μ s. The probed spectral range reaches from 188.5 THz to 201.2 THz (1490-1590 nm). The figure shows additionally the full recorded optical

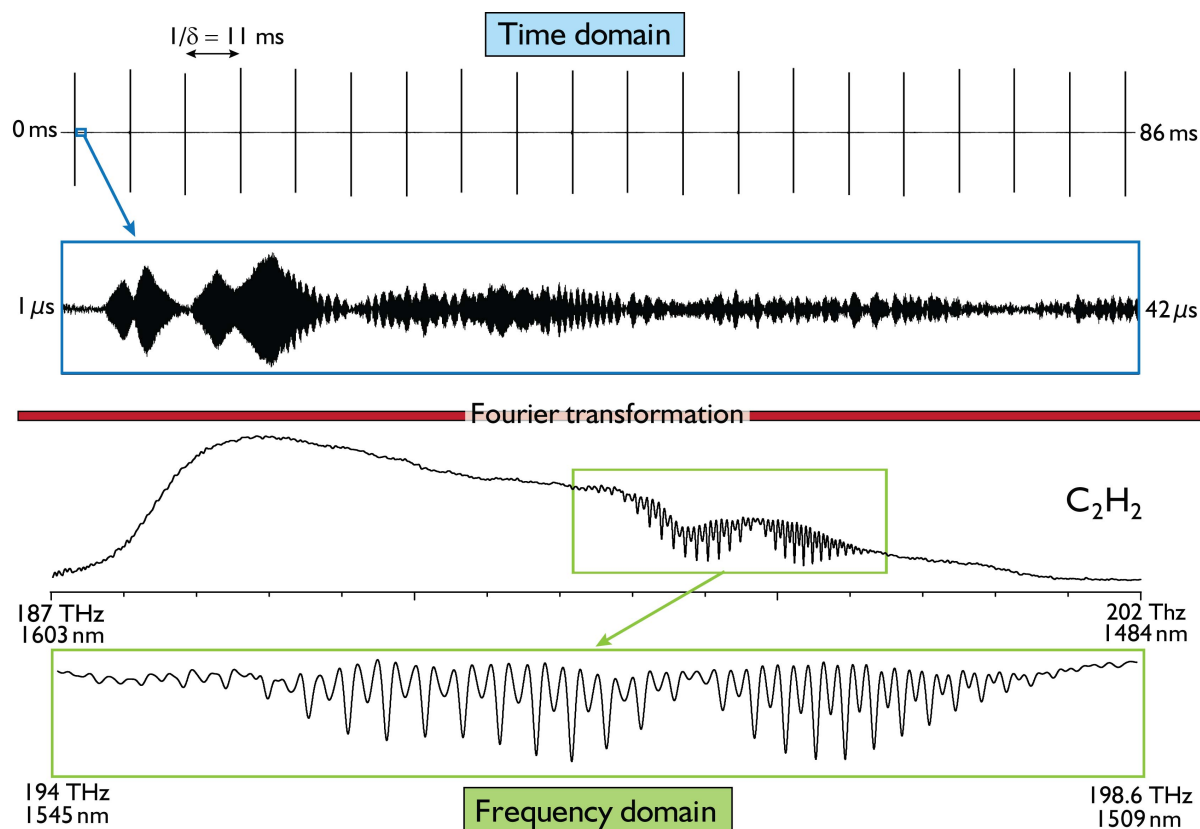


Figure 3.10: Interferogram and resulting spectrum obtained out of a single shot measurement. The absorption information is included in a $42 \mu\text{s}$ long part of the interferogram. After Fourier transformation of this part, the absorption spectrum of acetylene is revealed with a resolution of 12 GHz.

spectrum. Beneath, a zoom of the $\nu_1 + \nu_3$ band of acetylene is depicted whose baseline has been adjusted (green box). With a time of only a few tens of microseconds, an apodized resolution of 12 GHz is achieved in the presented single-shot measurement (see equation 3.12 for the calculation of the resolution).

As expected, the acquisition time of the spectra are extremely short compared to traditional methods of Fourier spectroscopy. Few tens of microseconds are needed to obtain a spectrum whose resolution is equal to the Doppler width of molecular transitions. In comparison with an incoherent source of spectral range and a similar Fourier spectrometer, the required acquisition time is 1 minute for the same SNR. Thus, the method of spectroscopy with two frequency combs reduces the recording time by a factor of one million. As mentioned earlier, with such short recording times and the lasers that we utilize in this experiment, there is no need to implement a control system since changes of the f_0

and f_{rep} cannot be corrected with our lasers. The implemented phase locked loops have a limited bandwidth on the order of a few 10 kHz which means that fluctuations that occur faster than for example 25 μs (corresponds to a bandwidth of 40kHz) cannot be managed. Nevertheless, these fluctuations in the position of the comb teeth that presently cannot be fixed during the 10 μs fast acquisition times can cause phase fluctuations which would result in chromatic distortions in the spectrum that are uncorrectable a posteriori and, hence, would deform the spectrum.

Since the acquisition times are extremely fast and the lasers have a high spectral brightness, the sensitivity for 1 s time average (NEA, definition see equation 2.4) is on the order of $7.9 \cdot 10^{-7} \text{ cm}^{-1} \text{ Hz}^{-1/2}$ (with a SNR of 117). To further improve the detection sensitivity, the feature of the lasers' high average power can be harnessed: because of their adequate powers, the absorption path length can be increased by a multiple what enhances the sensitivity of the method. This possibility was realized for example with the means of an enhancement cavity and will be explained in detail in chapter 4.

Extreme resolutions

By increasing the measurement time, the resolution can also be even further improved. The resolution of the recorded spectra depends on the recording time of the beat signal between the two combs. In theory, it is possible to achieve a spectral resolution that is at best equal to the intrinsic width of the comb teeth in the radio frequency domain were the comb linewidths are also down-converted by the factor $\frac{1}{2 \cdot t_M} \cdot a$.

Here, the method of *interleaving* is presented that further improves the resolution. The extended measurement time is resulting in an apparent resolution that seems to be given by the resolved comb linewidth. In fact, the real resolution of the observed molecular transition is determined by the repetition frequency of the laser that probes the gas sample with this certain frequency.

For the long acquisition times of this part of the experiment, it is necessary to lock both comb parameters f_0 and f_{rep} . Otherwise, the subsequent bursts of the interferogram would fluctuate too much and as a result, the high resolution spectra would be blurred out due to the oversized phase errors. For this experiment, a difference in repetition rate of $\delta = 200$ Hz was measured. This means a periodicity in the interferogram of 5 ms. With the help of the feedback loops, it was possible to keep the standard deviation of the fluctuations below 2 μs which corresponds to an uncertainty that is less than $4 \cdot 10^{-4}$.

The measurement time was 3.35 s what effectively results in 670 bursts that contribute to

the improved resolution.

For the acquisition of the high resolution spectra (which resolve the teeth of the comb), presented subsequently, the offset frequencies $f_{0,k}$ of both combs are stabilized via a center mode (as described in 3.2.2) and the gains and bandwidths of the servo systems are adjusted to minimize the time variations between the maxima of the interferogram. Figures 3.11 and 3.12 show the spectra recorded at a resolution that is unattainable by traditional Fourier spectroscopy.

The spectrum of figure 3.11 is the Fourier transform of the beat signal recorded in 3.35 seconds (3.11 a). The obtained spectrum ranges more than one hundred nanometers and its envelope looks similar to the previous spectrum since the lasers haven't been changed in their mode-lock operation. The spectrum, as shown at the present scale in 3.11 b, appears completely black because of the high spectral resolution in the optical frequency range of 420 kHz: the teeth of the comb are completely resolved. The spectrum consists of 130,000 evenly spaced teeth that were all recorded simultaneously. The spectrum is the Fourier transform over 536 megasamples. This is the maximum number of samples that can presently be recorded with the available data acquisition system. A zoom into the dense tooth spectrum reveals the comb structure (3.11 c). At the bottom of the figure (3.11 d), an enlargement of one of the comb teeth is depicted. The resolution is given by the width at the half maximum of the tooth. To record an equivalent spectrum with traditional Fourier transform spectroscopy (i.e. same resolution within the same acquisition time), the scanning mirror has to be moved a distance of more than 357 meters with a velocity of $v = 107$ m/s.

As already noted, the current acquisition system and the present technical ability to calculate the Fourier transform determine the number of time samples to 536 millions. In order to further improve the resolution of the recorded spectra, the only solution is to increase the scaling factor and hence to reduce the free spectral range. To avoid the associated aliasing, the extent of the optical spectral range must be restricted. For this purpose a fiber Bragg filter is connected directly behind the outputs of both lasers. The spectral bandwidth of these filters are 1 nm (126 GHz) and they are centered at 1542.5 nm (194.35 THz). Since the power of the optical signal at the output of the filters is much lower than without the filters, the previously used detector is replaced by an avalanche photodiode. Under these conditions, the difference in repetition frequencies between the lasers can be increased to up to $\delta = 18$ kHz. Figure 3.12 shows the spectrum that was recorded with the previously used gas cell filled with acetylene with a pressure of 68 mbar. The spectrum

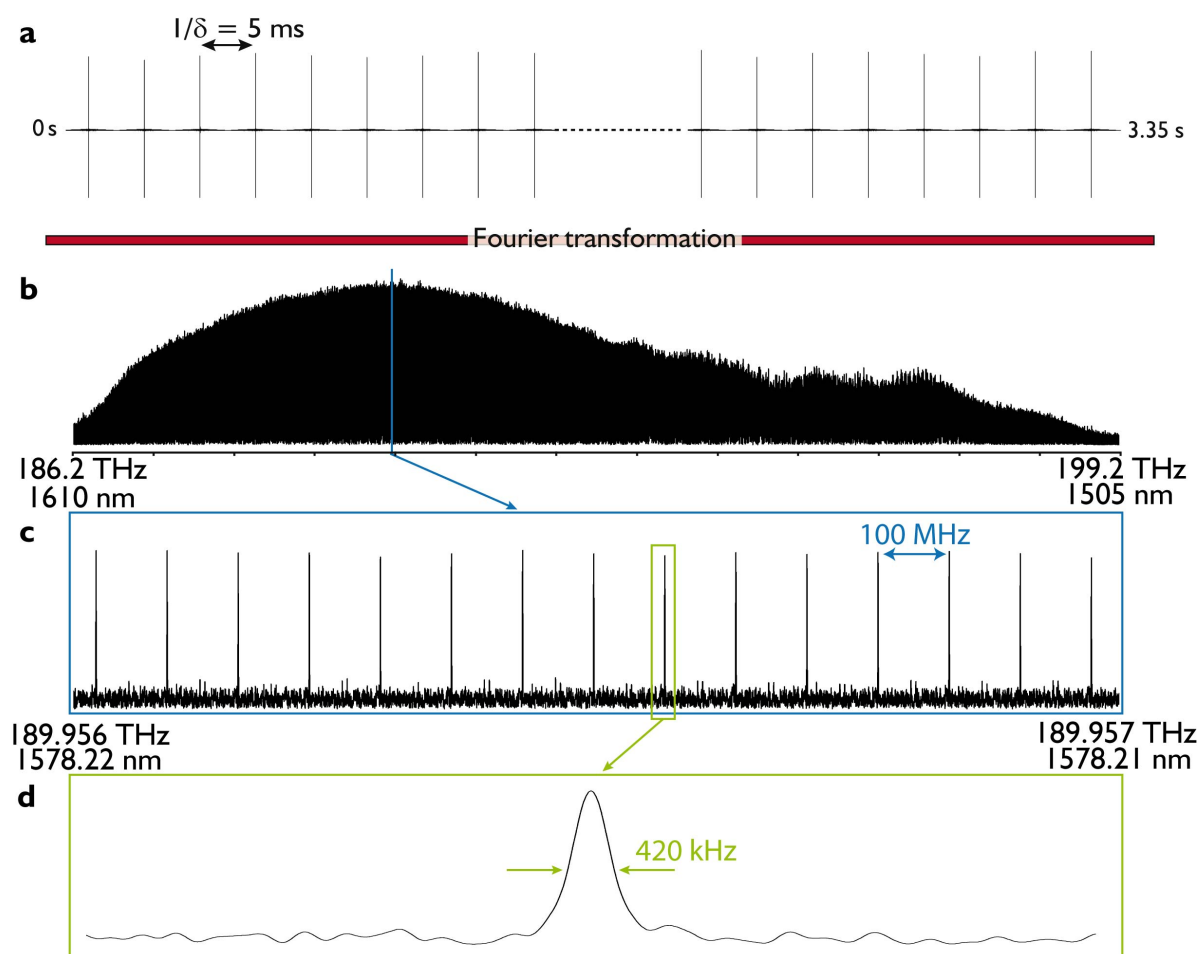


Figure 3.11: Absorption spectrum of acetylene spanning 105 nm with 420 kHz resolution. The interferogram is plotted in the upper part of the figure. It consists of 536 million samples and results from a 3.35 s measurement. Its Fourier transform displays very well resolved comb lines. The resolution of the comb lines is 420 kHz high and is only limited by the data acquisition system.

again consists of the maximum possible number of 536 million independent elements and about 1260 comb teeth. The recording time could be increased to 6 s until the acquisition limit was reached¹. The apodized spectral resolution is only 2300 Hz. It is still limited by the properties of the acquisition system. The most intense molecular line can be seen in 3.12 b, the P(27) line in the $\nu_1 + \nu_3$ band. In order to get to the same resolution with a traditional Fourier spectrometer, the mirror would have to be moved almost 65 km within

¹Simultaneously, the sampling rate had to be reduced to 100 megasamples.

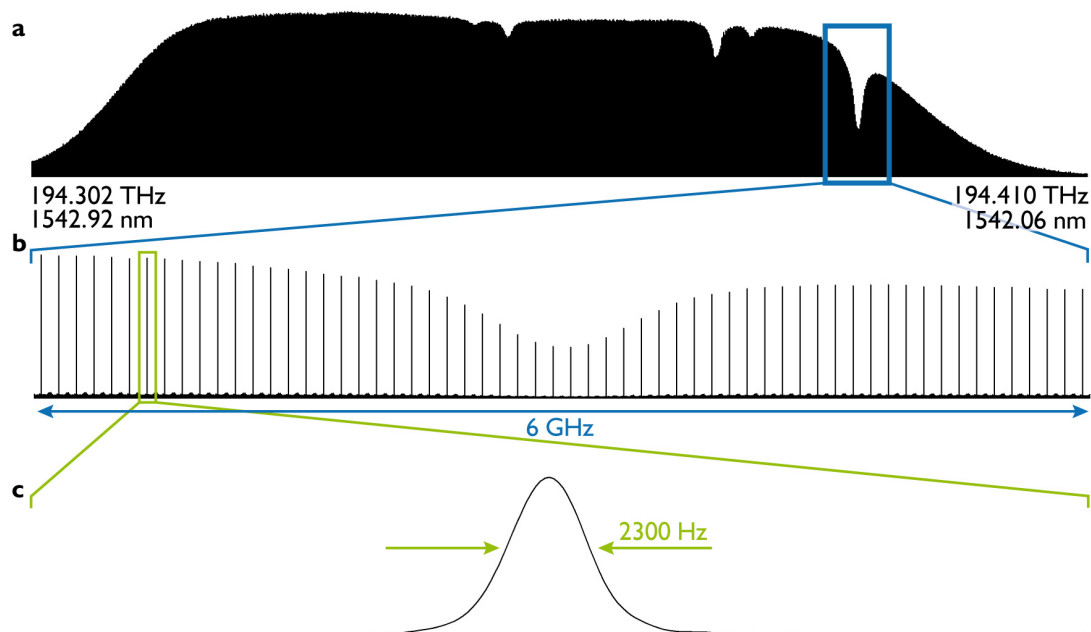


Figure 3.12: kHz resolution of an absorption spectrum of acetylene obtained out of 536 megasamples measured within 6 s. **a** The whole spectrum (displayed at 110 kHz resolution) appears black because it consists of discrete cramped comb lines. An optical bandpass filter is used to use an only 1 nm broad spectrum for the limited number of samples. Chart **b** shows a zoom on the P(27) line of the $\nu_1 + \nu_3$ band at 7500 Hz resolution, while **c** displays a single comb line surrounded in green in **b** with full 2300 Hz apodized resolution.

6 s, what would result in an unworkable scanning speed of almost 11 km/s in addition to the unrealistic size of the interferometer.

Resolving the teeth of the comb spectrum brings along many benefits. The first is the improved signal-to-noise ratio (in the last presented case around 400). It is observed that as soon as the spectral resolution becomes sufficient enough to resolve the comb teeth, the SNR of the spectrum improves. In fact, in the case of resolved comb lines, the recorded spectrum has the same properties as an emission spectrum recorded with traditional Fourier spectroscopy. Its signal-to-noise ratio increases with the path difference, thus with the resolution like it is observed in this experiment. The second advantage is the possibility of using the comb teeth as a frequency ruler for self-calibrating the absolute scale of the optical frequencies. Finally, the study of molecular profiles is simpler and more accurate

thanks to a device function which becomes negligible with spectral resolutions exceeding the Doppler width of the molecular transitions by a factor of 100000.

By stabilizing the combs, the high precision that is standard for frequency metrology can now be transferred to the field of broadband spectroscopy. Compared to the possibilities offered by the traditional Fourier spectroscopy, the relative accuracy in the scale of optical frequencies is outperformed by a factor of one million in this experiment.

For the sake of completeness, it shall be mentioned that additional experiments concerning pressure broadening and dispersion measurements were also performed. Detailed information on these demonstrations can be found in the thesis of Julien Mandon [88]. In this work, the method of interleaving can additionally be read in detail: an application to further improve the spectral sampling. In the experiments presented here, the sampling step is the repetition frequency, i.e. $f_{rep} = 100$ MHz. This is sufficient for molecular spectra at room temperature because the Doppler width of the molecular transitions are on the order of 400 MHz in the near infrared region. However, the spectral sampling step could still be improved by the following: successively different interferograms were recorded while the offset frequencies of the combs were tuned in small steps for each measurement. By this technique, the comb teeth are slipping over the absorption lines and by this, the line shapes of the molecular transitions can be identified much better. To be more accurate, the sampling step could be advanced by a factor of 100 to 1 MHz (see figure 3.13). To achieve such a sampling rate of 1 MHz means to save 100 spectra. However, the acquisition time is relatively low since it takes only 10 minutes to record all spectra at a resolution of 2300 Hz.

For the presented method of extreme resolutions but also for a clean absorption spectrum without any distortions during the previously demonstrated short acquisition times, it is necessary to actively stabilize the frequency combs. Especially, in order to prevent any perturbations during the measurement times, the feedback loop has to provide a pulse to pulse timing jitter below 1-10 as. Such advanced phase locked loops are challenging and require both experience and extensive equipment of radio frequency technology [89]. Recent experiments tested an alternative method to the stabilization of the frequency combs. The new technique of adaptive sampling uses the reference signal between pairs of modes of the two involved combs as an external clock for sampling the interferogram. This synchronizes the data acquisition and compensates optical delay fluctuations of the interferogram. As a result, the recorded spectra look far less scrambled in comparison to the same experiment with free-running combs suggesting an attractive alternative to the sophisticated and ex-

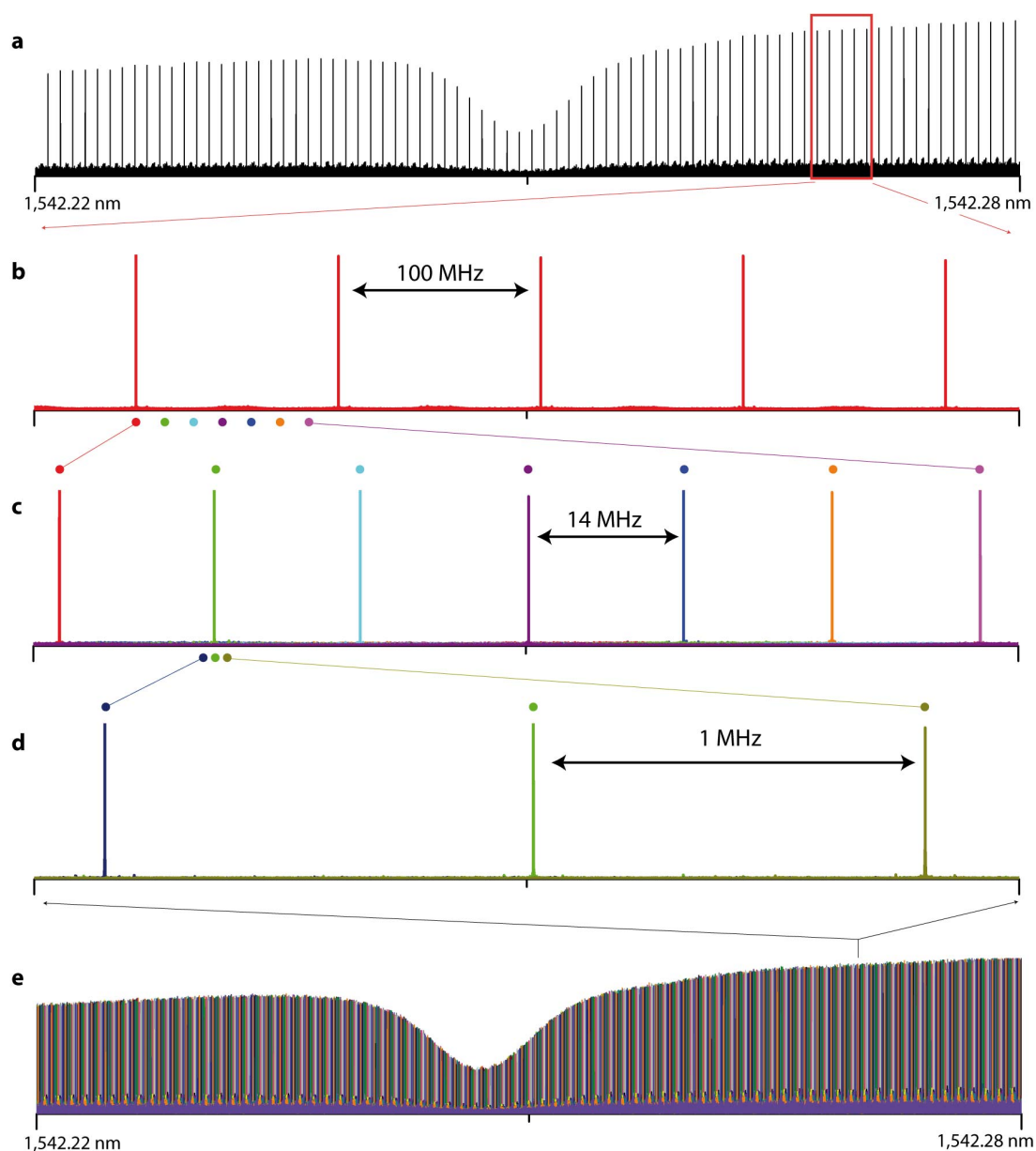


Figure 3.13: The method of interleaving in order to increase the resolution. **a** Recording a longer interferogram with several bursts reveals the comb structure after Fourier transformation. **b** The resolution of the probed molecular transition is limited by the comb repetition frequency (here 100 MHz). **c** By recording several interferograms after successively shifting the offset frequency, the resolution is increased to 14 MHz and to 1 MHz after additional, smaller steps in the offset frequency adjustment (**d**). Picture taken from [88].

pensive method of stabilizing the combs onto a reference [90].

3.2.4 Comparison with traditional Fourier transform spectroscopy

The detailed introduction of the innovative spectrometer using two frequency combs completes here with a survey of all the advantages that the new method brings along, especially in comparison with the so far widespread traditional technique.

The new approach is based on the same physical principle of down-converting the optical frequencies but without the use of mechanical elements. Hence, this method allows to record spectra much faster while simultaneously achieving unrivaled resolutions. The problem of limiting the acquisition time due to the speed of the moving mirror of the spectrometer no longer exists. A numerical example illustrates the advantage of the static spectrometer: for instance, frequency combs with a repetition rate of 100 MHz that emit a 120 nm broad spectrum centered at 1550 nm (FWHM) like in the experiment that was just presented in 3.2 would provide a resolution of

$$\delta\nu = \frac{(201 - 186) \text{ THz}}{1\text{s} \cdot 100 \text{ MHz}} = 150 \text{ kHz} \quad (3.13)$$

with an acquisition time of 1 second. With a traditional Fourier transform spectrometer based on a Michelson interferometer, the scanning mirror would have to be traversed a distance of 1 km within the measurement time of 1 s to achieve a comparable resolution. This simple example shows the clear supremacy of the dual comb Fourier spectroscopy.

With a Michelson interferometer, the down-converted spectrum is limited to the range of acoustic frequencies. With the spectroscopic method based on the use of two combs, the down-converted spectrum can cover up to half of the repetition rate of the laser probing the sample. It is therefore in the radio frequency domain, an area where the frequencies are nearly a thousand times higher. These high frequencies are preferable since the noise goes with $\frac{1}{f}$: higher frequencies are less sensitive to noise and thus provide a better signal-to-noise ratio.

The utilization of laser sources instead of an incoherent light source additionally results in an improved signal-to-noise ratio despite the short acquisition times.

Provided that the comb lines are resolved or all comb parameters are known, another attractive advantage of the dual comb spectrometer is the fact that the calibration of the frequency scale is principally already included in the device, providing a higher accuracy than the established technique. In traditional Fourier spectroscopy, the operation of the

Michelson interferometer provides a knowledge of the frequency scale with a relative precision of 10^{-9} by molecular calibration standards. However, an absolute knowledge of the frequency scale without using a molecular reference stays delicate. The main problem is that the He-Ne laser that is generally used as a reference for measuring the path difference does not follow exactly the same optical path in the interferometer like the beam whose frequencies are measured. Nevertheless, accuracies of 10^{-9} could be achieved with this method involving molecular standards [12, 13].

With the new technique involving the combs, the accuracy of the frequency scale is determined by the precision in the measurement of the comb parameters since the scaling factor a is indispensable for the back-calculation to optical frequencies and is dependent of the comb parameters (see equation 3.3). For the radio frequencies $f_{0,k}$ and $f_{rep,k}$, the simplest available measurement tools are counters like the counter model *53131A* by *Agilent*. They can be used to measure frequency values relative to a precise reference source. The precise measurement of the two repetition rates is required for determining the down-conversion factor a . The two offset frequencies $f_{0,k}$ (or in our scheme the absolute position of the combs via the knowledge of the absolute position of a center comb line) have to be monitored for potential phase drifts that can occur during the acquisition time and that should be taken into consideration a posteriori. The reference for the counters is for example a signal delivered by a hydrogen maser (Microwave Amplification by Stimulated Emission of Radiation). The radio frequency measurement is principally limited by the accuracy the reference provides, which is typically 10^{-13} in one second measurement time, but can also be worse (10^{-7} - 10^{-8} , see [91]).

Most frequency counters do not work accurately enough, especially on the ms time scale: They provide eight digits at a gate time of 1 ms what corresponds to a counting error of 10 Hz for the given repetition rate of 100 MHz. This relative uncertainty of $1 \cdot 10^{-7}$ in the frequency measurement impinges much stronger (i.e. 10 percent) upon the down-conversion factor and, hence, also on the optical domain: Let's assume two lasers with slightly different repetition rates $f_{rep,1} = 100.000100$ MHz and $f_{rep,2} = 100$ MHz. The down-conversion factor would then be $a = \frac{100 \text{ Hz}}{100 \text{ MHz}} = 1 \cdot 10^{-6}$ (see equation 3.3). The inaccuracy of the counter on the order of 10 Hz could also result in the unequal down-conversion factor of $\tilde{a} = \frac{110 \text{ Hz}}{100 \text{ MHz}} = 1.1 \cdot 10^{-6}$. Using these variable down-conversion factors to recalculate a frequency that is located in the RF domain back to the optical domain produces two

largely different results:

$$\begin{aligned} f_{RF} \div a &= 193 \text{ MHz} \div 1 \cdot 10^{-6} = 193 \text{ THz} = f_{opt} \\ f_{RF} \div \tilde{a} &= 193 \text{ MHz} \div 1.1 \cdot 10^{-6} = 175.\overline{45} \text{ THz} = \tilde{f}_{opt} \end{aligned}$$

Hence, a miscalculation of only 10 Hz results in an uncertainty in the optical domain of 17.5 THz in this example (i.e. almost 10 %). Since the transition linewidths in the near infrared range are about 460 MHz broad, counters are inappropriate for the back-calculation into the optical domain since the uncertainty they produce is too large. The uncertainty would get negligible as soon as it is $< \frac{\pi}{8} \frac{d\sigma}{S/N}$ ($d\sigma$ is the halfwidth of the transition, S/N the signal to noise ratio, see [92]). In our experiment, this critical value would be $\frac{460\text{MHz}}{400} = 1.15 \text{ MHz}$ what would correspond to a required accuracy of the counter of 10^{-14} . Since this is far beyond what is met by state-of-the-art counters (especially for a general acquisition time on the order of μs , see [91]), the calibration of the optical axis still has to be done with the help of molecular standards or molecular spectroscopic databases as for instance the HITRAN database [7].

Singly measurements that resolve the comb lines do not need such a helping tool for the calibration. Here, with measurement times on the order of seconds, the frequency comb can be used as a frequency ruler whose lines have an absolutely known position. They allow accurate calibration of the frequency scale measured by the dual comb spectrometer. An absolute knowledge of the frequency scale is possible with the same high accuracy that the reference provides that the combs are stabilized to without having to record the spectrum of a molecular standard. Using an optical frequency standard as reference would even improve the uncertainty further to 10^{-15} in 1 second measurement time.

With the presented experiment, it could be proven that the novel dual comb spectroscopy technique can provide short acquisition times, high resolutions and high accuracies. The new approach would become even more attractive if it provided in addition advanced sensitivit

Chapter 4

Cavity enhanced dual comb spectroscopy in the infrared region

4.1 Improving the sensitivity

The previous chapter showed that dual comb spectroscopy can achieve standard resolutions on the order of GHz with very short acquisition times of several μs . However, another property of the approach, the sensitivity, could still be improved (in subchapter 3.2.3 on the order of $10^{-8}\text{cm}^{-1}\text{Hz}^{-1/2}$). This chapter presents an experiment aiming at this objective while simultaneously maintaining the mentioned short measurement times without any deterioration in resolution.

An increased sensitivity would not only benefit the measurements in the near infrared range but would also extend the applications of a dual comb spectrometer to the mid infrared. In the near infrared wavelength range, only overtone transitions of molecules are located. Since these transitions have a low cross section (10^{-5} to 10^{-8} of the fundamental transitions, [93]), they are weak and, hence, difficult to detect. This complication can be overcome when the presented dual comb spectrometer becomes more sensitive. The fundamental, stronger rovibrational transitions of molecules are found in the mid infrared region. Here, a high sensitivity for their detection is not as much required but would still be of large interest: trace concentrations of gas samples (on the order of parts per trillion) could be detected turning the dual comb spectrometer attractive for trace gas analysis.

Eventually, this amelioration in sensitivity can be realized by increasing the path length that the light interacts with the gas sample (see also equation 2.4). For that purpose, the single-pass cell is often exchanged by a multi-pass cell that extends the path length from a

few tens of centimeters to several tens of meters. On this longer path, the light experiences the absorption of the sample for an enhanced extent (see the Beer-Lambert law, equation 2.1). This effect can be magnified even more by using a high finesse cavity instead of the multi-pass cell. This cavity elongates the path length to several hundreds of meters as it is shown in this chapter and in the publication [94].

4.2 Experimental setup

The experimental setup is based on the same physical principle as the dual comb realization in the previous chapter. Here, two ytterbium lasers were implemented that are emitting at 1040 nm. Besides the important extension of an enhancement cavity instead of a single-pass cell for an improved sensitivity, an ytterbium (Yb) amplifier was also installed after one of the two fs lasers (see figure 4.1). The first frequency comb is amplified and injected into the enhancement cavity located in a gas chamber. As already noted in the previous chapter, it is preferable to have a balanced beating signal for a large signal-to-noise ratio of the interferogram. Since the high finesse cavity consists of high reflecting mirrors, the light that is transmitted by one of these mirrors and that is used as one of the two contributions for the beating signal will be of little power. The integrated Yb fiber amplifier in the setup helps to get to a more balanced signal since it increases the power of the light coupled into and out of the cavity. The light that is transmitted by the cavity and that carries the absorption information is overlapped with the output of a second frequency comb that has a slightly different repetition rate. The beating signal of the two combs which is located in the radio frequency domain is sent onto a fast photodiode. The signal is low-pass filtered and transferred to a data acquisition board on a computer for digitization and Fourier transformation of the data in order to reveal the absorption spectrum.

For this experiment, two Yb fiber lasers were used. One of the lasers is amplified before it is injected into the enhancement cavity.

The beam transmitted through the cavity is overlapped with the second Yb fs laser with slightly detuned repetition rate. The beating signal is finally detected with a photodiode for the data acquisition. The following subchapters will provide a closer look to the most important components of the experiment such as the Yb lasers, the Yb amplifier and the enhancement cavity.

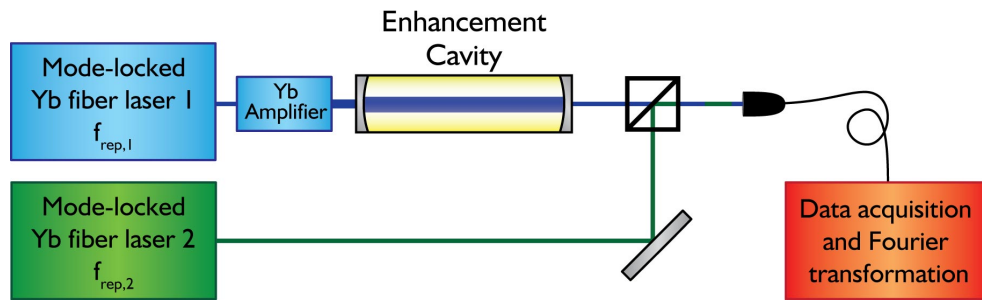


Figure 4.1: Principle of dual comb spectroscopy with enhanced sensitivity. The broad spectral output of a frequency comb with its equidistant modes is amplified and injected into an enhancement cavity that simultaneously serves as the gas chamber. The interaction length between the laser light and the gas sample is increased by the enhancement factor of the cavity. The light-storage effect of the enhancement cavity is indicated by the broader beamline between the two cavity mirrors. For the down-conversion of the optical absorption spectrum, the light that is transmitted by the cavity is overlapped with a second frequency comb with slightly different repetition rate and detected by a photodiode. Finally, the time-domain interferogram is recorded and Fourier transformed to get to the absorption spectrum.

4.2.1 The ytterbium lasers

The two utilized fs lasers are two ytterbium (Yb) fiber lasers. One is a prototype by *MenloSystems GmbH* (model *Orange*, in the meantime also commercially available) and the second one is a home-made laser that is one of the successful results of a diploma thesis in our group [95]. Both lasers share the same principal setup, shown in figure 4.2.

The lasers consist mainly of two parts: a free-space sector and a fiber part that is basically the Yb^{3+} -doped gain fiber and the fiber combiner that couples in the light of a laser diode pumping the oscillator at 976 nm. The ring resonator is closed via the free-space part that features two gratings and two pairs of half- and quarter-wave plates that in combination with a polarizing beam splitter are used for polarization-dependent Kerr-lens mode-locking. Via the distance between the two gratings, different dispersion regimes of the oscillators can be chosen. Depending on the total dispersion, the oscillators can emit so-called soliton pulses [96] or self-similar pulses [97] for negative or positive dispersion, respectively.

The two lasers performed best in stability running in a positive dispersion regime ($\text{GDD} \cong 11000 \text{ fs}^2$). The corresponding spectra and pulse shapes are depicted in figure 4.3. The first laser has an output power of 120 mW and a repetition rate of 128.7 MHz. The second frequency comb has an output power of 100 mW and its repetition rate is slightly

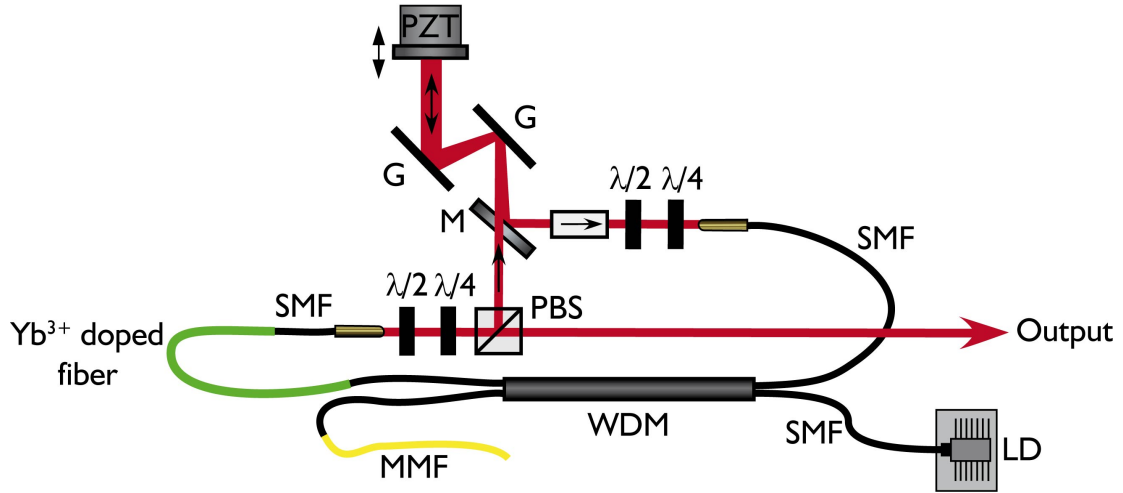


Figure 4.2: Principal setup of the Ytterbium lasers. The pumping light of a laser diode (LD) is injected into a ring resonator via a wavelength division multiplexer (WDM) and coupled into the Yb^{3+} -doped gain fiber. The light is sent to a free space part via a collimator. Two half- and two quarter-waveplates change the polarization for Kerr-lens mode-locking together with a polarizing beamsplitter (PBS) which in addition serves as the laser's output coupler. Two adjustable gratings (G) enable dispersion selection of the running lasers. A mirror mounted on a piezo-electric transducer (PZT, for cavity length control) serves to close the loop of the ring resonator. An isolator guarantees uni-directional operation. Abbreviations SMF and MMF represent single mode fiber and multi mode fiber, respectively. The multi mode fiber prevents perturbation by reverse reflexions from the blind end of the WDM back into the oscillator cavity.

detuned with respect to the first comb by a fixed value between 200 and 600 Hz during the experiments.

Comparison of the spectra of these two lasers shows that the spectrum of the first frequency comb is much broader (see parts a and c in figure 4.3). However, since this laser is amplified and injected into a cavity with non-zero dispersion, this spectrum is narrowed and adapted closer to the spectrum of the second comb as shown in the next two subchapters.

4.2.2 The ytterbium amplifier

The ytterbium fiber amplifier that is used to increase the power of the first Yb laser, is the prosperous achievement out of a collaboration with Prof. Yohei Kobayashi of the *Institute for Solid State Physics, University of Tokyo*.

Its experimental setup can be reconstructed in figure 4.4. Before the laser light is in-

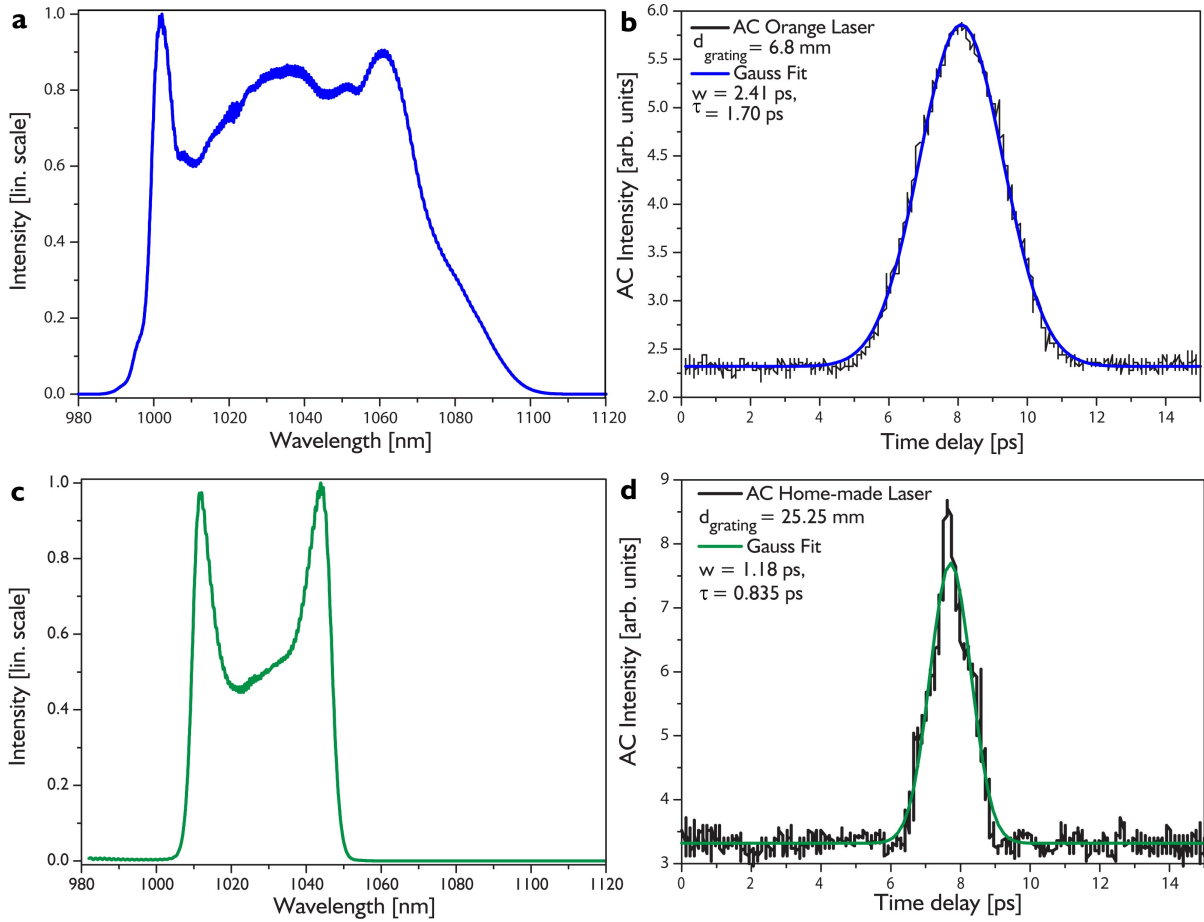


Figure 4.3: **a** Spectrum and **b** auto-correlation (AC) function of the first frequency comb (Prototype *Orange* by *MenloSystems GmbH*). **c** Spectrum and **d** auto-correlation function of the second frequency comb, a home-made Yb-fiber laser running in the same positive dispersion regime like the first comb. The spectral bandwidths of the lasers correspond to Fourier limited pulse durations of 23 fs and 39 fs, respectively.

jected into the amplifying fiber, the pulses are stretched by a 3 m long stretcher fiber (model *HNDS1582BA-4-2-2* by *Sumitomo*) to about 15 ps. This fiber was chosen because it pre-compensates the third order dispersion introduced by the amplifying fiber and the compressor gratings behind the amplifier.

After an isolator that protects the oscillator from back-reflections, the stretched pulses are coupled via an achromatic lens ($f = 50\text{mm}$) into the 1.8 m long amplifying polarizing double-clad fiber (DC-200/40-Pz-Yb-01 by *NKT Photonics*). Several fiber types have been tested in this high power amplifier setup. First, variable polarization maintaining fibers with different core sizes (fiber types *YB1200-10/125DC-PM*, *Yb1200-12/125DC*,

Yb1200-20/125DC-PM, *Yb1200-20/400DC-PM* and *YB1200-25/250DC* by *nLIGHT*, formerly *LIEKKI*, with core sizes of 10, 12, 20 and 25 μm , respectively) have been implemented one by one in order to find out the optimum candidate for single mode operation with simultaneous high power capability. While fibers with a small core ($< 20\mu\text{m}$) have been melted during the operation with high pumping powers after several minutes, the fibers with large cores showed multi-mode operation with a modulated spectrum and a blurred beam profile due to the overlapping of different higher order modes. Eventually, a fiber with an additional photonic crystal fiber structure achieved the best results concerning mono-mode operation. The higher order modes are successfully suppressed thanks to the special fiber structure technology.

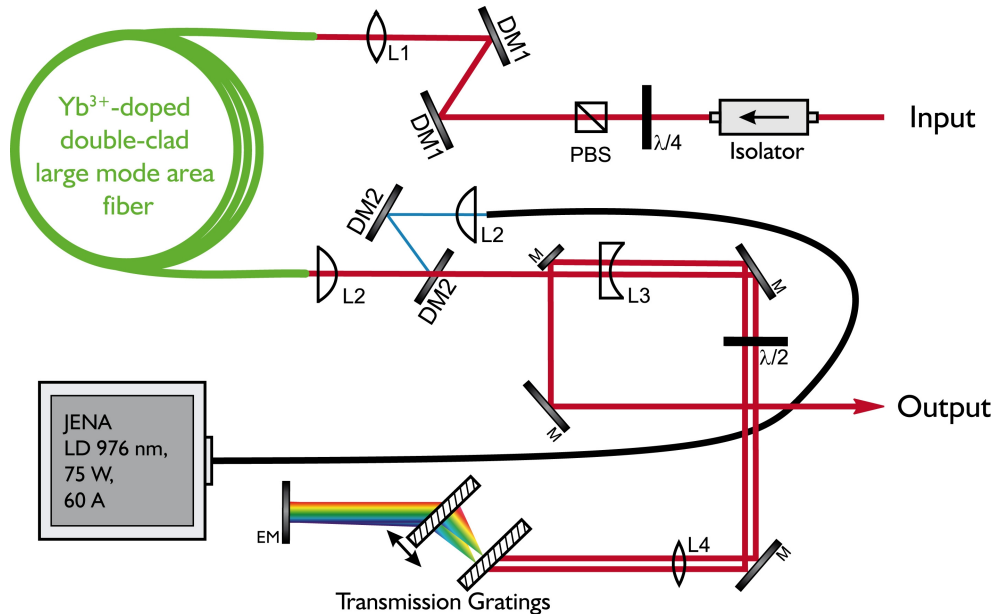


Figure 4.4: Setup of the Ytterbium amplifier. About 30 mW of signal laser light behind a protecting isolator is injected via an achromatic lens into the amplifier fiber, a polarizing double-clad large mode area Yb-doped fiber that preferably maintains the fundamental transverse electromagnetic mode (TEM₀₀) propagation. The amplifier is pumped in its backwards direction by a 70 W laser module emitting at 976 nm. A grating compressor reduces the durations of dispersion-managed pulses to less than 100 fs. The second passage through the grating compressor and the subsequent run of the amplified beam is indicated in this two-dimensional drawing by a collateral beam offset which is actually realized by tilting the end mirror EM downwards rather than sideways. Further abbreviations: DM dichroic mirror, M mirror, PBS polarizing beamsplitter, L lens.

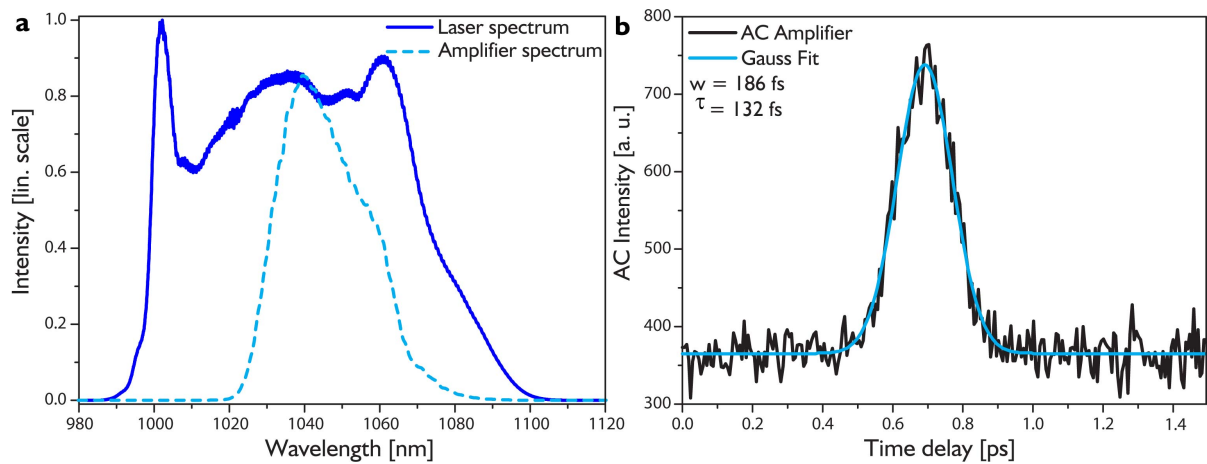


Figure 4.5: **a** Amplifier Spectrum (dashed light blue) and the original laser spectrum (dark blue) for comparison. On chart **b**: the corresponding auto-correlation (AC) trace for a 130 fs long pulse.

A powerful laser diode (up to 75 W of output power, corresponding to 55-60A of pump current) emitting at 976 nm is pumping the double-clad large mode area amplifier fiber in the amplifier's backwards direction. A combination of lenses and mirrors recollimates the amplified beam behind the amplifier and sends it to the grating compressor. This compressor consists of two transmission gratings and an end mirror that enables the light passing twice through the compressor. The compressor's transmission is about 60 % and it can compress the pulses to durations below 100 fs (for seeding signals in the dispersion-managed regime). The maximum average power after the amplifier and compressor was measured to be 14 W. However, this high power is not required in this experiment. Here, an average output power of 1 W was totally sufficient to get to a balanced signal in the interferogram behind the enhancement cavity.

Since pulses with positive dispersion are amplified, the compressor cannot provide a bandwidth-limited duration but the achieved duration of about 130 fs is still remarkable (see figure 4.5 b). The emitted spectrum is shown in figure 4.5 a together with the laser spectrum for comparison.

4.2.3 The enhancement cavity

The output of the amplifier behind the compressor is injected into the enhancement cavity after passing a mode-matching telescope consisting of two lenses ($f_1 = 100$ mm, $f_2 = 150$ mm) in order to convert the beam parameters to the ones of the cavity mode (beam waist

between the two focusing mirrors (with radius of curvature $r = 38$ mm each) $w_{0,1} = 7.3$ μm , beam waist in the collimated cavity arm $w_{0,2} = 637$ μm).

The enhancement cavity is implemented in a vacuum tank that serves as the gas chamber. Eight mirrors form the enhancing ring resonator with one tight focus. Its detailed setup is depicted in the photo in figure 4.6. Six of the eight cavity mirrors are high reflectors with a reflectivity of $R > 99.98$ %. The output coupler was chosen to be $R = 99.86\%$ in order to provide a leaking beam strong enough for the later beating signal. The input coupler was finally determined by considering the impedance matching condition for optimum coupling into the cavity. It's value was calculated to be $R = 99.74$ % (see equation 2.20 for impedance calculation and appendix A for detailed reflectivity curves of the cavity mirrors).

This impedance-matched configuration of the cavity mirrors theoretically results in a high finesse of $\mathcal{F} > 1200$ and in a power enhancement factor of $P_{IM} = 385$ (see equations 2.21 and 2.22). The path length where the laser can interact with the gas is hence increased by a factor of 385 to more than 900 m since the actual length of the ring cavity accounts for 2.34 m.

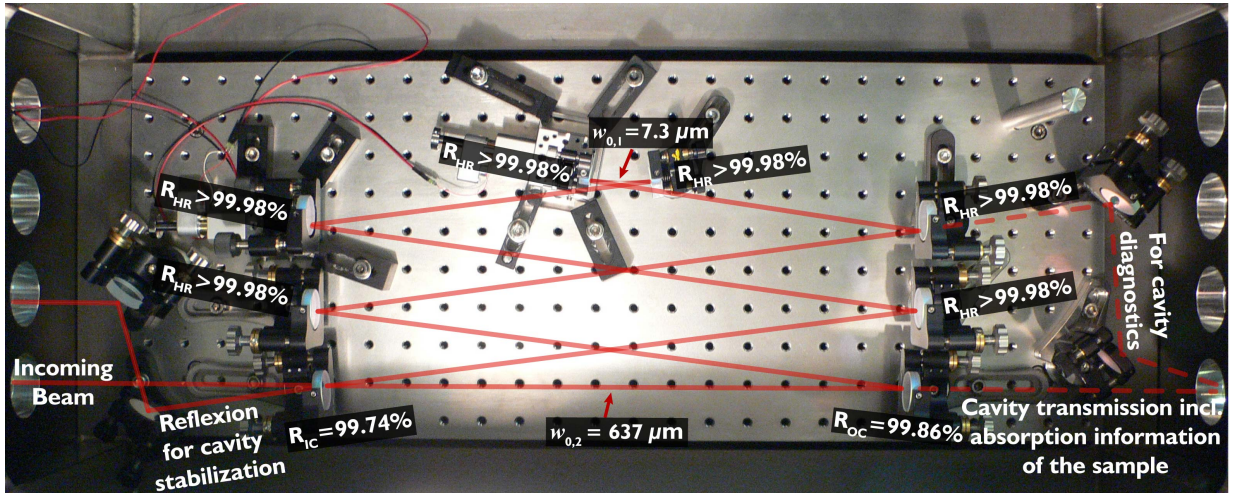


Figure 4.6: Photography of the enhancement cavity in the gas chamber. Eight mirrors form a ring cavity. The individual values of the mirror's reflectivities can be taken directly from the photography. The two beam waists of the cavity $w_{0,1}$ and $w_{0,2}$ mentioned in the text are also marked.

Stabilization

As already explained in detail in chapter 2.4.3, one has to make some efforts to achieve this theoretically possible enhancement in the experiment: the laser has to be actively stabilized to the cavity (or vice versa) in order to get constructive interference of the pulses inside the cavity. This is accomplished by the adjustment of the cavity length of the laser. There exist several techniques for such a stabilization like the wide-spread polarization-dependent Hänsch-Couillaud locking scheme [59]. Here, the so-called Pound-Drever-Hall lock showed to be more reliable because of its insensitivity in polarization and alignment [60].

Since the stabilization of the laser to the cavity is as important as the stabilization of the frequency combs in the previously presented experiment, it is worth to explain in detail the achievements of the locking technique. Eventually, only a proper stabilization circuit will enable a broadband power enhancement and, hence, a high detection sensitivity over a wide spectral range. Furthermore, the feedback loop should be able to filter out any frequency noise that otherwise would be converted into intensity noise in the interferogram. The implementation of the stabilization scheme is shown in figure 4.7.

The light that is reflected by the cavity input coupler is used to produce an error signal

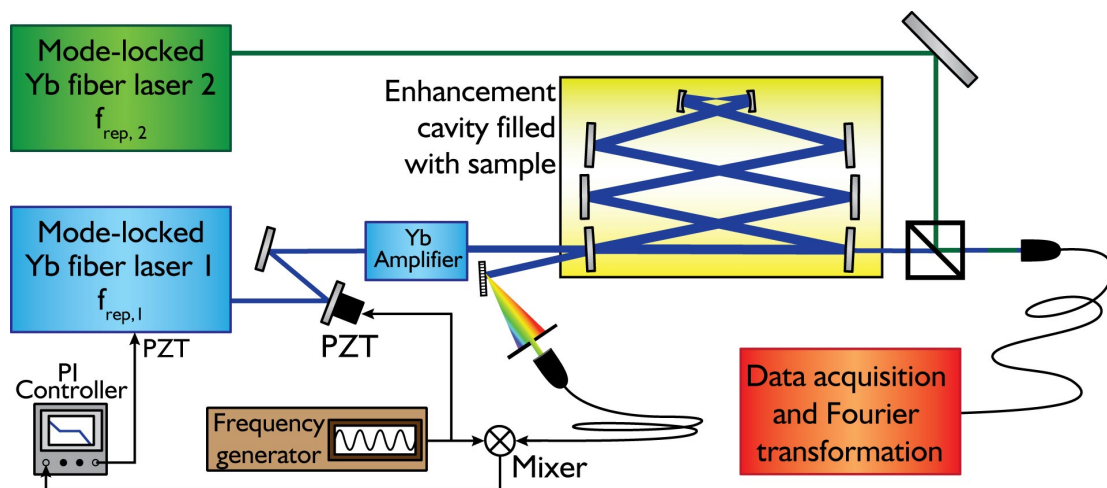


Figure 4.7: Scheme for the Pound-Drever-Hall stabilization. The light that is reflected by the cavity is used to generate an error signal by mixing it with a modulation frequency originating from a function generator. The same modulation frequency is used to produce sidebands next to the repetition rate via a piezo-electric transducer (PZT) behind the laser output port. The mixed signal forms the error signal that is sent to a proportional plus integral (PI) controller which in turn creates the controlling signal for the laser PZT.

that indicates the mismatch between the lengths of the enhancement cavity and the laser cavity. For this purpose, the back-reflected light is diffracted by a grating and filtered by a slit for wavelength selection of the locking point before it is detected by a photodiode. The use of the grating also results in a better signal-to-noise ratio of the error signal. This error signal originates from sidebands of the repetition frequency that are generated via a mirror on a piezo-electric transducer (PZT) directly behind the laser's output. The PZT modulates the phase of the laser beam with a frequency of 668 kHz which is a resonance of the PZT. The light that is reflected by the cavity is then compared with the same modulation frequency produced by a function generator. The comparing mixer extracts the part that is at the same frequency as the modulation signal and generates an error signal. A proportional plus integral controller feeds back the error signal to a piezo-electric transducer with 45 kHz bandwidth inside the laser resonator and maintains the system on resonance.

This locking scheme enables to meet number 2 of the three conditions presented in chapter 2.4.3 for an optimum enhancement, the adaptation of the laser repetition rate with the inverse of the cavity round trip time. The first condition prescribes a cavity dispersion as low as possible for a preservation of the pulse shape inside the cavity. This is achieved by the selection of cavity mirrors with low group-delay dispersion (GGD). To be more precise, the GDD of all mirrors together does not exceed -10 and $+35$ fs² for the crucial region of the amplified laser spectrum between 1030 nm and 1065 nm ((FWHM, see appendix A for detailed dispersion curves of the cavity mirrors). The third condition of the adjustment of the comb's offset frequency for phase matching is realized by displacing a wedge pair (not represented in figure 4.2) inside the laser cavity to improve the overlap of the comb frequencies with the cavity modes.

Figure 4.8 shows the transmitted spectrum of the locked cavity with the comb's offset frequency optimized. For comparison, the amplifier spectrum that was injected to the cavity is also depicted. The cavity filtering is mainly due to the dispersion inside the cavity (introduced by the mirrors and the gas inside the cavity) but also due to the limited bandwidth of the phase-locked loop which still can be optimized. The intra-cavity dispersion could be decreased by a proper design of one or more chirped mirrors that exactly compensate the dispersion introduced by the other cavity components and the gas. A faster servo loop can be realized by the implementation of a faster PZT or an electro-optical modulator inside the laser resonator.

Despite the narrowing effects of dispersion and limited servo-loop bandwidth, a spectrum

broader than 25 nm could still be enhanced with this setup design enabling a broadband multiplex examination of the sample lines.

To finally overlap the beam that is transmitted through the cavity with the output of the second laser onto the photodetector with an optimum balance, a fiber combiner with the ratio 10:90 was chosen (in figure 4.1 depicted as a beam cube for sake of simplicity). This special ratio ultimately adapts the power contributions of the leaking light of the cavity and the light of the second frequency comb (90 % and 10%, respectively). In addition, by coupling the free-space laser outputs into the two fiber input ports of the combiner via simple achromatic lenses, the different beam sizes and divergence angles are automatically adjusted for an optimum overlapp without the need of complex mode-matching telescopes. After these arrangements of an optimum matching of the beams in both size and power ratio, the beating signal is sent to a fast photodiode. A low pass filter of 70 MHz that is attached to the photodiode provides non-redundant information. The signal is finally amplified and digitized by a high resolution digitizer on a personal computer (same models for amplifier, acquisition board and computer as used in chapter 3.2.1).

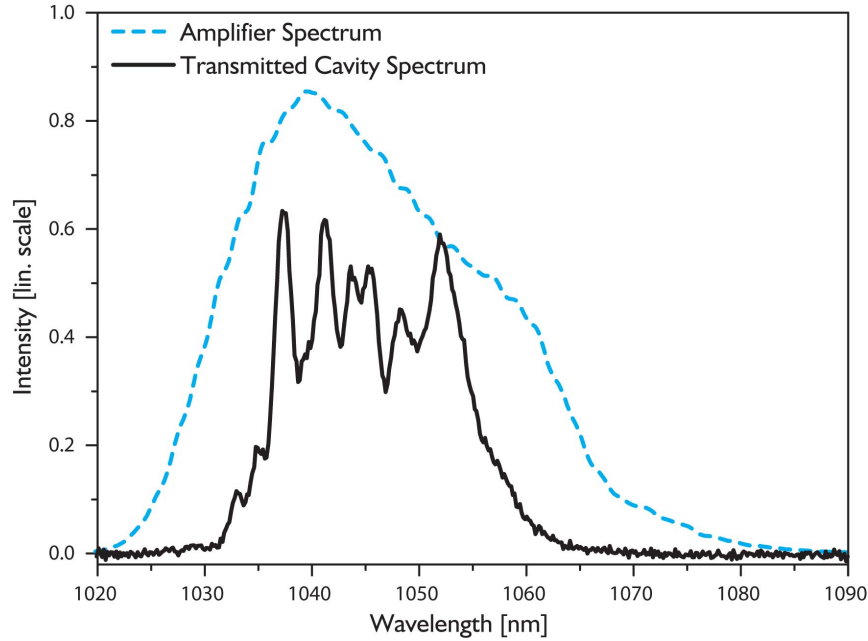


Figure 4.8: Spectrum transmitted through the locked cavity (black). The irregular slope is due to the measurement: The spectrum is detected with an *Ocean Optics* spectrometer via a multimode fiber wherein higher order modes are excited and consequently a modulated spectrum is generated. For valuation of the wavelength range supported by the cavity, the incident amplifier spectrum (dashed blue) is also shown. The cavity filters the spectrum due to remaining cavity dispersion and upgradable locking conditions.

4.3 Results and discussion

As the first sample, the well investigated gas of acetylene (C_2H_2) was chosen since it can give a detailed statement about the performance quality of the new dual comb spectrometer by comparing the first results with the already available spectroscopic data in the HITRAN data base, for example [7]. The $3\nu_3$ band region of acetylene has already been studied in particular because of its relatively strong line strengths and its usefulness in frequency metrology [98].

In the first experiment, 3 mbar of acetylene was filled into the cavity chamber. After stably locking the laser to the cavity, an interferogram of the two Yb frequency combs was recorded. Its acquisition took only 23 μs and the corresponding trace is displayed in figure 4.9.

This unapodized interferogram leads to a spectrum after its Fourier transformation, with a resolution of 4.5 GHz. The burst, arbitrarily set to 0 μs , corresponds to the overlap of two

pulses of the two Yb frequency combs on the photodetector. The inset shows an enlarged view of the burst episode. After the burst, for times longer than $1 \mu s$, the interferometric signal exhibits the typical modulation originating from the molecular lines. It only occurs on one side of the burst since the absorbing sample held in the high-finesse resonator interacts with only one of the two combs.

Fourier transforming the single time-domain sequence without averaging depicted in figure 4.9 reveals the absorption spectrum. It resolves the rovibrational lines with a good signal-to-noise ratio of $SNR \approx 100$ (see figure 4.10). As already mentioned, the unapodized resolution is 4.5 GHz and the spectral span ranges from 1025 nm to 1050 nm. The interferogram was recorded within $23 \mu s$ which results in a minimum detectable absorption coefficient of $\alpha_{min} = 8 \cdot 10^{-8} \text{ cm}^{-1}$ and a noise equivalent absorption coefficient at 1 s averaging of $NEA = 5 \cdot 10^{-10} \text{ cm}^{-1}\text{Hz}^{-1/2}$ (see equations 2.3 and 2.4 for value calculation). As second species, ammonia (NH_3) was chosen to be investigated. This time, 50 mbar of NH_3 were filled into the cavity chamber. To match the region of its absorption lines, the center of the cavity transmission spectrum is shifted to 1045 nm by rotating the grating in front of the photodiode used for the Pound-Drever-Hall lock (see figure 4.7). To the best of our knowledge, the $3\nu_1$ band of NH_3 has never been rotationally resolved before. However, the requirement for such a spectral insight has been recognized [99, 100], in particular for the radiative transfer modeling of the atmosphere of Jovian-like planets.

In figure 4.11, the recorded NH_3 spectrum is displayed. The shift in the locking point resulted in an increased SNR of 380. Here, the cavity transmission spectrum spans 20 nm with an unchanged resolution of 4.5 GHz. The acquisition time was only $18 \mu s$. Hence, an even better minimum detectable absorption coefficient of $\alpha_{min} = 3 \cdot 10^{-8} \text{ cm}^{-1}$ and a noise equivalent absorption coefficient at 1 s averaging of $NEA = 1 \cdot 10^{-10} \text{ cm}^{-1}\text{Hz}^{-1/2}$ could be achieved.

The comparison of these values for the sensitivity shows that the presented method is more sensitive by more than two orders of magnitude compared to our previously demonstrated experiment with the single-pass cell (compare with chapter 3.2.3). Moreover, this technology outperforms the hitherto state-of-the-art experiment that also involves a high finesse cavity for increased sensitivity [70]. In the cited experiment, a broadband frequency comb is coupled into a high-finesse optical cavity (Finesse $\mathcal{F} = 4500$) to create the simultaneous ring-down decay of the individual cavity modes. The different modes are detected by a CCD camera combined with a grating monochromator and a scanning mirror that generates a time and wavelength resolved image. The resolution of the setup (25 GHz) is limited

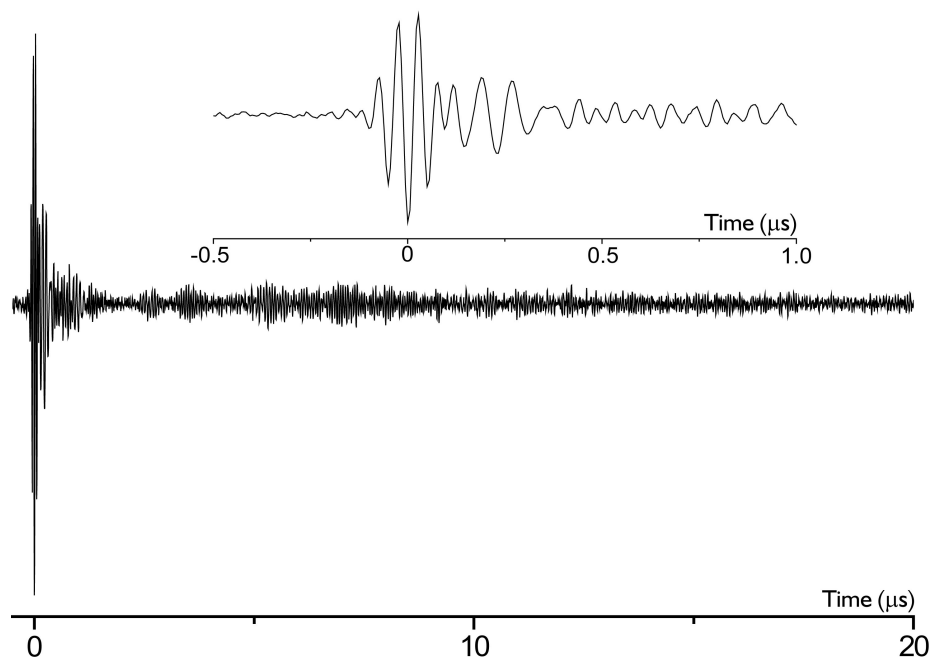


Figure 4.9: The time-domain interferogram. A burst occurs when two pulses of the two frequency combs overlap on the detector. The signal modulation after the burst is due to the molecular lines of the gas sample.

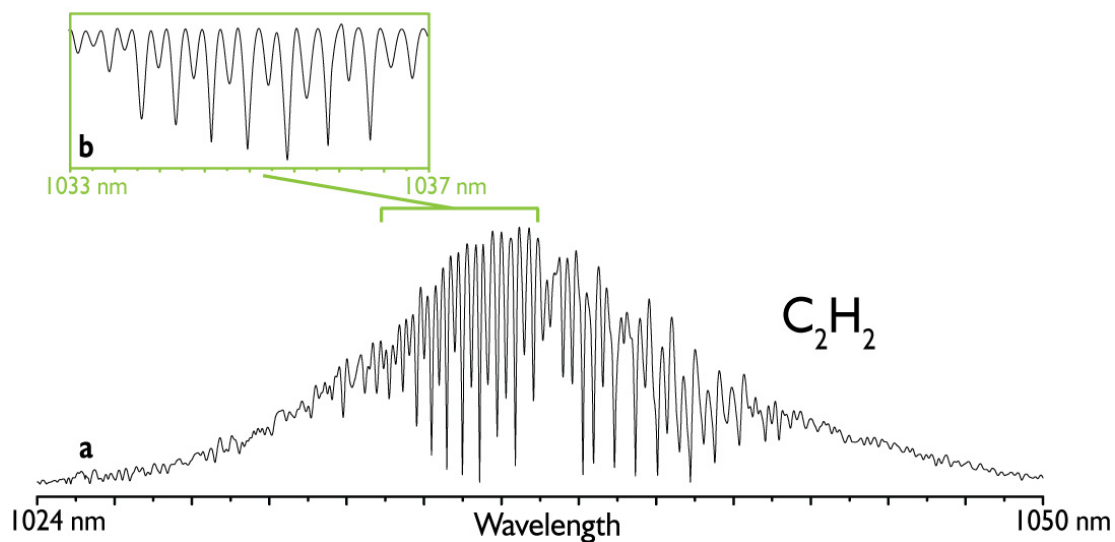


Figure 4.10: Absorption spectrum of acetylene. The enhanced laser spectrum extends from 1025 to 1050 nm. The intensity alternation arises from the $3\nu_3$ vibrational band of C_2H_2 centered at 1037.4 nm. The inset b shows signatures around 1035 nm affiliating to the R-branch (from R(19) to R(1)).

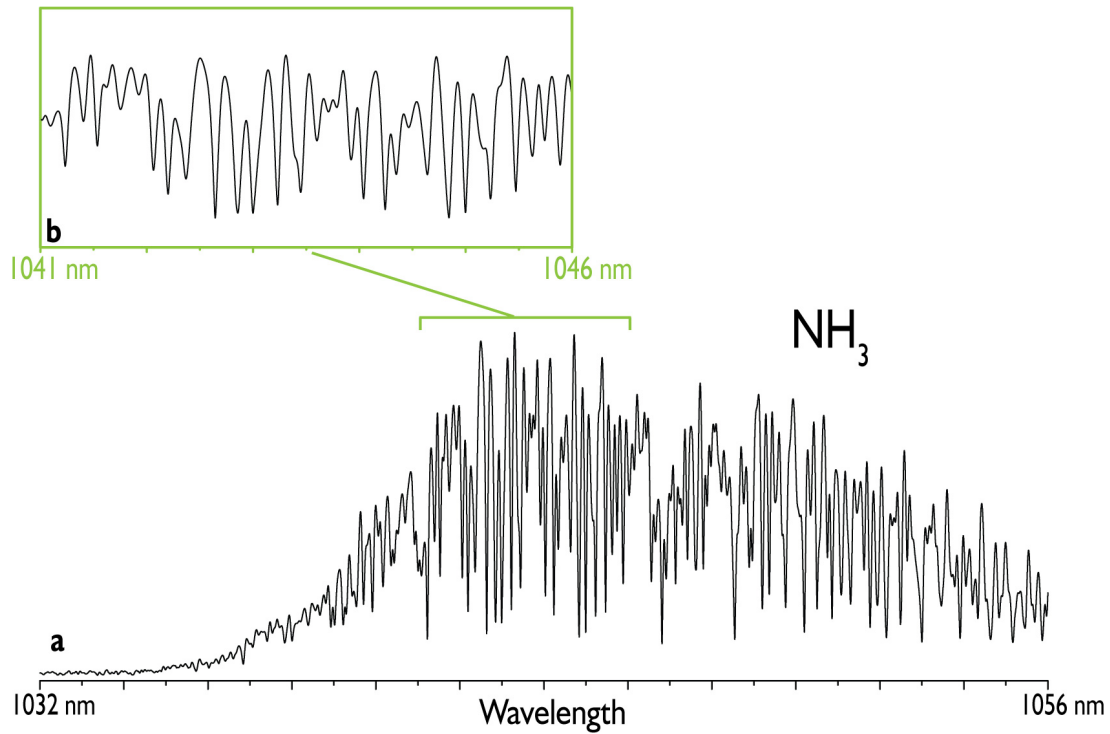


Figure 4.11: Absorption spectrum of ammonia. To our knowledge, the weak transitions of the $3\nu_1$ overtone band of NH₃ are observed for the very first time.

by the monochromator. A 15 nm broad spectrum could be coupled into the cavity (laser wavelength centered at 800 nm). Besides the monochromator resolution, the speed of the scanning mirror was the major limiting issue that could only provide acquisition times not shorter than 1.4 ms. With this setup, a minimum detectable absorption coefficient of $\alpha_{min} = 6.3 \cdot 10^{-8} \text{ cm}^{-1}$ could be realized. The comparison of these results with the achievements of the static dual comb spectrometer presented in this thesis exposes a 20-fold better minimum detectable absorption coefficient α_{min} and an almost 100-fold shorter measurement time.

Nevertheless, further improvements can even advance the recent results. For example, the signal-to-noise ratio could be enhanced by a superior matching of the cavity modes with the comb teeth during the acquisition time with a faster servo-control loop. In addition, the SNR could benefit by a better adjustment of the combs' pulse durations: in the presented experiment, the first frequency comb probing the sample with about 100 fs short pulses is beating with the second frequency comb that generates unequally long pulses in the ps range. By inserting a pulse compressor behind the second frequency comb in order

to adapt the pulse durations, the SNR can easily be further enhanced without large effort. The spectral bandwidth of the experimental technique is presently limited by the cavity mirrors but the experimental principle allows for the measurement of octave spanning spectra. The spectral broadening of the frequency comb output can be achieved by nonlinear optical fibers. In order to qualify the cavity to enhance broader laser spectra, the cavity mirrors would need to feature an even lower group delay dispersion (GDD) or chirped cavity mirrors would have to be implemented that compensate the cavity GDD by special coating designs. However, a well adapted broadband GDD design of the mirrors requires an elaborate iterative development [101].

The presented method of enhancing the sensitivity with an external cavity involves the requirement of a fast stabilizing feedback loop. Since its implementation can be challenging, using a multipass cell could be a more convenient alternative approach, although less powerful.

However, if the effort of implementing a phase locked loop can be made, stabilizing both degrees of freedom of the lasers would additionally increase the resolution like already demonstrated in the previous chapter (see part 3.2.3 for details) and in [77,81]. With the technique of interleaving successive spectra, an extremely high resolution can be reached that is only limited by the width of the comb lines (i.e. on the order of kilohertz).

With the presented setup, excellent sensitivities have been reached enabling the usage of dual comb spectroscopy for trace gas detection. An alternative approach to reach such high sensitivities would be the implementation of the new dual comb method in the mid infrared wavelength range where the stronger fundamental rovibrational lines of molecules are located. A possible concept for such a realization is presented in the subsequent chapter.

Chapter 5

Dual comb spectroscopy in the mid-infrared region

5.1 The mid infrared - the molecular fingerprint region

After the demonstration of two realizations of dual comb spectroscopy in the near infrared region, the large versatility of this new technique has become evident.

This technique gains in importance when it is realized with laser sources in the mid-infrared region (MIR). Molecules exhibit their fundamental and, hence, strong rovibrational lines in the range of about 2 to 20 μm which is called the fingerprint region since the molecules show unique characteristics in this range. In the hitherto examined near infrared region, only overtone transitions occur that are weak by nature. Therefore, the detection level of the new method automatically decreases, i.e. improves, if it is transferred to the mid-infrared wavelength range.

Up to now, the lack of easily manageable laser sources in the mid-infrared has prevented an easy implementation of frequency comb Fourier transform spectroscopy in the fingerprint region. The very first implementation of the promising method has been demonstrated in the mid-infrared at 10 μm , but because of the utilized process of optical rectification, only very weak powers on the order of μW could be achieved which resulted in a poor signal-to-noise ratio [102]. Since this first realization, other sources, based on difference frequency generation [103], optical parametric oscillation [104] or on Cr^{2+} -doped chalcogenide fibers [105] have been developed and look promising to get established as the com-

mon source for MIR dual comb spectrometers.

Another interesting candidate is a solid-state laser that is based on Cr^{2+} doped ZnSe polycrystalline active media. Its mode-locking operation with sub-100-fs pulses was demonstrated in 2006 [52] and its suitability as high-brightness spectroscopic source has already been demonstrated with a Michelson-based Fourier transform spectrometer [106]. In the experiment presented in this chapter, two similar $\text{Cr}^{2+}:\text{ZnSe}$ lasers have been utilized for the first time to realize a dual comb spectrometer in the mid-infrared [107]. For this purpose, Evgeni Sorokin from the *Institut für Photonik, Vienna, Austria* and Irina Sorokina from the *Norwegian University of Science and Technology, Trondheim, Norway* visited the MPQ for two weeks with two twin $\text{Cr}^{2+}:\text{ZnSe}$ lasers that have been developed by themselves over the past years.

5.2 Experimental Setup

The setup is similar to the Fourier spectroscopy experiment with erbium lasers that was presented in chapter 3.2.1. In the current experiment, two similar $\text{Cr}^{2+}:\text{ZnSe}$ lasers emitting both at about $2.4 \mu\text{m}$ but with slightly different repetition rates ($\Delta f_{\text{rep}} \approx 400 \text{ Hz}$) are overlapped via a germanium coated fluorine beam mixer.

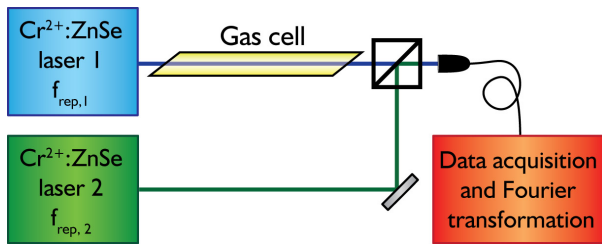


Figure 5.1: Experimental setup of the Fourier transform spectroscopy experiment with two fs lasers in the mid-infrared.

Before the superposition of the two laser beams, the first laser is interrogating a gas sample located in a single-pass cell (see figure 5.1).

The gas cell is 70 cm long and filled with 230 mbar of acetylene. The interferometric signal is detected with an InGaAs photodiode that has a bandwidth of 60 MHz. This signal is sampled with the high-resolution 16-bits-digitizer with 65 MHz bandwidth at a rate of 180 megasamples per second that

has already been utilized in the two fore running experiments (see chapter 3.2.1 for model details).

The two lasers share one pumping laser, a continuous wave Erbium-doped fiber laser emitting at $1.61 \mu\text{m}$ (by *IPG Photonics*, up to 5 W output power). Their detailed setup is

explained in the following subchapter since this type of fs pulse generation in the mid-infrared region is still not commonly known.

5.2.1 The $\text{Cr}^{2+}:\text{ZnSe}$ lasers

The two lasers that are both based on a 2 mm thick Brewster-cut polycrystalline $\text{Cr}^{2+}:\text{ZnSe}$ active medium (doping concentration $5 \cdot 10^{18} \text{ cm}^{-3}$, respectively) are each pumped by 1.9 W originating from a single Erbium-doped fiber laser emitting at 1607 nm. The astigmatism-compensated Z-folded cavities consist each of two curved dichroic mirrors (radius of curvature $R_c = 75 \text{ mm}$ and 50 mm , respectively) for incoupling the pump light and for focusing into the gain crystal, a third curved mirror ($R_c = 45 \text{ mm}$) for focusing onto an InAs/GaSb semiconductor saturable absorber (SESAM) and an output coupler with a transmission of 2 % at $2.4 \mu\text{m}$ for both lasers (see figure 5.2). Dispersion compensation is achieved by a 3 mm thick sapphire plate. The self-starting mode-locking operation is ensured by the SESAM. The repetition rates of the lasers are set to 215 MHz while differing in total by about 400 Hz. Both lasers have an output power of about 50 mW each.

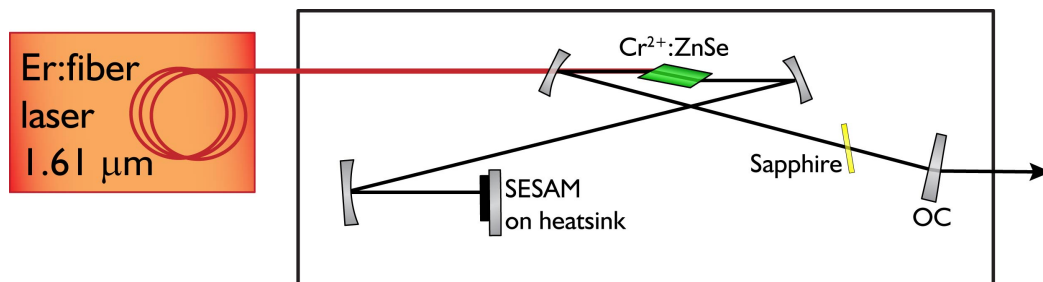


Figure 5.2: Setup of the $\text{Cr}^{2+}:\text{ZnSe}$ lasers. A $\text{Cr}^{2+}:\text{ZnSe}$ crystal is pumped by a continuous wave Erbium-doped fiber laser. The z-type laser cavity includes a sapphire plate for dispersion management and a SESAM for mode-locking.

The generated 60 nm broad laser spectrum is shown in figure 5.3. It is centered at 2435 nm and exhibits a large cw peak that is due to unclean mode-locking operation. The peak could be removed by decreasing the pump power at the expense of the stability of the mode-locking operation. Hence, during the measurement, the cw peak was present resulting in a larger noise in the interferogram.

In addition, the spectrum shows dispersive lines corresponding to intra cavity water vapor lines [108]. Besides the fundamental laser radiation, the oscillator also emits pulses at the

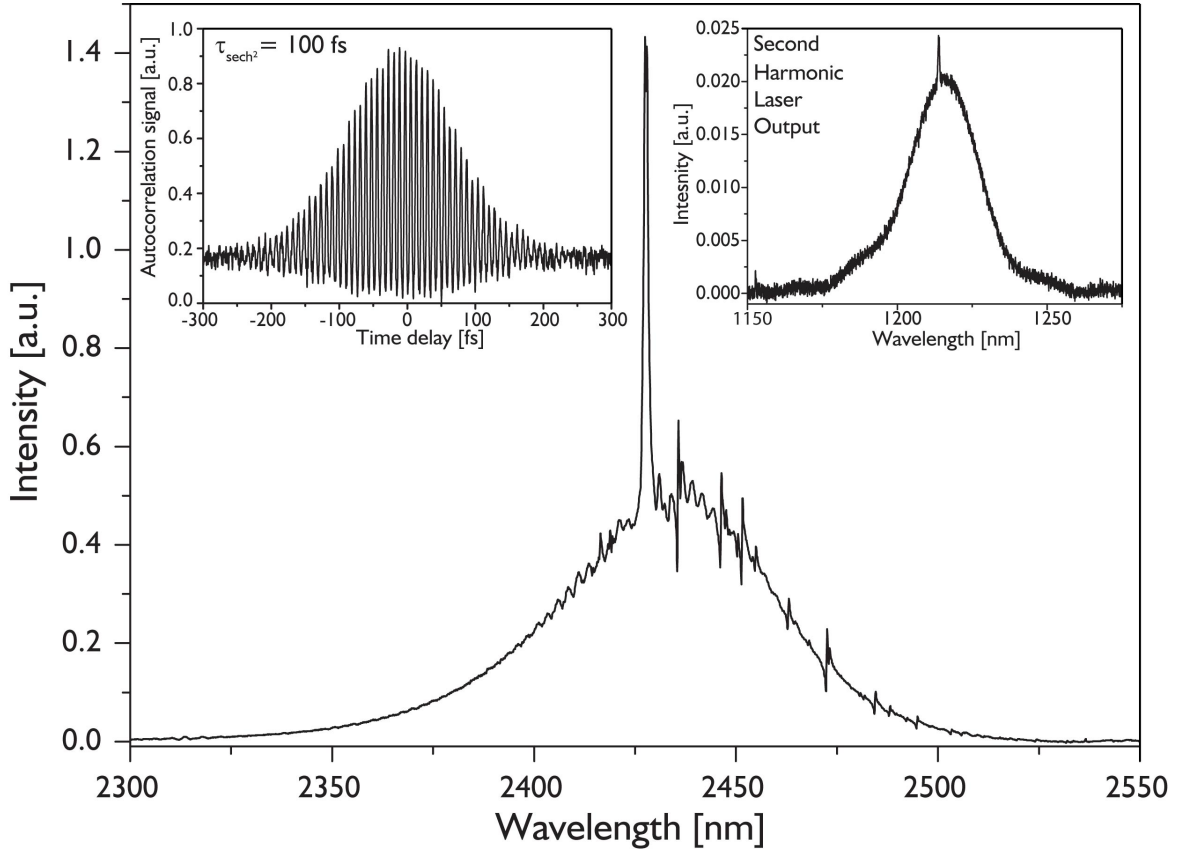


Figure 5.3: Laser spectrum and auto-correlation trace. The laser is emitting a 60 nm broad spectrum (FWHM) centered at 2435 nm. The laser additionally exhibits second harmonic radiation shown in the right inset. Both spectra feature a cw peak arising from suboptimal laser operation. The interferometric auto-correlation trace shown in the left inset exposes a pulse duration of 100 fs.

second harmonic centered at about 1218 nm (see right inset in figure 5.3). Its average power is about 10-20 μW or about 10^{-4} of the fundamental signal. The generation of the second harmonic is due to quasi-phase-matching processes in the multi-crystalline gain material (see [109] for more details).

The left inset of figure 5.3 shows the auto-correlation (AC) trace measured by a collinear auto-correlator using two-photon absorption in an InGaAs photodiode. The full width at half maximum (FWHM) of the AC trace is about 190 fs which corresponds to a pulse duration of 100 fs since the pulses have a sech^2 shape (total negative intra cavity dispersion).

5.3 Results and discussion

Beating the two fs lasers with different repetition rates on a photodiode results in an interferogram depicted in figure 5.4. The bursts arising from the simultaneous overlap of the pulses from the two fs lasers on the photodiode are expected to have a separation that is proportional to the inverse of the difference in repetition frequencies of the lasers Δf_{rep} . Since this value is $\Delta f_{rep} = 400$ Hz, the bursts should be separated by 2.53 ms. Taking a closer look at the interferogram reveals a doubly-periodic structure with an additional set of bursts that is shifted by about 1.075 ms. These second bursts originate from the fact that one of the lasers could only run stably in a double-pulse regime. This double-pulsing could not be retrieved in the auto-correlation trace since the two pulses are effectively separated by $1.075 \text{ ms} \cdot \frac{400 \text{ Hz}}{215 \text{ MHz}} \approx 2 \text{ ns}$ which corresponds to an optical delay of 60 cm. However, this regime is not disturbing the interferometric measurement since the modulation due

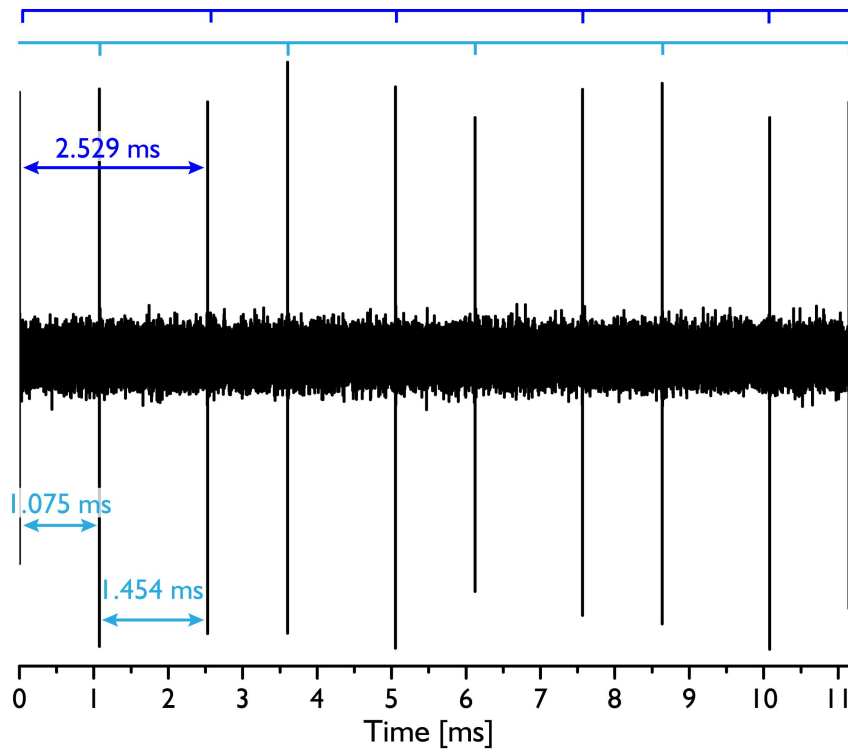


Figure 5.4: The time-domain interferogram. The sequence of 11.2 ms reveals a double periodic structure of the bursts (enlightened in dark and light blue) due to double-pulsing by one of the two fs lasers (see text for details). The Fourier transform of a $10 \mu\text{s}$ unweighted interferogram leads to a spectrum with 12 GHz unapodized resolution. Hence, the double periodic structure in the interferogram has no influence on the measurement.

to the molecular transitions only occurs on one side of the interferometric bursts (that is because only one laser beam interacts with the sample) on a scale of ten microseconds. In fact, achieving double-pulsing could even be of interest for time-resolved sequences because the increased burst rate with simultaneously reasonable cavity lengths would enlarge the temporal resolution of dynamic single events.

The rovibrational spectrum of acetylene at 2450 nm is chosen to demonstrate the capability of the new mid-infrared spectrometer for broadband absorption spectroscopy. Figure 5.5 depicts the absorption spectrum in the region of the $\nu_1 + \nu_5^1$ band after the Fourier transformation of the interferogram. The P, Q and R branches are clearly distinguishable while the intensity alternation is obvious as can be seen in the left inset of the figure. The spectrum is retrieved from a Fourier transform of a 10 μs long sequence of the interferogram shown in 5.4, without averaging several interferogram sequences. The dual comb spectrum reaches from 2370 to 2525 nm with an unapodized resolution of 12 GHz. Numerical apodization was performed in the displayed spectrum with a Blackman-Harris function that strongly

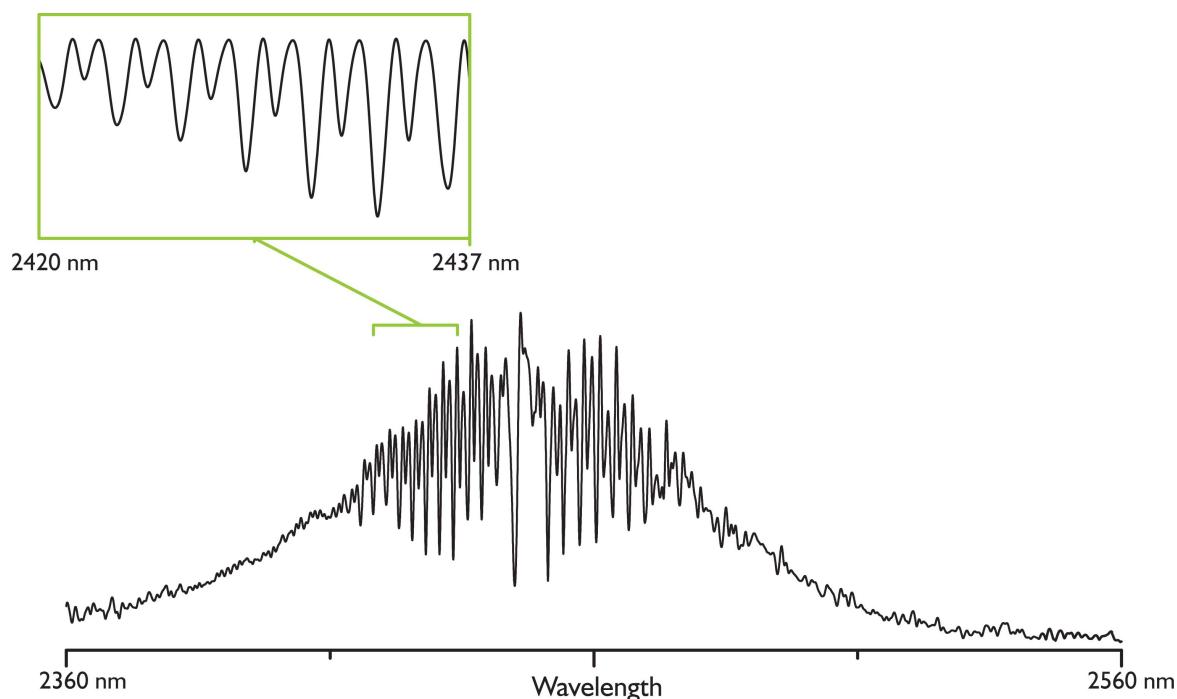


Figure 5.5: Mid-infrared absorption spectrum of acetylene showing the $\nu_1 + \nu_5^1$ combination band. The laser spectrum extends from 2370 nm to 2525 nm with an unapodized resolution of 12 GHz after Fourier transformation of a 10 μs long interferogram sequence. The inset shows the alternating signature at around 2430 nm belonging to the R branch (from R(17e) to R(5e)).

suppresses the sidelobe amplitude in the interferogram.

A signal-to-noise ratio of 50 could be reached. Hence, a minimum detectable absorption coefficient of $\alpha_{min} = 2.9 \cdot 10^{-4} \text{ cm}^{-1}$ and a noise equivalent absorption coefficient at one second averaging of $NEA = 9.0 \cdot 10^{-7} \text{ cm}^{-1}\text{Hz}^{-1/2}$ could be achieved (see equations 2.3 and 2.4 for value calculation).

The value for NEA is relatively poor since both the absorption path and the signal-to-noise ratio still require improvements but also because the combination bands of C_2H_2 in this region are quite weak: their intensity of the order of $10^{-21} \frac{\text{cm}}{\text{molecule}}$ is on the same order than the intensity of transitions in the infrared $1.5 \mu\text{m}$ region. Besides the improvement in absorption length and signal-to-noise ratio (for example by utilizing also here an enhancement cavity as gas cell as it was realized in the previous chapter 4), the operation of the $\text{Cr}^{2+}:\text{ZnSe}$ lasers need a further development for an overall amelioration of this experiment. The fragile stability of the lasers enabled only a successful proof-of-principle operation rather than a convincing final implementation. Their mode-locking operation was permanently an issue during the measurements and, hence, represents the main sensitivity and reliability limitation of this new dual comb spectrometer in the mid-infrared. As a result for the restricted possibilities in laser operation during the limited time of the measurement campaign, a compromise had to be found between the signal-to-noise ratio and the resolution of the individual rovibrational lines in the computation.

However, $\text{Cr}^{2+}:\text{ZnSe}$ lasers in principle allow much longer-term hands-free stable operation as it could be achieved in this experiment. One of the most interesting promises of $\text{Cr}^{2+}:\text{ZnSe}$ as the active medium is the availability of technologically developed and low-cost polycrystalline material that can be manufactured with arbitrary sizes for potential scaling in the output power. The combination of the $\text{Cr}^{2+}:\text{ZnSe}$ ceramic gain media with diode lasers as pump sources hold promise to make these lasers the most practical, compact and cost-efficient femtosecond lasers in the mid-infrared region in the future. The resolution of this mid-infrared dual-comb spectrometer can then be improved to a limit that is given by the width of the comb lines just by increasing the acquisition time like it was done in chapter 3.2.3.

Increasing the measured optical domain would also be a desirable issue. Since the enormous gain bandwidth of $\text{Cr}^{2+}:\text{ZnSe}$ lasers exceeds 850 nm (FWHM), a much broader spectral region could be observed simultaneously either by tuning or, even superior, by developing a few-cycle laser with an optimized Kerr-lens mode locked configuration. Highly non-linear fibers can also provide a broadened spectrum in this wavelength region as already demon-

strated with chalcogenide [105] and ZBLAN [110] microstructured fibers.

In the last years, the lack of frequency comb sources in the mid infrared region has been tackled also with other approaches that all, however, require further developments. Difference frequency generation in GaSe crystals enabled to shift the output of Ti:sapphire lasers to 9-12 μm [78]. By mixing a near infrared femtosecond laser with a near infrared continuous wave laser in a periodically poled lithium-niobate crystal, a frequency comb at 3 μm was successfully generated (ranging from 2.9 to 3.5 μm , [103]). However, these realizations only provide poor power levels of a few μW in the MIR region and the coherence of recently generated combs with higher output powers on the mW level still needs to be proven [111]. Optical parametric oscillators can supply more power (for example in the 2.8 to 4.8 μm region, [104]) but exhibit a complicated setup. A recent experiment could generate an average power of 1 W in this wavelength range corresponding to a power of 1-10 μW per comb line [112]. The smallest MIR comb so far with equal output power has been generated via four-wave-mixing in a MgF_2 microresonator generating a comb centered at 2.45 μm promising compact and convenient MIR comb sources in the future when the problem of significantly differing relative intensities will be solved (≈ 20 dB difference between cw pump mode, center and marginal comb modes, respectively, see [113]).

Chapter 6

Towards frequency comb Fourier transform spectroscopy in the XUV

6.1 The extreme ultra-violet wavelength region

The wavelength region of the vacuum ultraviolet (VUV, 100 nm - 200 nm) and the extreme ultraviolet (XUV, 10 nm - 100 nm) is a spectral range that is difficult to access with laser sources. Especially below 120 nm, there is a lack of powerful single wavelength lasers or media for transferring the output of lasers with a higher fundamental wavelength into the XUV.

However, universally extending the broad application field of Fourier transform spectroscopy also to the VUV and XUV region is an appealing enterprise. The FTS technique is the leading spectroscopic tool in the mid-infrared region because of its simultaneous features of high resolution and wavelength accuracy over a broad spectral range. It is desirable to transfer all these convincing properties to a similar spectrometer in the VUV and XUV since this spectral region is still partially unexplored due to the lack of laser sources and spectroscopic instruments. Especially the Doppler-limited resolutions will enable unprecedented insights into the rotational structure of the absorption bands of light molecules of atmospheric (N_2 , O_2 , ...) and astrophysical interest (H_2 , O_2 , C_2H_2 , ...). This high resolution is essential to measure the cross sections of the photoabsorption lines of molecular species without instrumental artifacts in order to precisely study and model the different planetary atmospheres and interstellar clouds [114].

Not only the lack of a suitable light source is a problem to solve. Traditional Fourier transform spectrometers are based on the Michelson interferometer and hence all have a

beamsplitter in their setup in order to recombine the two beam paths of the fixed and the scanning interferometer arm. The manufacture of beamsplitters for the UV, however, is difficult or even impossible for wavelengths below 140 nm. This difficulty is the reason why Fourier transform spectroscopy could not be extended to spectral regions beyond this limitation for a long time.

Very recent innovations have overcome the beamsplitter issue by transferring an approved geometric design into the UV range as will be explained in the following subsection. While large synchrotron facilities are often employed for the XUV generation, it would be more convenient to have a more compact table-top system. In recent years, there have been a few XUV frequency comb realizations that are manageable systems extending only a few square meters in a laboratory. Since these systems feature interesting advantages compared to big XUV facilities, such a source has been realized also in the framework of this thesis in order to implement the innovative frequency comb Fourier transform spectroscopy in the rather unexplored VUV and XUV region.

6.1.1 XUV sources and their spectroscopic applications

Fourier transform spectroscopy is an established technique not only in the IR and in the visible but also progresses into the direction of the VUV and, most recently, to the XUV range. For many years, the wavelength range was limited to 178 nm because of the generally used silica beamsplitter in the spectrometer setup [115]. The development of a MgF_2 beamsplitter shifted the wavelength cutoff for FTS to 140 nm [116]. Very recently, this wavelength limit was again shifted by a large amount to 40 nm with a new wavefront-division scanning interferometer [117]. The new device is based on a Fresnel bimirror where the two halves of the wavefront are incident on the reflecting surfaces. One of the prisms is slightly tilted in order to produce interference fringes. The other prism is scanned to change the path difference and to generate an interferogram.

In all the mentioned FTS realizations, large facilities have been used as light sources such as the synchrotron source SOLEIL in Gif-sur-Yvette, France [118]. It would be more straightforward if the light source was of much smaller size enabling a more compact setup. It is possible to produce UV radiation via nonlinear processes such as frequency mixing techniques or high harmonic generation (HHG). For instance, with resonance-enhanced four-wave mixing, a broadly tunable VUV and XUV source down to 62 nm has been realized in argon with a power level of milliwatts [119]. With this laser source, high resolution spectroscopy in C_2H_2 (around 108.7 nm) and in CO_2 (71.4 - 68.5 nm) has been realized.

With similar setups, other spectroscopic studies followed with improved spectral resolutions of 4.5 GHz (see for example [120, 121]).

The other mentioned possibility is high harmonic generation which also can be realized in any laboratory provided a noble gas (as a medium for the nonlinear frequency conversion) and a laser source that can be focused down to intensities exceeding 10^{13} W/cm² are available. With this technique, harmonics down to 40 nm have been generated with MHz repetition rates. With these systems, mostly direct (two-photon) spectroscopy is motivated or realized (see for example [50, 122–125]) but also direct frequency comb spectroscopy has already been performed (although exclusively pulse pairs are used, see [126, 127]).

These XUV frequency combs could also be used for frequency comb Fourier transform spectroscopy (FC-FTS) as it was already demonstrated in the near and the mid infrared region (see chapters 3.2, 4 and 5). This would bring the benefits of FC-FTS to the XUV range: high resolution XUV spectroscopy would become possible together with high accuracy while simultaneously a broad frequency scale could be recorded within short measurement times (μ s) without any scanning components. Since the customary beamsplitter can be replaced by the wavefront recombination approach, FTS is not limited anymore to wavelength ranges above 140 nm.

A powerful frequency comb source in the UV would not only have a strong impact to Fourier transform spectroscopy but also to high precision spectroscopy, be it either realized via one or two photon transitions. It will also enable the efficient generation of multi-photon entanglement. Further advancements in terms of high peak intensities and short pulse durations will allow attosecond coincidence spectroscopy and the development of an electron gun for femto-/attosecond electron diffraction [128].

All these arguments were decisive to realize an XUV comb source within the framework of this thesis. For a highly efficient frequency conversion, intra-cavity HHG was realized with a frequency-doubled mode-locked laser for the first time to our knowledge. After a quick look into the theory of HHG, the scaling laws that apply to the conversion efficiency will legitimate the innovative approach of enhancing the frequency doubled output of the laser source.

6.2 XUV frequency combs via high harmonic generation

High harmonic generation is a nonlinear process that upconverts the output of highly intense laser radiation into higher frequencies that are located in the XUV or even in the X-ray region depending on the driving wavelengths and intensities. In order to observe this frequency conversion phenomenon, the laser intensities have to be on the order of the atomic binding potential of the medium that is utilized for the process, on the order of 10^{13} W/cm² or higher for noble gases which are generally used.

The following section gives a quick overview about HHG. A more detailed treatment can be found in the respective precursor dissertations of our group [101,129] and in the primary publications (see for example [130,131]).

6.2.1 The perturbative regime: multi-photon ionization

When the laser energy does not exceed the ionization potential I_P of the medium that is irradiated, the atoms can still be ionized by absorbing multiple photons (see figure 6.1 a). The subsequent photon emission can then be attributed to a perturbative motion of the electron wavefunction. The oscillating electric field of the laser radiation causes a modulation of the atomic potential $V(\mathbf{r})$ that changes periodically with the angular laser frequency ω_{mod}

$$V(r) = -\frac{\alpha}{r} + \delta\alpha y \cos[\omega_{mod}t] \quad (6.1)$$

A simulation of a classical particle (electron) in such a perturbed potential was performed in [101] (see chapter 2.2.1, pp. 32 of [101]). In the power spectrum of the modulated potential, odd-order side bands appear that exhibit an exponential decay with increasing order. Hence, in the perturbative regime, odd order harmonics are generated that decrease in power rapidly (see left part in figure 6.2). This behavior occurs at intensities not exceeding 10^{13} W/cm². For higher intensities, the strong laser field starts to significantly deform the atomic binding potential and perturbation theory breaks down.

6.2.2 The non-perturbative regime: the three step model

For larger laser intensities, harmonics of higher order are generated and the shape of the harmonic spectrum features a plateau region that cannot completely be derived from perturbative theory. For these intensities approaching or even exceeding 10^{14} W/cm², the

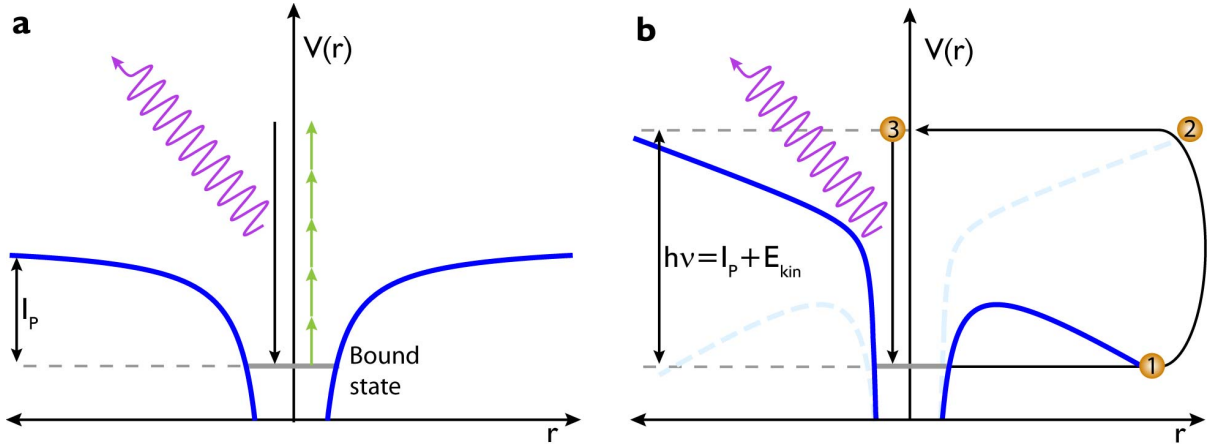


Figure 6.1: XUV radiation can be generated via multi-photon ionization (a) but also via tunnel ionization provided the laser intensity bends the atomic potential strongly enough (b, see following section 6.2.2 explaining the three step model for details).

so-called three-step model introduced by Corkum and Kulander [132, 133] describes high harmonic generation in a simple manner which was afterwards justified also in a quantum mechanical approach by Lewenstein [134]. In the intuitive semi-classical description, the electron first experiences tunnel ionization through the atomic potential into the continuum, because the intense laser radiation strongly deforms the atomic potential (step 1, see figure 6.1 b). Since the electric field changes its sign after half of a laser period (dashed light blue potential curve in figure 6.1 b), the electron that was first accelerated away from the parent ion changes its moving direction and speeds up again towards its parent ion (step 2). This enables a recombination of the electron and the ion by the emission of a high-energy photon that corresponds to the sum of the ionization potential and the additionally attained kinetic energy of the electron (step 3).

The maximum possible kinetic energy of the returning and recombining electrons is found to be $3.17U_P$ with U_P being the ponderomotive energy of the electron (the average kinetic energy of the electron) given by

$$U_P = \frac{e^2 E^2}{4m_e \omega^2} \quad (6.2)$$

with e meaning the electron charge, E the amplitude of the electric field, m_e the electron mass and ω the angular laser frequency. Hence, the highest attainable energy E_{max} is composed by the ionization potential of the electron I_P and the maximum possible average kinetic energy the electrons can have that return to the parent ion:

$$E_{max} = I_P + 3.17U_P = h\nu_{\text{cut-off}} = E_{\text{cut-off}} \quad (6.3)$$

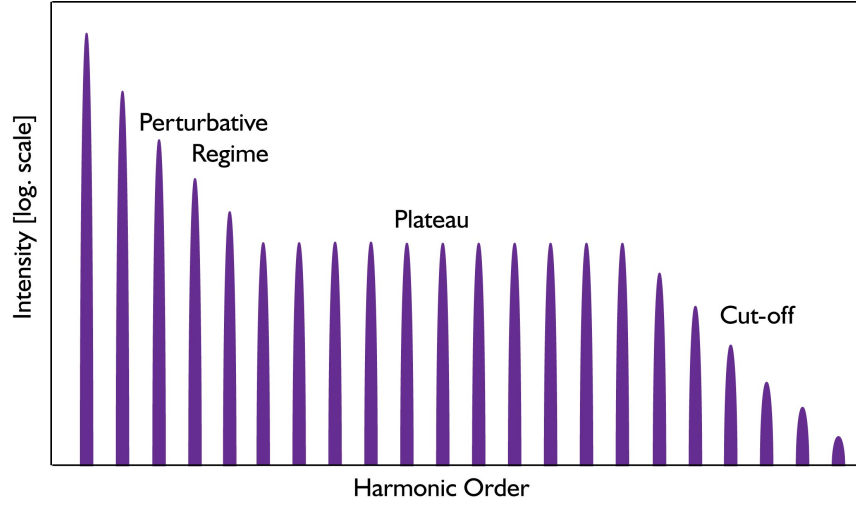


Figure 6.2: High harmonic radiation scheme. Odd order harmonics are generated by an intense laser field in a noble gas cloud, for instance. The harmonic spectrum consists of three different regions: the perturbative regime at low harmonics, a plateau region for intermediate orders and a cutoff region at the highest orders (see text for details).

In the harmonic spectrum, this cut-off energy is clearly visible because it separates the plateau region of the harmonics with equal intensity contributions from the cut-off region where the power of the highest harmonics decrease rapidly again (the cut-off radiation is emitted only by a few electrons that are accelerated by the few most intense half cycles of the laser field, for the shape of the harmonic spectrum, see figure 6.2). Since this whole three-step process occurs every half cycle of the laser frequency and the generated UV radiation of each half cycle interferes with each other, the harmonics are only of odd order: their spacing in time at half the laser period $T/2$ corresponds to a spacing in the frequency spectrum of $2 \cdot \hbar\omega_{laser}$ starting with the fundamental laser energy.

6.2.3 Scaling laws

The recombination event is rather unlikely, and hence, the conversion efficiencies of HHG are low. Indeed, they can vary a lot, between 10^{-5} and 10^{-10} , depending on the applied experimental parameters such as the driving laser frequency and intensity or the phase matching conditions at the gas target [135]. A rather high conversion efficiency of 10^{-5} could be achieved by optimizing the gas pressure in a hollow fiber with an inner diameter of $200 \mu\text{m}$ [136]. This implementation or even more sophisticated realizations of quasi-phase matching [137] could not be realized up to now in enhancement cavities (because of the

associated high losses) but only in single pass systems. On the other hand, spatial filtering in the cavity provides an improved beam quality compared to amplified systems which has a positive impact on the conversion efficiency.

Since an optimized UV output is invariably desired, several publications deal with scaling laws in order to find the parameters that are most profitable to get a high conversion efficiency. One of these scaling laws was published by Balcou et al. [138] stating that the number of generated photons in the plateau region scales with

$$n_{ph} \propto \begin{cases} b^3 \tau, & \text{if } L_{gas} > L_{coh}^{foc} \\ b\tau, & \text{if } L_{gas} < L_{coh}^{foc} \end{cases} \quad (6.4)$$

with $b = \frac{2\pi w_0^2}{\lambda}$ being the confocal parameter of the fundamental laser beam, τ the (intra cavity) pulse length, L_{gas} the length in the medium and $L_{coh}^{foc} = \frac{b}{2} \tan\left(\frac{\pi}{q-1}\right)$ the focal coherence length of the q^{th} harmonic, respectively (see [138] and the reference [139] in there for a more detailed explanation).

Assuming optimum¹ and, hence, equal on-axis peak intensities $I_{peak} = \frac{2}{\pi w_0^2} \cdot \frac{P_{IC}}{f_{rep}\tau}$ for the experiments to be compared (P_{IC} is the intra-cavity power and w_0 the focal radius), the scaling of the generated XUV power can be written with equation 6.4 as

$$P_{XUV} \propto n_{ph} \cdot f_{rep} \propto \begin{cases} \frac{P_{IC}^3}{f_{rep}^2 \tau^2}, & \text{if } L_{gas} > L_{coh}^{foc} \\ P_{IC}, & \text{if } L_{gas} < L_{coh}^{foc} \end{cases}. \quad (6.5)$$

How well this scaling law applies can be tested by comparing relevant publications whose experimental parameters are summarized in table 6.1. For the comparison of [122] with [50], $L_{gas} > L_{coh}^{foc}$ applies and the prediction for the power of the 9th harmonic in [50] would be

$$\left(\frac{100 \text{ W}}{38 \text{ W}}\right)^3 \cdot \left(\frac{10.8 \text{ MHz}}{114 \text{ MHz}}\right)^{-2} \cdot \left(\frac{57 \text{ fs}}{28 \text{ fs}}\right)^{-2} \cdot 820 \text{ pW} = 402 \text{ nW}.$$

This fits quite well with the reported 540 nW. In order to get from the experimental results of [50] to an estimate for [140], one has to consider the second case of equation 6.5:

$$\frac{750 \text{ W}}{100 \text{ W}} \cdot 540 \text{ nW} = 4.05 \text{ } \mu\text{W}$$

The published value of 63.3 μW exceeds the calculated one which can be explained by the strong peak intensity dependence of the XUV output that has not been considered in this

¹The intensity has to reach a certain value in order to generate harmonics. On the other hand, an overvalued intensity would ionize the gas atoms and the electrons would get lost for recombination according to the three step model.

Experiment	Gohle et al. [122]	Ozawa et al. [50]	Jones et al. [140]	Ruehl et al. [125]
$\lambda_{driving}$ [nm]	800	800	800	1070
P_{IC} [W]	38	100	750	5000
f_{rep} [MHz]	114	10.8	50	154
τ [fs]	28	57	>80	>120
ω_0 [μm]	5.3	13	15	17.5
I_{peak} [W/cm^2]	$5 \cdot 10^{13}$	$5 \cdot 10^{13}$	$6 \cdot 10^{13}$	$4.5 \cdot 10^{13}$
b [μm]	220	1300	1770	1800
L_{coh}^{foc} [μm]	45	269	366	38
L_{gas} [μm]	50	400	100	80
P_{9th}^{out} [nW]	0.82	540	63300	3700
η_{9th}	$2.6 \cdot 10^{-10}$	$6.8 \cdot 10^{-8}$	$8.4 \cdot 10^{-7}$	$7.7 \cdot 10^{-9}$

Table 6.1: A selection of different cavity realizations aiming for XUV frequency combs in the past years and their experimental parameters. (P_{IC} is intra-cavity power, τ intra-cavity pulse duration, I_{peak} the on-axis peak intensity, b the confocal parameter of the fundamental beam, ω_0 focus radius, L_{coh}^{foc} focal coherence length, L_{gas} interaction length, P_{9th}^{out} is the outcoupled power of the 9th harmonic and η_{9th} the conversion efficiency of the 9th harmonic.)

model (see for example [122] for an investigation on the intensity dependence of the XUV output). Nevertheless for equal intensities, the presented scaling law matches quite well with experimentally achieved data despite the fact that it is a simplified estimation.

In the presented scaling model, a potential wavelength dependence has not been considered. However, already more than fifteen years ago, a significant difference in conversion efficiencies for different driving laser wavelengths was reported (see for instance [141]). High harmonics were generated with an intense Nd:glass laser system achieving a conversion efficiency on the order of 10^{-10} . The same experiment was performed with the frequency-doubled laser output with comparable experimental parameters (such as peak intensity and focal spot size) and the conversion efficiency outclassed the one achieved with the fundamental laser wavelength by three orders of magnitude.

As can be seen from equations 6.2 and 6.3, the cutoff wavelength reciprocally scales with the square of the driving laser wavelength, λ^{-2} (since $\nu = \frac{\omega}{2\pi} = \frac{c}{\lambda}$). So, for larger driving laser wavelengths, higher harmonic orders are generated. If higher powers at the lower and intermediate harmonics are preferred, short driving laser wavelengths are favored. Recent

publications show that the conversion efficiency η in the plateau region scales with λ^{-6} and the efficiencies in the cut-off region scale with λ^{-5} [142]. The last column in table 6.1 shows a latest publication based on an Yb based cavity running at 1070 nm [125] that can be used for testing the applicability of this scaling law:

$$\left(\frac{1070 \text{ nm}}{800 \text{ nm}}\right)^6 \cdot \eta = \left(\frac{1070 \text{ nm}}{800 \text{ nm}}\right)^6 \cdot 7.7 \cdot 10^{-9} = 4.4 \cdot 10^{-8}$$

This matches quite well with the conversion efficiency of [50]. However, since this law does not account for any experimental parameter but the wavelength, only setups with absolutely equal parameters can be compared with it. A theoretical example probably substantiates better the possible benefit of the wavelength dependence: an intensity of $2 \cdot 10^{13} \text{ W/cm}^2$ at a driving wavelength of 1040 nm can reach a cut-off wavelength of $\approx 67 \text{ nm}$. With the same peak intensity, the frequency doubled source would reach only a cutoff wavelength of 90 nm but would be 64 times more efficient in the plateau region and 32 times more efficient in the cutoff region according to the wavelength scaling law. Since second harmonic generation is rather efficient ($> 50 \%$), it is preferable to use a frequency-doubled system rather than a laser with longer wavelengths for the harmonic generation in order to reach satisfactory power levels especially for the lower and intermediate orders up to the cut-off. That is why a frequency-doubled Yb laser and amplifier system is used for the XUV frequency comb source in this thesis. To our knowledge, this system is the first XUV source generated from green laser radiation with high repetition rates on a MHz scale in an enhancement cavity.

6.3 Experimental setup

The initial laser source for the XUV generation is a mode-locked Ytterbium fiber laser (model *Orange* by *Menlosystems*, emitting at 1040 nm with a repetition rate of 128 MHz) that was already introduced in detail in subchapter 4.2.1. Its laser pulses are stretched, amplified to roughly 12 W and compressed to about 130 fs pulses (see figure 6.3). Since this amplifying segment of the experimental setup was already part of the cavity enhanced Fourier transform spectroscopy, the reader is referred to the according section for details (see subchapter 4.2.2). The amplified output is frequency doubled in a non-linear crystal and injected into the enhancement cavity. The geometry of the cavity provides a tight focus that enables high intensities on the order of 10^{13} W/cm^2 which in turn permit harmonic generation if a gas jet is launched into the focus area. The resulting VUV and XUV

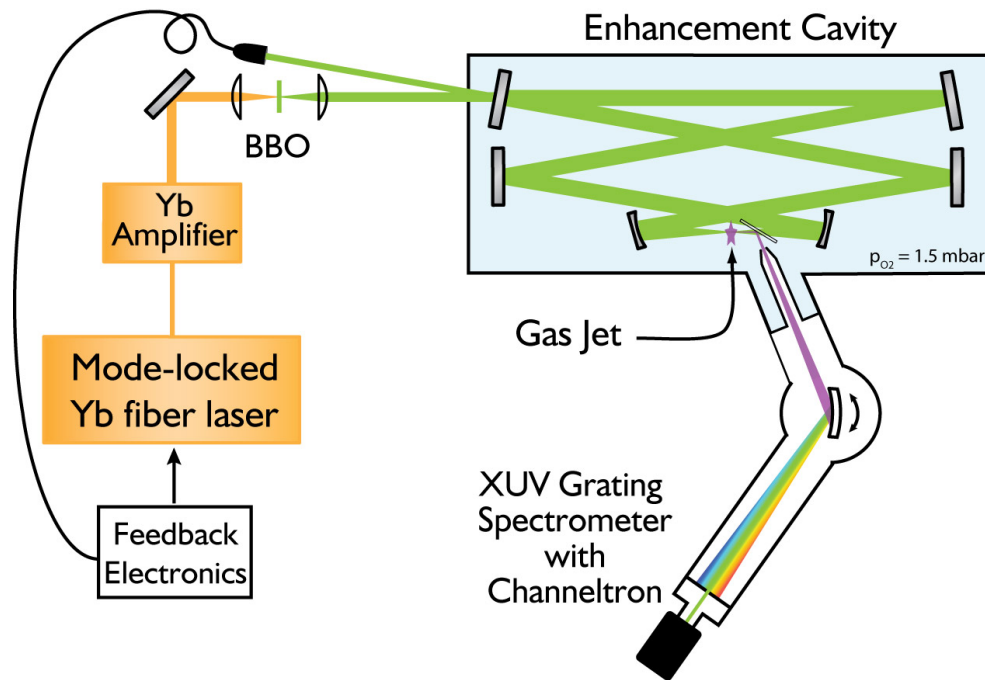


Figure 6.3: Experimental setup for the frequency comb generation in the VUV and XUV. A mode-locked Yb fiber laser is amplified, frequency-doubled and injected into an enhancement cavity. The geometry of the cavity allows a focal intensity on the order of 10^{13} W/cm^2 which is required for the non-linear process of harmonic generation. The resulting XUV light is separated from the fundamental (green) light by using a fused silica Brewster plate. The XUV output is analyzed with a XUV monochromator in combination with a channeltron detector. The oxygen pressure of 1.5 mbar in the cavity chamber is required to prevent mirror degradation (see subchapter 6.3.2 for details).

light has to be extracted from the cavity which is done by using a thin plate oriented at Brewster's angle for the fundamental (green) light circulating in the cavity. Thus, the major part of the green light is transmitted by the Brewster plate while a proper part of the XUV radiation is reflected and coupled out of the cavity enabling the exploitation of the generated light. The VUV and XUV light extracted from the cavity is finally analyzed with a XUV monochromator and a channeltron detector.

The following subchapters provide more details on all important components such as the frequency doubling stage, the enhancement cavity itself, including the gas jet and the Brewster plate, and the detection apparatus for the XUV characterization.

6.3.1 Second harmonic generation

As already pointed out in subchapter 6.2.3, a laser source with a shorter wavelength looks very appealing since it promises higher efficiencies of the high harmonic generation than with a longer driving wavelength. Hence, a frequency-doubling stage has been implemented into the setup so that, to our knowledge, intra-cavity high harmonic generation could be realized for the first time with a frequency doubled light source and hence with such short wavelengths.

The compressed output of the Yb amplifier is focused via an achromatic lens ($f = 75$ mm) into a non-linear crystal (LBO, 1 mm thickness) for second harmonic generation. The green output is recollimated with a second achromatic lens ($f = 75$ mm). The achieved green output power and the corresponding conversion efficiency with growing infrared amplifier output power is depicted in figure 6.4. Various crystal materials with different thicknesses have been tested (PPKTP, BBO, LBO, with thicknesses ranging between 0.5 and 5 mm) with different lens configurations ($f = 20$ -75 mm). The 1 mm thick LBO crystal (from *CASIX*, anti-reflexion-coated for 1040 nm and 520 nm) performed best in terms of high conversion efficiency, minimum beam walkoff and longtime damage resistance. While the PPKTP crystals could not resist the high infrared power of the amplifier because of their too low damage threshold, the beam profile after the BBO crystals appeared elliptical due to the larger walkoff. Figure 6.5 shows the frequency-doubled spectrum and the applying autocorrelation trace that was achieved with the LBO crystal. The thickness of the crystal was chosen to be a good compromise between good conversion efficiency (of about 47 %) and reasonable acceptance bandwidth (The full width at half maximum FWHM = 6 nm or 6.7 THz). 4 W of green power could typically be maintained directly in front of the cavity in a stable and long-term operation of one day with a pulse duration of about 95 fs.

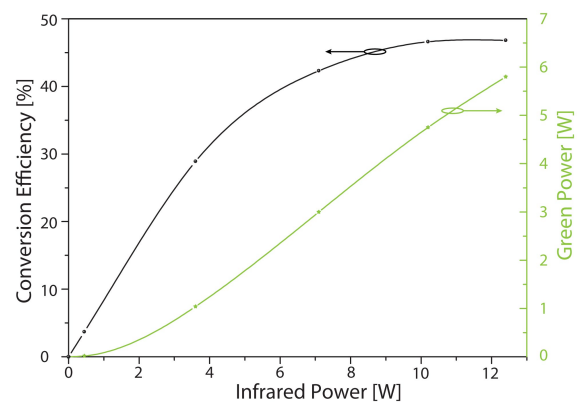


Figure 6.4: The measured green output and the corresponding conversion efficiency with increasing infrared amplifier output.

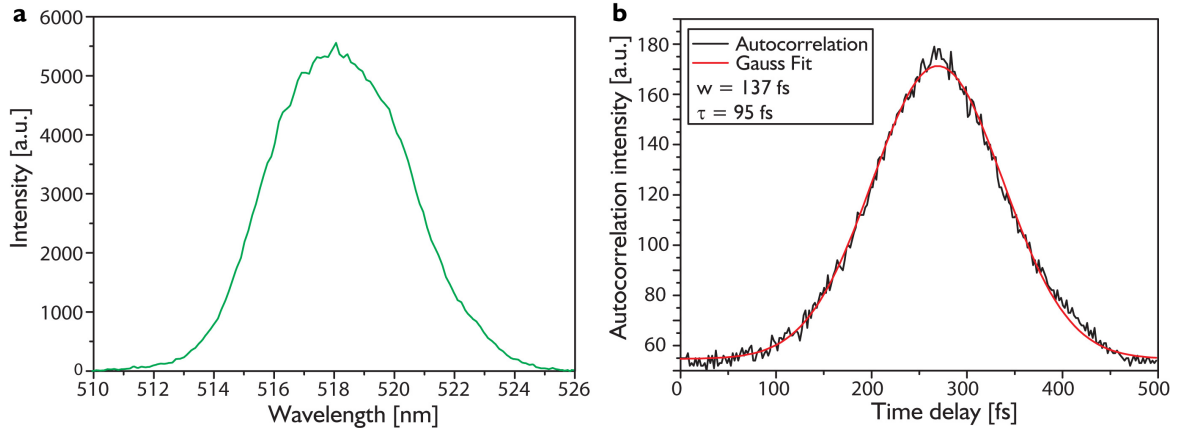


Figure 6.5: Green Spectrum providing an average power of 4 W (a) and the corresponding autocorrelation trace (b) behind the LBO crystal. The spectral shape and the pulse duration appeared to be independent of infrared input power.

6.3.2 The green enhancement cavity

The frequency-doubled light is injected into the enhancement cavity after passing a mode-matching lens ($f = 500$ mm) and three dichroic mirrors in order to filter out the residual fundamental infrared light. The mode-matching lens and the recollimating lens behind the non-linear crystal convert the beam parameters into the ones of the cavity mode (beam waist between the two focusing mirrors (with radius of curvature $r = 25$ mm each) $w_{0,1} = 6.3 \mu\text{m}$, beam waist in the collimated cavity arm $w_{0,2} = 900 \mu\text{m}$).

Similar to the cavity presented in chapter 4, a ring resonator is formed by an input coupler, three plane high-reflector mirrors and two convex high-reflecting mirrors (all mirrors are custom-made by *Advanced Thin Films*). All highly reflecting mirrors were designed to have a reflectivity of $R \approx 99.998$ % between 490 and 550 nm. Impedance matching was achieved best with an input coupler having a transmission of $T = 0.5$ %. Three input couplers with different transmission values (0.05 %, 0.14 % and 0.5 %, respectively) were available and have been tested for the best coupling efficiency (2.7 %, 30 % and 49 %, respectively). The good coupling with the highest transmittive input coupler indicates that the highly reflecting mirrors must have higher losses and, hence, lower reflectivities than specified, about $R \approx 99.90$ % for the relevant wavelength region between 510 and 526 nm. Principally, a slightly lower reflectivity of the green cavity mirrors in comparison to the infrared cavity mirrors was suspected since irregularities in the layer thicknesses of the dielectric coating become more crucial for shorter wavelengths. A transmission measure-

ment of the cavity mirrors confirmed a higher transmission than the specification would allow ($T \approx 0.01\%$ instead of $T \approx 0.002\%$, see appendix B). Further losses can be explained by absorption and light scattering from the imperfect mirror surfaces.

With the presented mirror configuration involving an impedance matched input coupler with a transmission of 0.5 %, one expects a cavity finesse of $\mathcal{F} \approx 630$ and a power enhancement factor of $Q_{IM} = 200$ (see equations 2.22 and 2.21, respectively).

Mirror behavior at high powers

At low input powers of ≈ 250 mW (injected into the cavity), the theoretical enhancement of 200 could be realized also experimentally (see figure 6.6 a). However, with increasing input power, the power enhancement drops. This results in a saturating slope of the intra-cavity power. It was verified that the coupling to the cavity did not change during the measurements by monitoring the coupling ratio via the cavity reflection signal that was mainly used for the Pound-Drever-Hall stabilization of the cavity to the laser (see chapter 4.2.3). A reproducible change in the intra-cavity spectrum with high and low input powers could

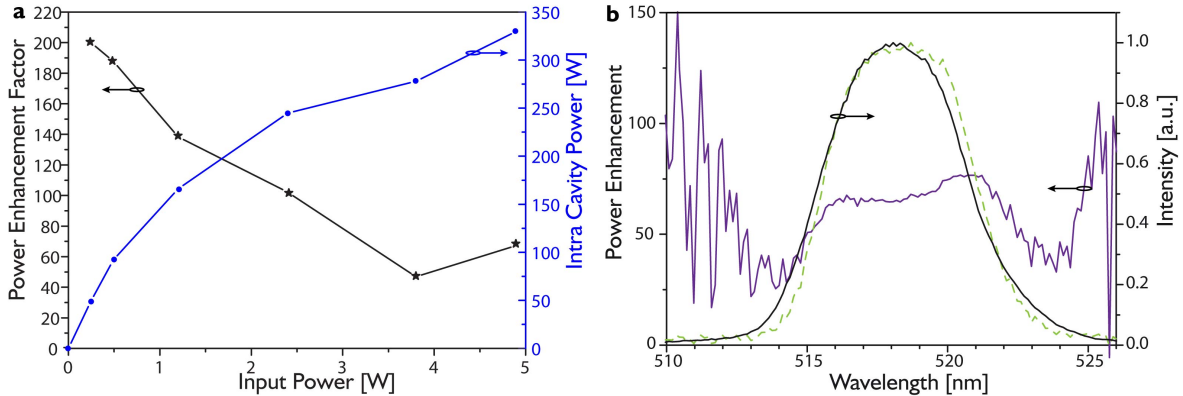


Figure 6.6: **a** The power enhancement factor and the resulting intra-cavity power in dependence of the incident power. The enhancement decreases with growing input power which leads to a saturation of the intra-cavity power. A constant air pressure of 10 mbar was set during the measurement. **b** The laser spectrum at an output power of 4.6 W (black) and the corresponding intra-cavity power (dashed green): the empty cavity (without Brewster plate or gas jet) is low-dispersive and enhances almost the full laser spectrum. The resulting power enhancement is also depicted in violet, spectrally resolved. The power enhancement factor averages to 60 in the presented measurement (air pressure $p = 1.5$ mbar).

not be confirmed. Stretched pulses achieved a higher enhancement indicating a nonlinear effect on the cavity mirrors to be the reason for the power enhancement decrease (115 fs short pulses were enhanced by a factor of 114, 340 fs long pulses reached a power enhancement of 145 with the same input power of 2.4 W). However, since high peak intensities are essential for the nonlinear process of high harmonic generation, chirping the pulses was not an option. Although the power enhancement decreases with the input power, a maximum average intra-cavity power of 330 W could still be reached with an input power of 5 W. This corresponds to a peak intensity of more than $2.5 \cdot 10^{13}$ W/cm² at the focus for the empty cavity. For the case of a long term operation of the setup during a full day, the typical power in front of the cavity could be maintained at 4 W. The corresponding intra cavity power of 280 W provided peak intensities larger than $2.1 \cdot 10^{13}$ W/cm² at the focus. For the data collection in figure 6.6 a, an air pressure of about 10 mbar was set (an undervalued pressure would cause mirror degradation, see following subsection for details). Figure 6.6 b shows the intra-cavity spectrum of the empty enhancement resonator in comparison to the laser spectrum at an output power of 4.6 W (however, a small background pressure of oxygen of 1.5 mbar in the cavity chamber was necessary for degradation prevention, see following subsection for details). The empty cavity without Brewster plate or gas jet features low dispersion over the full laser bandwidth and therefore enhances almost the full laser spectrum. The corresponding spectrally resolved enhancement factor is also depicted in 6.6 b and averages to a power enhancement factor of 60.

Mirror behavior in vacuum

Besides the generally reduced quality in reflectivity and the saturation occurring at high powers, a third mirror effect has been observed: the combination of high intra-cavity powers with vacuum pressures smaller than 1 mbar affects the cavity finesse within a few seconds causing a form of degradation to the cavity mirrors' reflectivity. This is a commonly known phenomenon in the UV community (see for example [143, 144]) but has been observed in the visible wavelength range for the first time to our knowledge. In the UV range, carbon contaminations are the most common explanation for the deterioration of the reflectivity. The highly intense laser field is able to crack residual carbon compounds that are left over in the vacuum which deposit onto the mirror surfaces, thereby shrinking their reflectivity. An established technique to restore the mirror surfaces is a treatment with oxygen. For pressures < 1 mbar, the intra cavity power tended to degrade exponentially with time at the same intra-cavity power independent of the pulse duration (40 W for 115 fs short and

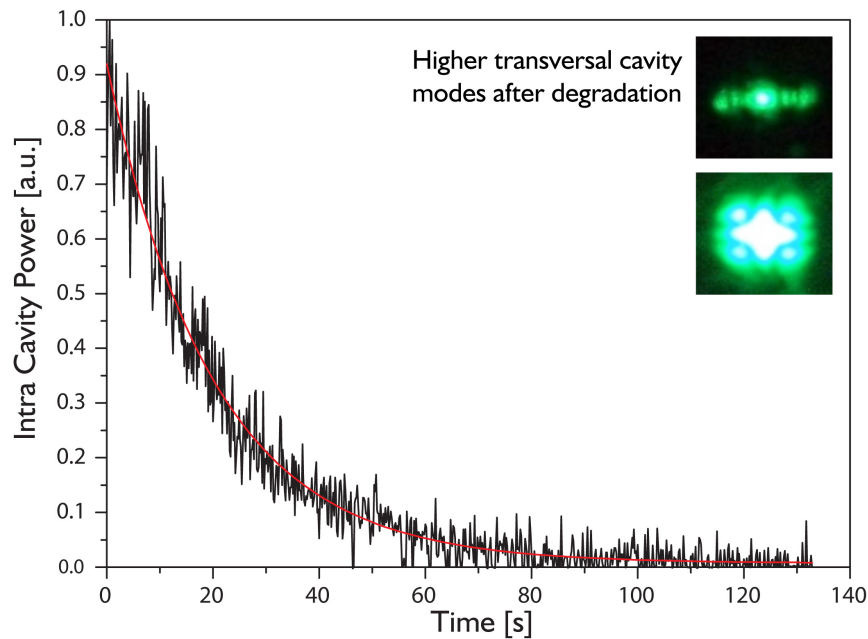


Figure 6.7: Typical degradation behavior of the cavity: as soon as the cavity is locked in vacuum, the cavity starts to degrade exponentially within a few seconds. As a reason, carbon contaminants could stick to the mirrors' surfaces preventing a further locking of the cavity to the fundamental transversal electromagnetic mode TEM00. After the degradation, only locking to higher transversal modes is possible, with lower intra-cavity powers (about 20 % of the original power at most; for typical higher transversal cavity modes after the degradation, see insets in the figure).

340 fs long pulses, see figure 6.7 for the temporal decay). This excludes a peak intensity dependence of the carbon contamination but permits an average intensity dependence like it has been observed in [143]. Oxygen was found to help the mirrors to regenerate again which supports the explanation of the carbon compounds recombining with the oxygen. In fact, a constant amount of oxygen in the cavity chamber prevented the degradation completely. The required oxygen pressure was found to be about 1.5 mbar if the cavity mirror surfaces are flushed with the oxygen close to the point where the laser beam strikes the mirror. This was realized by tubes wrapped by wires for a flexible twist of the tube apertures close to the incidences of the beams on the mirror surfaces.

Another observation in favor of a surface contamination is the beam profile after the degradation: The cavity cannot be locked on the fundamental transversal electromagnetic mode TEM00 anymore but on higher transversal modes (see insets in figure 6.7) which have a different intensity distribution reallocating part of the intensity from the center and

Top mirror coating	P_c [W]	ΔH [kJ/mol]
SiO ₂	39	-911 [145]
HfO ₂	50	-1112 [146]
Ta ₂ O ₅	27	-1970 [147]

Table 6.2: Different top coating materials on the cavity mirrors were tested in their degradation behavior. All mirrors started to degrade at different power levels P_c which have no correlation to the actual dissociation energies ΔH . The values of the critical intra-cavity powers P_c where the degradation starts are reproducible making the explanation of the oxygen dissociation unlikely (see text for details).

hence from the area of the largest contamination to the lateral areas. In addition, the surfaces of the degraded mirrors even appear dirtier to the bare eye and also seem to cause an increased light scattering.

Besides the carbon contaminants, there also has been a second potential explanation of the mirror degradation: the oxygen compounds in the mirror top coating (SiO₂) can dissociate which could also result in a reduction of the reflectivity. Flooding the chamber with oxygen can reverse the dissociation and hence regenerate the mirrors' reflectivity again.

If this is true, the effect should occur at different intra-cavity powers for different materials as the top coating. We were able to try three different material types as the terminal mirror coating: SiO₂, HfO₂ (Hafniumdioxide²) and Ta₂O₅ (Tantalum pentoxide³). Table 6.2 compiles the intra-cavity power that were found to be the critical point the degradation sets in. The dissociation energy of the coatings are also listed. This direction has not further been investigated since there seems to be no correlation between the two parameters.

The carbon contamination theory which has been presented first seems to be the applicable reason for the mirror degradation. For a definite solution, further efforts in the development of mirror design and technology have to be taken. At the current point, the oxygen background pressure of 1.5 mbar is the most convenient solution to prevent the degradation.

²This top layer of a thickness of 50 nm has been coated afterwards on a complete cavity mirror set of the purchased mirrors by ATF after the degradation was found. Special thanks go to Ramin Lalezari at this point for his helpful cooperation.

³For this set of mirrors, special gratitude goes to Dr. Vladimir Pervak, Ludwig-Maximilians-Universität München, who kindly fabricated the coating exclusively for this experiment.

The UV output coupler

An important part of the cavity that has not yet been dwelled on is the Brewster plate inserted behind the tight focus (see figure 6.8 b). The thin window separates the generated XUV light from the fundamental green beam. The latter one should not be attenuated by the plate in order to avert a decrease in the cavity finesse. This is accomplished by implementing the output coupler at Brewster's angle for the fundamental wavelength. The currently used plate is made out of fused silica which has a refractive index of $n = 1.46$ at 518 nm and, hence, a Brewster's angle of

$$\theta_B = \arctan 1.46 = 55.6^\circ. \quad (6.6)$$

In order to get to the resulting reflectivities of the Brewster plate for the generated UV light, the following Fresnel equation of the reflectivity of p-polarized light has to be calculated:

$$R(\lambda) = \left| \frac{n_2(\lambda) \cos \alpha(\lambda) - n_1(\lambda) \cos \beta(\lambda)}{n_2(\lambda) \cos \alpha(\lambda) + n_1(\lambda) \cos \beta(\lambda)} \right|^2 \quad (6.7)$$

α is the angle of incidence in the surrounding medium n_1 (here, $n_1 \approx 1$ for an oxygen pressure of 1 mbar inside the cavity chamber, see section 6.3.2 for details), β is the angle of refraction in medium n_2 (here, the fused silica (FS) Brewster plate). The angle of incidence α is the Brewster's angle θ_B and hence constant but the complex index of refraction $n_{FS}(\lambda)$ and the angle of refraction $\beta(\lambda)$ are wavelength dependent:

$$\begin{aligned} R_{\theta_B}(\lambda) &= \left| \frac{n_{FS}(\lambda) \cos \theta_B - \cos \beta(\lambda)}{n_{FS}(\lambda) \cos \theta_B + \cos \beta(\lambda)} \right|^2 \\ &= \left| \frac{n_{FS}(\lambda) \cos \theta_B - \sqrt{1 - \left(\frac{\sin \theta_B}{n_{FS}(\lambda)}\right)^2}}{n_{FS}(\lambda) \cos \theta_B + \sqrt{1 - \left(\frac{\sin \theta_B}{n_{FS}(\lambda)}\right)^2}} \right|^2 \end{aligned} \quad (6.8)$$

$\beta(\lambda)$ could be substituted via the Snell's law $\frac{\sin \alpha}{\sin \beta} = \frac{n_2}{n_1}$ (here it becomes to: $\frac{\sin \theta_B}{\sin \beta} = n_{FS}(\lambda)$) and the trigonometric function $\cos(\arcsin x) = \sqrt{1 - x^2}$. The resulting reflectivity curve of the fused silica Brewster plate for ultra violet wavelengths is shown in figure 6.8 a. The values for the complex refractive index were taken from [148].

While sapphire (Al_2O_3) has successfully been used in several cavities ($R_{104nm} \approx 6.5\%^4$,

⁴In order to compare the different output coupler materials, the reflectivity at the 5th harmonic is always stated. The single values for the different materials are calculated via the formulas 6.6 and 6.8 with the particular refractive index values from [148].

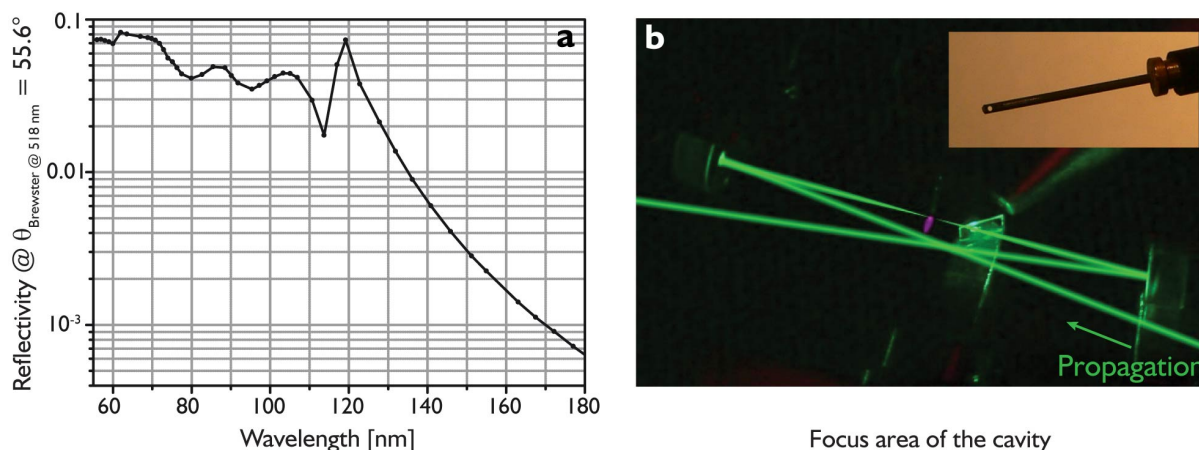


Figure 6.8: XUV reflectivity of the Fused Silica plate (a) at the Brewster's angle of 55.6° for the green fundamental beam. The data of the complex refractive index is taken from [148]. Part b shows the implementation of the Brewster plate behind the focus (the violet plasma is visible in the focus with the Xe gas jet turned on). The inset in b depicts the subsequent nozzle that facilitates the alignment and increases the interaction of the laser beam with the gas.

see for example [50,122]), it introduced too high losses to the green cavity ($> 0.5\%$). This can be explained by the higher sensitivity of short wavelengths to surfaces roughnesses.

Furthermore, different types of thin silicon nitride (Si_3N_4) membranes (thicknesses 50-200 nm, manufactured by *SPI*, *Noricada* and *Silson*) have been tested as XUV output couplers. This material looks very promising since it provides an attractive reflectivity for the UV range ($R_{104\text{nm}} \approx 13\%$) and its thinness adds almost no dispersion to the cavity. The introduced losses of $< 0.1\%$ enabled an enhancement of > 100 but the thin membranes turned out to be very sensitive: a maximum intra-cavity power of only 6 W could be reached before the membranes were destroyed.

Fused silica proved to be a more robust and more applicable candidate ($R_{104\text{nm}} \approx 4.5\%$). A 100 μm thick plate was tested and showed the best performance both in terms of losses introduced to the cavity and damage resistance. At high powers, the implementation of the Brewster plate did not cause any decrease in the power enhancement factor since the cavity mirrors are the limiting element. The Brewster plate's group delay dispersion introduced to the cavity can be looked up in the appendix B.

The intra-cavity spectrum with implemented Brewster plate is shown in figure 6.9. For comparison, the laser spectrum that is injected into the cavity is also depicted as the black curve. The difference of the two curves is due to the cavity dispersion which mostly arises

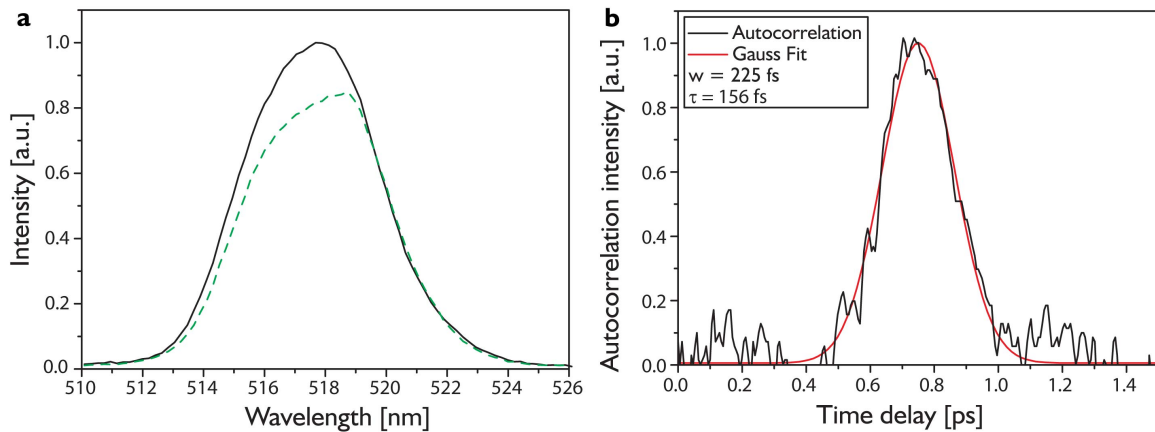


Figure 6.9: **a** shows the intra-cavity spectrum (dashed green) with the Brewster plate implemented in comparison to the laser spectrum that is coupled into the cavity (black). **b** depicts the corresponding intra-cavity autocorrelation revealing a pulse duration of 156 fs inside the cavity.

from the Brewster window (see appendix B). The invariance of the enhancement factor despite the change in the intra cavity spectrum indicate a variation in the spectral coupling to the cavity when the Brewster plate is implemented. For this measurement with Brewster plate, an intra-cavity power of 220 W could be achieved with the injected power of 4 W. This corresponds to a power enhancement factor of 60.

The cavity dispersion also results in a broadening of the pulses to about 156 fs as can be seen in the autocorrelation trace in figure 6.9 b. The autocorrelation of the intra cavity pulses was measured with the pulses that were coupled out by the Brewster's plate. Since the reflectivity is deliberately low for the fundamental light, the signal to noise ratio of the autocorrelation measurement is comparably poor.

With all mentioned parameters, peak intensities of more than $1.7 \cdot 10^{13}$ W/cm² are reached without gas jet.

For the sake of completeness, it shall be mentioned that there also exist alternative techniques for coupling out the generated XUV radiation. They have either already been demonstrated successfully [51, 149] or are currently under first experimental investigation [150, 151].

The Xenon gas jet

Besides the output coupler, figure 6.8 b also shows a violet plasma that is generated at the focus in a Xe gas cloud. The Xe gas is injected via a nozzle whose design has been further optimized after the picture was taken. Similar to the one used in [101], a tube with an inner diameter of 0.4 mm was pierced perpendicularly to its axis with holes of 200 μm diameter (see inset in figure 6.8 b, a photography with this nozzle implemented in the focus of the cavity is not as descriptive since it does not clearly show the generated plasma because it is concealed by the nozzle). By careful alignment of the laser beam through the nozzle holes, a sufficiently good initial overlap between beam and gas is achieved that can be easily optimized by scanning the nozzle along the propagation axis.

An influence of the noble gas jet on the power enhancement has been observed. The higher the gas flow is set, the lower is the power enhancement. This seems to be a nonlinear effect rather than a dispersion effect since the enhancement increases again when the gas jet is scanned out of the focus along the propagation axis with the gas flow held constant. A compromise between high output of the harmonics and high peak intensities in the cavity could be found with a Xe gas flow of 0.4 mbar l/s (value set with the control valve *EVR 116* by *Pfeiffer Vacuum*). The resulting intra-cavity spectrum and pulse length can be

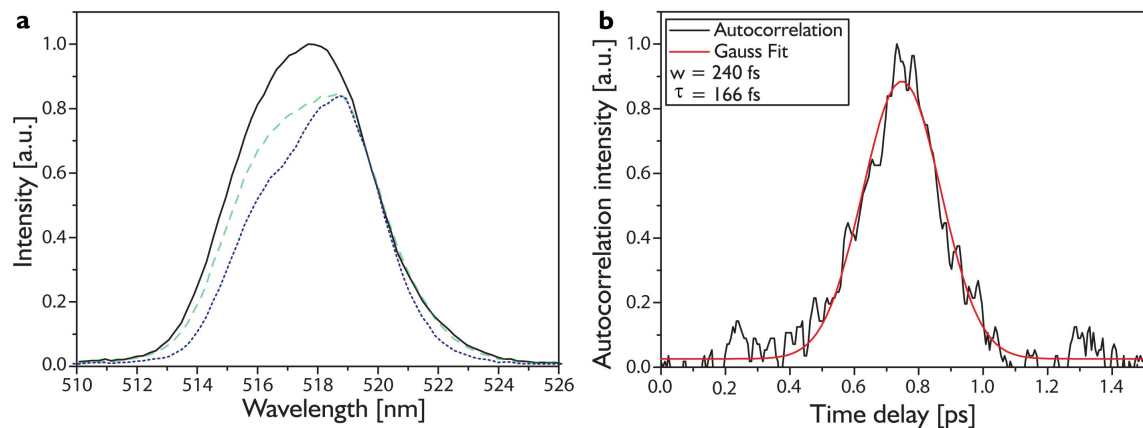


Figure 6.10: **a** shows the intra-cavity spectrum (dotted blue) with both the Brewster plate and the Xenon gas jet implemented (gas flow 0.4 mbar l/s). For comparison, the laser spectrum (black) and the intra-cavity spectrum without Xe gas jet (dashed green curve) are also shown. **b** depicts the corresponding intra-cavity autocorrelation revealing a slightly increased pulse duration of 166 fs inside the cavity.

found in figure 6.10. The spectrum experiences an additional slight reshaping compared to the intra-cavity spectrum with only the Brewster plate installed, and the pulse duration inside the cavity also features an additional small extension. The average intra-cavity power reaches about 190 W corresponding to a power enhancement factor of 50. Hence, with the Xe gas jet, peak intensities of more than $1.5 \cdot 10^{13}$ W/cm² can be reached in the cavity focus.

Stable operation of the cavity

Especially the effect of mirror degradation proved challenging for a stable long-term operation of the experiment (> 45 min). The oxygen pressure of 1.5 mbar required to prevent the degradation leads to a stronger coupling of vibrations and acoustics to the cavity. The increased noise and vibrations impinge on the cavity stabilization: the phase lock is much noisier and unstable and its bandwidth is not high enough to correct all perturbations that are coupled to the cavity. Hence, for a long-time and robust operation, the carrier envelope offset of the laser had to be detuned from the optimum enhancement. The corresponding error signal exhibits a flatter slope than at the optimum position and is consequently easier to control (because of the flatter slope, fluctuations of the cavity length have a smaller amplitude in the error signal and hence a smaller impact to the feedback control). How-

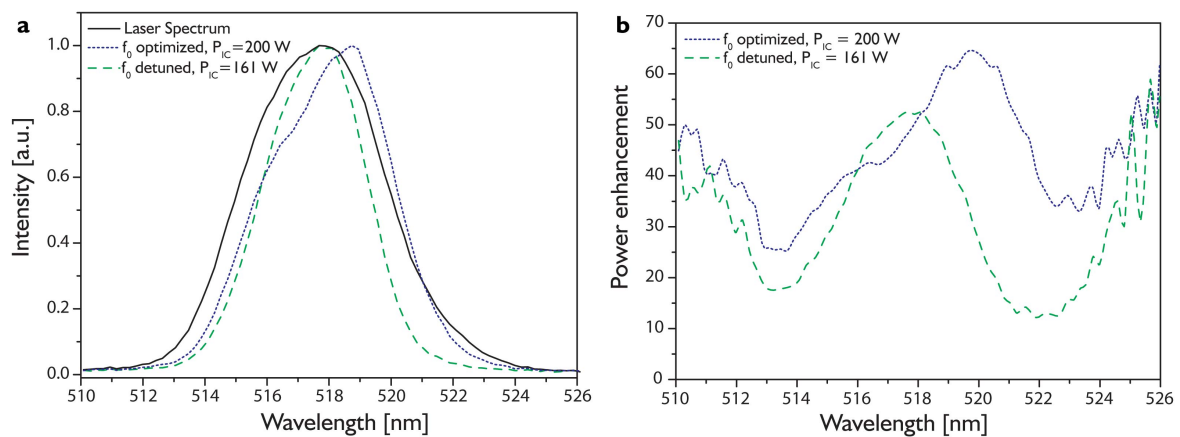


Figure 6.11: For a permanently stable operation, the offset frequency f_0 had to be detuned from the optimum value. The spectrum with optimum offset frequency f_0 (dotted blue), with detuned f_0 (dashed green) and the laser spectrum in figure a are all normalized to 1 for an unweighted spectral comparison. Figure b shows the corresponding spectral enhancements.

ever, this detuning brings along a lower intra-cavity power and hence a lower output of the harmonics. The resulting intra-cavity spectrum with the detuned offset frequency is shown in figure 6.11 a, together with the corresponding spectral enhancement. For long time operation, an average intra-cavity power of 161 W is permanently achieved, corresponding to a power enhancement of 40 and a peak intensity in the focus of more than $1.2 \cdot 10^{13}$ W/cm².

6.3.3 The detection apparatus

The harmonics generated in the Xe gas jet at the cavity focus are spectrally analyzed via an XUV grazing-incidence monochromator (*LHT30* by *Jobin-Yvon*, with an estimated resolution of 1.4 nm) and a channeltron detector (*CEM4839* by *Photonis*). The monochromator together with the attached channeltron had to be implemented into a second vacuum chamber with sufficient differential pumping because the channeltron requires a pressure on the order of 10^{-5} mbar (to suppress background signal of the detector). This pressure could be reached with four turbo pumps (one with pumping speed of 300 l/s and three with 64 l/s, respectively).

Furthermore, the generated harmonics should be coupled to the monochromator chamber with lower vacuum pressure as soon as possible after their production since the O₂ in the cavity chamber absorbs the generated UV⁵. The intersection between the two chambers is designed as a narrow tube where the harmonics are coupled in (see figure 6.12). The orifice of the tube (opening diameter 2 mm) is brought very close to the Brewster plate, so that the produced harmonics pass only a short distance of about 12 mm through the chamber filled with oxygen (see inset in figure 6.12).

For an absolute calibration of the total generated XUV power, the XUV monochromator is removed and the channeltron detector is implemented directly behind the Brewster plate and the tube that separates the two chambers.

The total current I_{ave} that is generated by the detected XUV photons is measured by recording the voltage over a resistor ($R = 1 \text{ M}\Omega$) on a multimeter (*Keithley* model *2001* with GPIB interface). The charge which equates to a single photon detection Q_{1ph} is determined by an averaging measurement over the integrated peaks recorded by a fast oscilloscope (3GHz, model *7300A* with 20 GS/s sampling rate by *LeCroy*). The ratio of these two quantities yields the total number of detected photons $n_{ph}=I_{ave}/Q_{1ph}$ per second

⁵The required oxygen pressure of 1.5 mbar on a path length of 12 mm results in a variable transmission between 30 % and 70 % over the wavelength range between 57 nm and 120 nm (calculated via [152]).

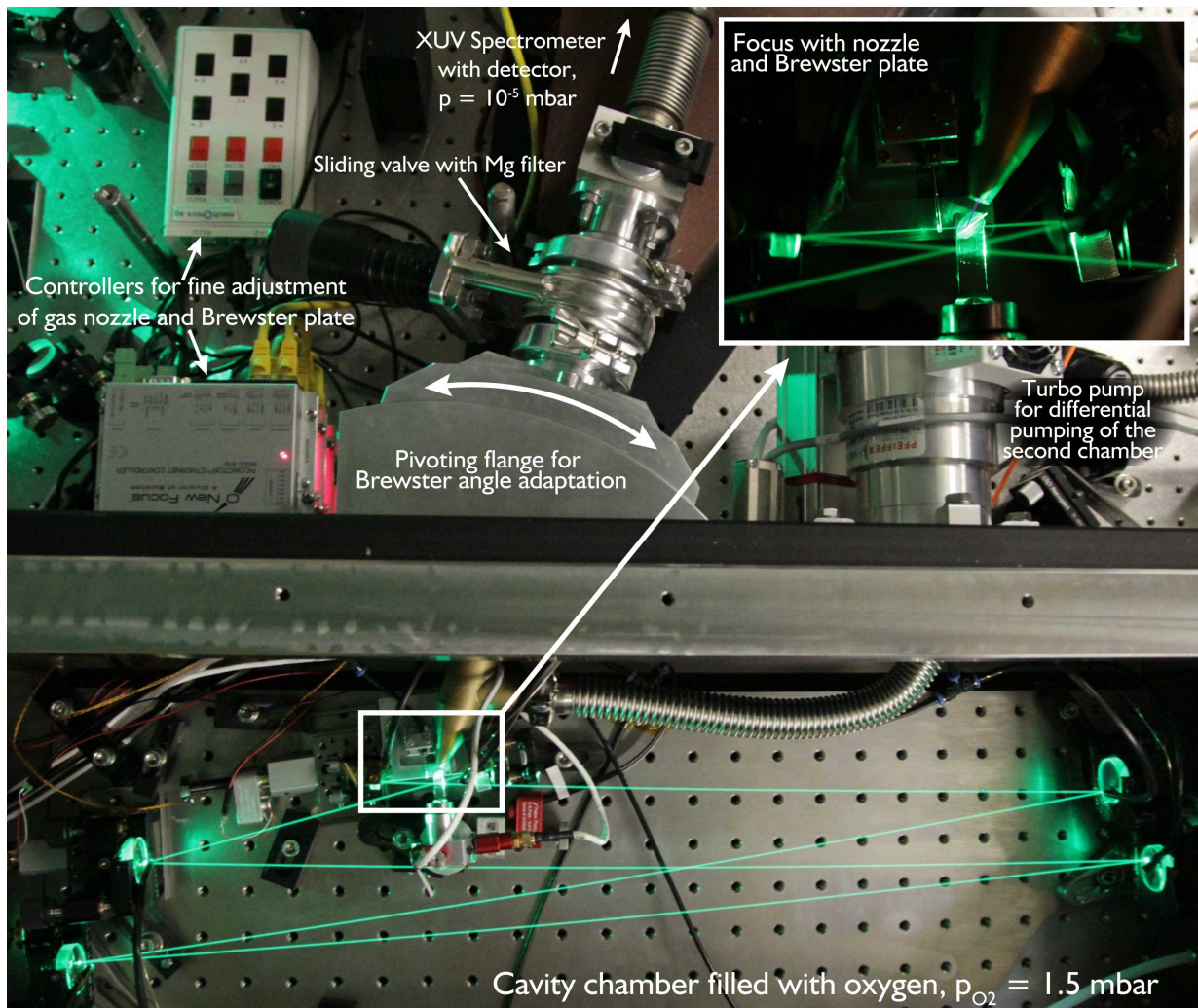


Figure 6.12: The cavity chamber with attached XUV monochromator. The generated harmonics are coupled out of the enhancement cavity by the Brewster plate into a narrow tube that connects the cavity chamber with a second differentially pumped chamber. The end of the tube is attached to a pivoting flange in order to adapt the subsequent monochromator in Brewster's angle (the pivot is seated at the center of the Brewster plate). A sliding valve between the pivoting flange and the XUV monochromator enables the transmission measurement of the Mg filter that is needed for the total power calibration (see text for details). The inset shows the focus area with gas nozzle, Brewster plate and tube tip (brass-colored). The harmonics are sketched in violet for a better understanding.

which may be used to calibrate the spectra taken with the XUV monochromator. For the measurement of the total power, a Mg Filter had to be implemented additionally behind the tube to reach the required pressure of 10^{-5} mbar for the channeltron in this configuration (here, the large turbo pump with 300 l/s is missing because it is directly connected to the XUV monochromator). The transmission of the Mg filter has been experimentally determined with the XUV monochromator and was found to be $2.4 \cdot 10^{-4}$ at 104 nm. This low transmission value is due to the oxide layer always arising on Mg surfaces and the implemented 100 nm thin Parylene-N layer that stabilizes the fragile Mg foil (thickness 300 nm). The measured transmission value is assumed to be constant along the XUV wavelength range (although it can theoretically be even lower for the used filter configuration, see database of the Center of X-ray Optics CXRO [152]) and used for the calibration together with the Brewster plate reflectivity, the transmission through the oxygen and the specified quantum efficiency of the channeltron.

6.4 Results and discussion

6.4.1 The XUV spectrum

With the permanent oxygen pressure of 1.5 mbar, a stable operation of the cavity with a peak intensity of more than $1.2 \cdot 10^{13}$ W/cm² could be achieved at the focus for more than 45 minutes providing an average intra cavity power of 161 W. Within this time period, the offset frequency of the Yb laser drifts and hence had to be readjusted repeatedly via the wedge pair inside the oscillator. Besides of the offset frequency, the Xe gas flow rate, the nozzle position, the feedback loop parameters, the Brewster plate and the oxygen pressure were optimized in order to maximize the XUV signal output. While tweaking all these parameters, a violet plasma is increasingly glowing at the tight cavity focus (see figure 6.8 b).

The XUV spectrum is measured directly behind the monochromator without any filter because the detector is insensitive to the fundamental radiation at 518 nm. Figure 6.13 depicts the number of detected photons after a normalization to the total number of detected photons with Mg filter (see previous section for details).

For the sake of completeness, the third harmonic at 172.7 nm was additionally detected with a photomultiplier (model *R7511* by *Hamamatsu*, green curve in figure 6.13). Here, the number of detected photons is in total smaller than the detected photon number of the

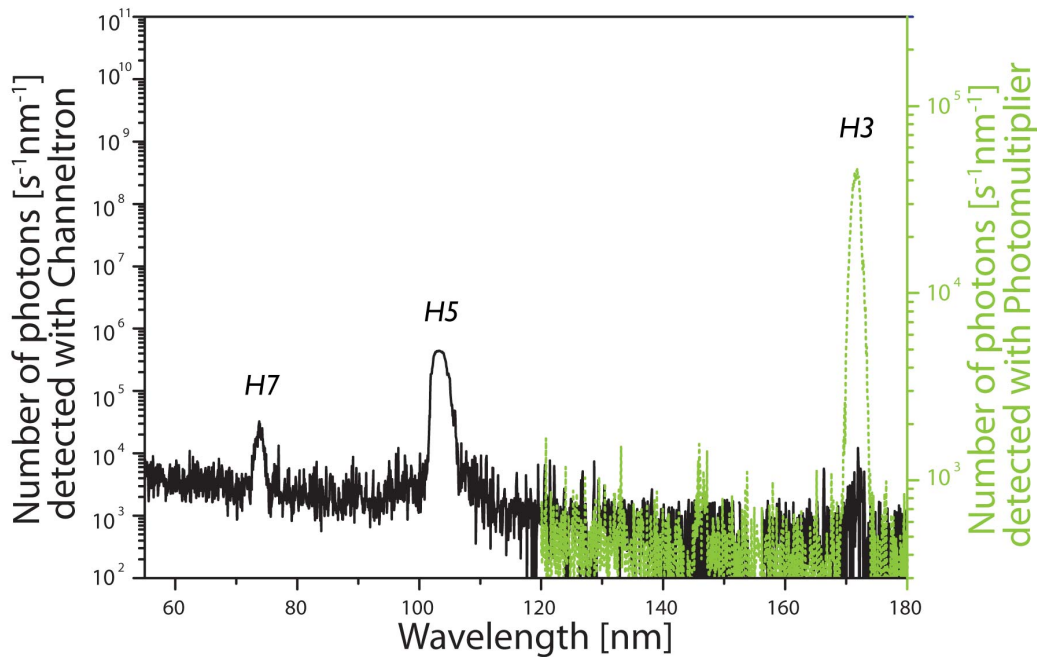


Figure 6.13: Number of detected photons after a total power calibration measurement (see text for details). The third harmonic was detected with a CsI coated photomultiplier (dotted green curve) since the channeltron is not sensitive enough in this region.

5th harmonic because the Brewster plate is much less efficient for this wavelength region (for reflectivity values, compare with figure 6.8 a). For the values of the generated XUV power, the Brewster plate reflectivity (see subsection 6.3.2), the magnesium filter transmission (see subsection 6.3.3), the transmission through the short path in the cavity chamber that is filled with oxygen (see table 6.3) and the quantum efficiency of the detector⁶ have to be taken into account. The result is shown in figure 6.14. Due to the limited accuracy of the total calibration (actual pathlength of the UV in the oxygen chamber and the corresponding theoretical O₂ transmission, Mg filter transmission measurement and grating diffraction efficiency) the absolute power is estimated to be correct within a factor of ≈ 2 . In the XUV spectrum, there is no plateau region observed but a rapid decrease with the order of the harmonics, as in a perturbative regime. This has been observed before with green fundamental light generating high harmonics (see for example [138]). The efficiency

⁶The quantum efficiencies of the channeltron are approximately $1 \cdot 10^{-5}$, $8 \cdot 10^{-2}$, 0.1 and 0.1 for the 3rd, 5th, 7th and 9th harmonic, respectively (see specification plot in the *Channelbook* by *Burle*).

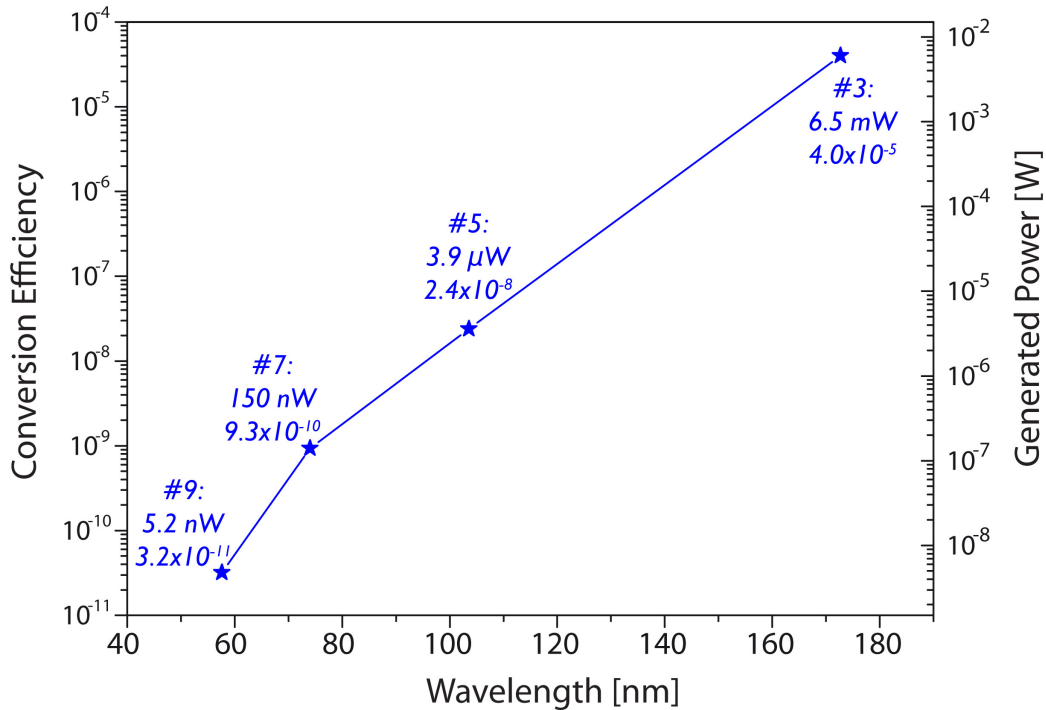


Figure 6.14: The total generated power of the harmonics and the corresponding conversion efficiencies. For the retrospective calculation of the generated powers from the detected signal (see figure 6.13), the reflectivity of the Brewster plate, the transmission through the oxygen chamber, the transmission through the Mg filter and the quantum efficiency of the detector have to be considered.

of the third harmonic of $4.0 \cdot 10^{-5}$ is large for a system without sophisticated phase-matching resulting in a power level of mW at 172.7 nm. Since the achieved intensity of $1.2 \cdot 10^{13}$ W/cm² lies within the perturbative regime, the higher harmonic orders decrease exponentially. However, the conversion efficiencies of the 5th, the 7th and even the 9th with their values of $2.4 \cdot 10^{-8}$, $9.3 \cdot 10^{-10}$ and $3.2 \cdot 10^{-11}$, respectively, are not too far below the most recent publication with Yb based high finesse intra-cavity HHG, although there, average intra-cavity powers of kW were obtained. This is due to the XUV output scaling law that is favorable for short driving wavelengths (see the following conclusion chapter 6.4.2 for a more precise comparison).

The 9th harmonic

In figure 6.14, there is a value given for the 9th harmonic, although there is no corresponding peak in the previously shown XUV spectrum (figure 6.13). For the detection of this

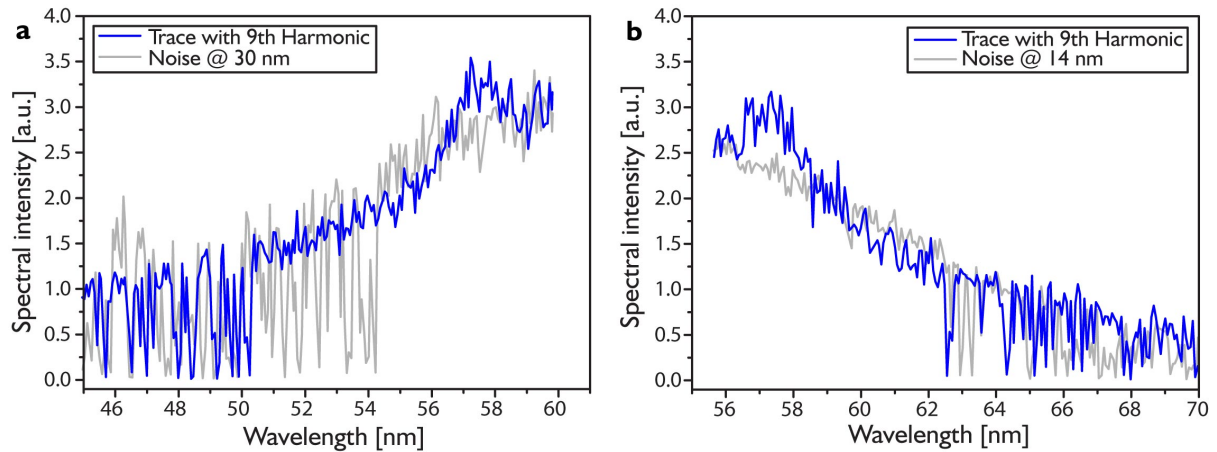


Figure 6.15: For the detection of the weak ninth harmonic, the cavity chamber is evacuated to a pressure $< 10^{-3}$ mbar. The scan over the expected position of the 9th harmonic is started simultaneously when the cavity is locked in order to maintain enough intensity to observe the harmonic. The typical decay due to the degradation is observed in both directions in addition to a clearly visible harmonic peak at 57.7 nm (Decreasing (a) and increasing (b) wavelength scan, respectively). To subtract the back ground noise, the scan is also performed at grating positions where no harmonic is observed (at 30 and 14 nm, respectively, gray lines. They are shifted in wavelength to overlap with the curves with the harmonic signal).

weak harmonic, the cavity has been evacuated to a pressure lower than 10^{-3} mbar and the grating position has been tuned to a point very close to the expected position of the harmonic (60 nm/56 nm for a scan towards lower/higher wavelengths, respectively). The wavelength scan was started on at the same time the cavity has been locked in order to scan over the 9th harmonic before the cavity had time to degrade. This has been repeated several times in both directions. The 9th harmonic could indeed be detected in this manner as can be seen in figure 6.15. In order to subtract the noise floor, a wavelength scan has been performed at points in the spectrum where no harmonic is located (scan starting at the arbitrarily chosen positions of 30 nm and 14 nm, respectively).

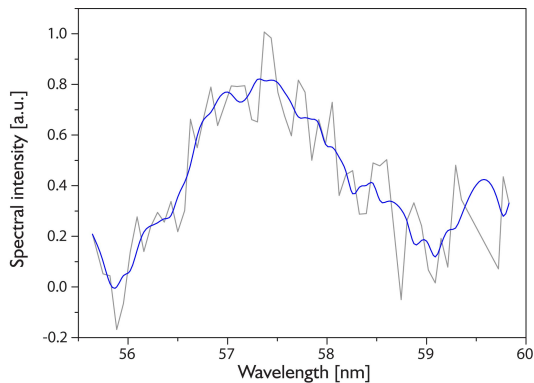


Figure 6.16: Subtracting the noise floor that is shown in figure 6.15 clearly reveals the 9th harmonic. An adjacent averaging over five points (blue) further smoothens the curve.

Figure 6.16 depicts the signal of the ninth harmonic after noise subtraction. For the power calibration, the area below the 9th harmonic was compared to the one of the 7th harmonic in the previously shown XUV spectrum (see figure 6.13). After accounting for the different resistors used for matching the sensitivity of the measurement, the power of the 9th harmonic has been determined to be about 2.5 % of the power of the 7th harmonic order.

The extracted power of the harmonics

Figure 6.14 summarized the generated power levels for each harmonic at the cavity focus. However, due to the oxygen inside the cavity chamber and the partially reflecting Brewster output coupler, only a part of this power is coupled out of the cavity. Table 6.3 outlines the oxygen transmission and the Brewster plate reflectivity for the different harmonics and the resulting power extracted from the cavity. The transmission values for the oxygen were determined by [152], the reflectivity of the Brewster output coupler was calculated via equation 6.8 (see figure 6.8). The outcoupling efficiency of the 3rd harmonic shows the lowest quality currently accounting for a loss of three orders of magnitude to several μW . However, this power level is still comparable with the extracted powers of the state-of-the-art Yb-based cavity system generating harmonics [125].

6.4.2 Conclusion

With the presented experimental system, harmonics up to the ninth order, i.e. down to a wavelength of 57 nm have been generated. The mirrors of the enhancement cavity turned out to be the currently limiting component that only allowed harmonic generation in the perturbative regime (since the peak intensities were $1.2 \cdot 10^{13} \text{ W/cm}^2$). Further develop-

Harmonic order	λ [nm]	P_{gen} [W]	T_{O_2}	R_{FS}	P_{ex} [W]
3rd	172.7	$6.5 \cdot 10^{-3}$	0.55	$8.8 \cdot 10^{-4}$	$3.1 \cdot 10^{-6}$
5th	103.6	$3.9 \cdot 10^{-6}$	0.70	$4.4 \cdot 10^{-2}$	$0.12 \cdot 10^{-6}$
7th	74	$150 \cdot 10^{-9}$	0.58	$5.6 \cdot 10^{-2}$	$5.0 \cdot 10^{-9}$
9th	57.6	$5.2 \cdot 10^{-9}$	0.32	$7.3 \cdot 10^{-2}$	$122 \cdot 10^{-12}$

Table 6.3: Due to the absorption of the oxygen inside the cavity chamber and the non-ideal reflectivity of the Brewster plate, less than 100 % of the generated XUV power is extracted from the cavity. P_{gen} is the generated power of the respective harmonic, T_{O_2} the transmission through the 1.2 cm long path of oxygen (pressure 1.5 mbar), R_{FS} is the reflectivity of the Brewster plate at an angle of incidence of 55.6° (see figure 6.8 a) and P_{ex} the power coupled out of the cavity.

ments on better cavity mirrors in terms of reflectivity and high-power insensitivities (less non-linear effects) could push the achievable intra-cavity powers and thus the intensities much higher entering into the non-perturbative regime. Further investigations towards an optimum focus diameter in the plasma and a more advanced output coupler (reduced in its thickness and UV reflexion coating) could decrease their nonlinear response to the high intensities and the cavity dispersion, thereby increasing the output of the harmonics. As a result of the former two issues, a plateau could be generated and even higher order harmonics could be produced since the cut-off energy increases for higher intensities. We estimate that the plateau of the conversion efficiency will be at least on the level of 10^{-8} since the theoretical single-atom cut-off wavelength for the current experimental parameters is at about 94 nm (see equations 6.2 and 6.3 and compare with the conversion efficiency at 94 nm in figure 6.14) and the output of the q th harmonics scales with intensity as I^q in the perturbative regime (see for example [138]).

Comparing the conversion efficiency achieved with the first green cavity mirror design presented in this thesis, they already overmatch the accordant first generation experiments that introduced the Ti:sapphire and the Yb-laser based systems [51, 122] (see figure 6.17). The experiments of the second or higher generation are in the meantime achieving higher efficiencies due to the development e.g. of more advanced mirror coating designs (dispersion management by chirped mirrors) or of advanced output couplers over the intervening years [50, 125, 140]. A precise comparison of the different experiments running at 518 nm, 800 nm and 1070 nm is very difficult because a variety of experimental parameters are totally different (e.g. driving laser frequency, focus size, confocal parameter, focal intensity, repetition rate, pulse length, phase matching, see table 6.4).

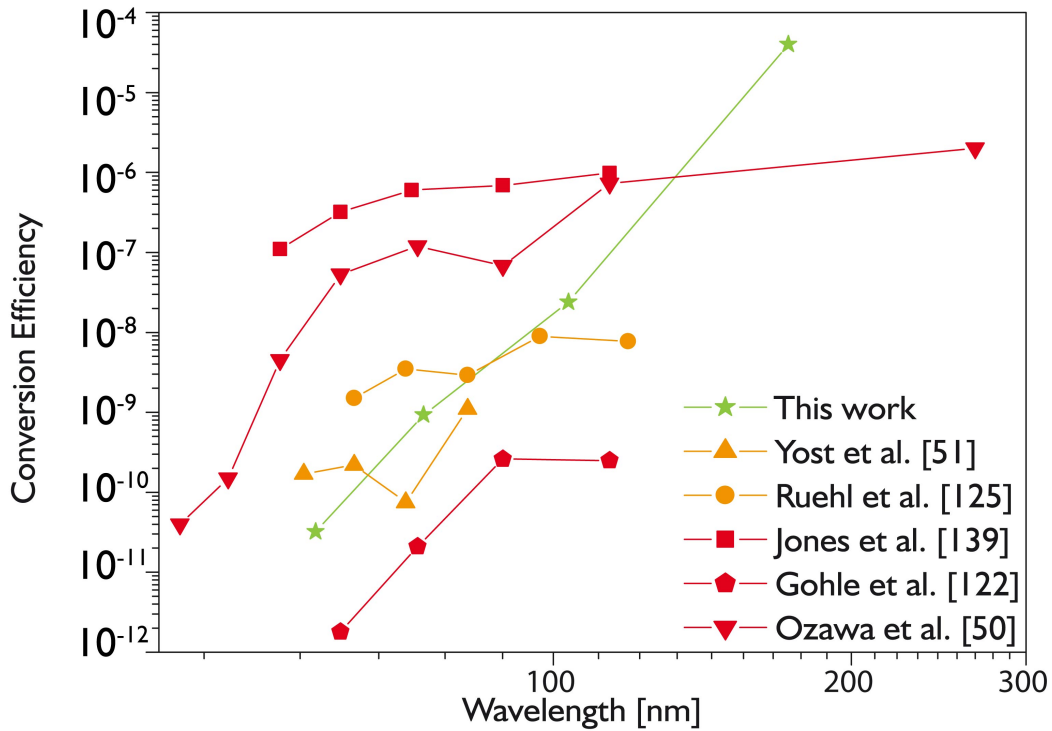


Figure 6.17: Achieved conversion efficiencies of several Ti:sapphire (red), Yb (orange) cavities and the green cavity. The green cavity already exceeds the first realizations based on a Ti:sapphire [122] and a Yb-fiber based system [51]. For a more detailed comparison, see text.

The most recent Ti:sapphire enhancement cavity could stably build up average powers of 750 W and peak intensities of $4.5 \cdot 10^{14}$ W/cm² [140]. With this, unprecedented conversion efficiencies on the order of 10^{-7} could be reached. This setup and another Ti:sapphire based cavity realized in our group [50] are the experiments with the highest conversion efficiencies to date. This can be attributed to the short pulse durations and low repetition rates besides their comparably short driving wavelengths (see equation 6.5).

A recent conference proceeding reports on a Yb-fiber laser based intra-cavity HHG setup [125] that reaches 5 kW with $4.5 \cdot 10^{13}$ W/cm². Since they used a long driving laser wavelength of 1070 nm, the cut-off wavelength is quite low (45 nm) and they observe a broad plateau with a conversion efficiency level of 10^{-9} . However, although several kW of intra-cavity power and almost four times higher peak intensities are achieved, the obtained conversion efficiencies are still comparable with the presented green cavity (repetition rate and pulse duration are of comparable order). This is due to the scaling law that favors

Experiment	Gohle et al. [122]	Ozawa et al. [50]	Yost et al. [51]	Ruehl et al. [125]	Jones et al. [140]	This work
$\lambda_{driving}$ [nm]	800	800	1070	1070	800	520
$\overline{P_{IC}}$ [W]	38	100	2600	5000	750	161
f_{rep} [MHz]	114	10.8	136	154	50	128
$\Delta\tau_{IC}$ [fs]	28	57	100	>120	>80	166
$2\omega_0$ [μm]	10.6	26	35	35	30	12.6
I_{peak} [W/cm^2]	$5 \cdot 10^{13}$	$5 \cdot 10^{13}$	$4 \cdot 10^{13}$	$4.5 \cdot 10^{13}$	$6 \cdot 10^{13}$	$1.2 \cdot 10^{13}$

Table 6.4: The experimental parameters of different cavity realizations aiming for XUV frequency combs in the past years. The conversion efficiencies of the harmonics achieved with these systems are depicted in figure 6.17.

short driving wavelengths (see section 6.2.3).

Hence, a shorter driving wavelength for VUV and XUV generation proved to be more efficient and even promises further improvements by further development of the cavity mirror design or redesign of the cavity with larger beam spot sizes on the cavity mirrors. The intensity dependence of the mirrors caused a decrease of the power enhancement from 200 to 60. Although the gas jet and the Brewster plate slightly reduced the intra-cavity power as well, the cavity mirrors are the crucial components limiting the intensity first of all. With an improved mirror technology and/or larger spot sizes on the mirrors, tripled intensities could become possible ($3.6 \cdot 10^{13} \text{ W}/\text{cm}^2$, an expansion of the focus due to plasma non-linearities could however become necessary, see [140]). Since each individual harmonic follows a power law with an exponent close to the harmonic order [122, 138], this slight improvement could bring a huge benefit.

An additional improvement could be made in the phase locking loop of the cavity stabilization. The current bandwidth is not high enough to stabilize the cavity with optimized carrier envelope offset. In order to increase the speed of the phase lock, an electro optical modulator could be installed inside the Yb oscillator which would increase the bandwidth of the PZT (that is currently limited to several kHz) in the oscillator to a MHz level.

Despite the mentioned limiting issues, already with the achieved results, FC-FTS would be feasible since power levels on the order of μW are sufficient for the new technique. In the range of the now accessible region of 104 and 173 nm, many molecular absorption

spectra such as those of Sulfur Dioxide (SO_2 , [153]), Nitrous Oxide (NO , [154]), Oxygen (O_2 , [155]), Ozone (O_3 , [156] and Acetylene (C_2H_2 , [157]) could be recorded with the new light source being relevant to the photochemistry of planetary atmospheres and astrophysical investigations.

In addition to that, the application field of the new UV light source is not only restricted to Fourier spectroscopy. For instance, also linear absorption spectroscopy could be done on the $3p_{1/2}$ - $4d_{3/2}$ transition in Mg^+ at 173.5 nm. With the experimental parameters that have been already achieved, a signal rate of approximately 1 GHz could be possible [158]. However, due to the oxygen in the cavity chamber and the fused silica Brewster plate, a big portion of the generated UV light is currently lost as could be seen in table 6.3. A small, differentially pumped vacuum chamber around the focus area similar to the one used in [129] would completely avoid the XUV propagation in the absorbing oxygen while the cavity mirrors in the bigger chamber could be undisturbingly flushed with the degradation preventing gas. The reflectivity of the currently used fused silica output coupler decreases quickly for wavelengths above 120 nm (see figure 6.8 a) what results in a three orders of magnitude loss of the generated power in the 3rd harmonic. Due to its high damage threshold, sapphire would be an alternative material that has been successfully used in all mentioned Ti:sapphire systems. However, due to the shorter driving wavelength, the surface roughness is more critical in the presented experiment and plates with a higher surface quality than the hitherto used ones have to be obtained. In addition, MgO as Brewster output coupler features higher reflectivity values in the UV compared to fused silica (MgO partially reflects almost two orders of magnitude better, see equation 6.8 with the index of refraction values in [148]). It has already been successfully implemented in an enhancement cavity with intra-cavity powers exceeding 3 kW, additionally outperforming fused silica in terms of high power damage resistance [159].

The light source realized here already represents a serious alternative to synchrotron sources since the latter ones also emit relative output powers on the μW level per wavelength segments of ≈ 2 nm (see for example [160]). With the current setup, UV radiation is only provided at the discrete odd multiples of the fundamental frequency due to the harmonic generation process. However, a continuum in the UV could be generated by shorter few-cycle pulses with cosine waveform, see for example [161].

Since the presented setup occupies only a small optical table of $1.2 \text{ m} \times 1.8 \text{ m}$ including the analyzing XUV monochromator being the bulkiest component, very compact frequency comb sources come into reach for Fourier transform spectroscopy in the UV. This brings

the high accuracy, high resolution and broad bandwidth that are all simultaneously possible with frequency comb Fourier transform spectroscopy to the rather unexplored and fascinating high-energy region of the VUV and the XUV.

Chapter 7

Summary and outlook

In this doctoral thesis, a variety of experiments around frequency comb Fourier transform spectroscopy has successfully been realized in different wavelength regions.

It has been demonstrated that dual comb spectroscopy has several powerful properties at once which all individually turn the new technique into a helpful tool for molecular spectroscopy. The first experiments outmatched the traditional Fourier transform spectroscopy in terms of *acquisition time* by a factor of one million. *High resolutions* were realized with the new compact setup while a device based on the conventional method has not yet been realized with equal resolution and will ever hardly fit in one laboratory¹. Implementing an enhancement cavity improved the *sensitivity* that much (minimum detectable absorption coefficient α_{min} on the order of 10^{-8} cm^{-1}) that the newly obtained detection levels make dual comb spectroscopy suitable for trace gas detections, although the utilized laser sources are not emitting in the mid infrared, the mainly investigated region because of the strong molecular fingerprints located there. The innovative dual comb spectrometry has nevertheless successfully been realized also in the *MIR region* and has the potential to conquer also the rather uninvestigated ultraviolet range with the already successfully demonstrated *XUV combs*, including the ones developed in this work as well.

To become more precise, the first implementation in our group of dual comb spectroscopy has been realized in this work by employing two erbium frequency combs emitting at 1550 nm. Broad absorption spectra of acetylene have been recorded within only 42 μs

¹The state of the art device has a maximum mirror displacement of 10 m which results in a resolution of 30 MHz [162]. In order to get to the same resolution of 1 MHz that was obtained in chapter 3.2, a mirror displacement of 300 meters would have to be realized with the conventional interferometer.

with a resolution of 12 GHz reaching a noise equivalent absorption coefficient (NEA) of $8 \cdot 10^{-7} \text{ cm}^{-1}\text{Hz}^{-1/2}$ (see section *Real time spectroscopy* in chapter 3.2.3), which means an *improvement in the recording time by a factor of one million* compared to the traditional Fourier transform spectroscopy.

A stabilization of the two erbium combs enabled *high resolutions* of the comb lines of only 2.3 kHz (see section *Extreme resolutions* in chapter 3.2.3). Further exploitation of the controlled stabilization of the offset frequency allowed to increase the sampling step and, hence, the resolution of the molecular transitions from 100 MHz (repetition rate) to only 1 MHz.

The next experiment aimed at the improvement of the detection sensitivity of dual comb spectroscopy. This was realized by an enhancement cavity that increases the path length the laser interrogates in the gas sample. With the ring cavity configuration that enhanced the output of an amplified Yb fiber laser, a power enhancement factor of 385 was achieved which corresponds to an effective absorption path length of more than 900 m. Absorption spectra of acetylene and ammonia have been recorded at the wavelength region around 1040 nm with a resolution of 4.5 GHz. An *enhanced detection sensitivity* could be demonstrated with NEA values of $5 \cdot 10^{-10} \text{ cm}^{-1}\text{Hz}^{-1/2}$ for C_2H_2 and $1 \cdot 10^{-10} \text{ cm}^{-1}\text{Hz}^{-1/2}$ for NH_3 , respectively. This means a 20-fold improved sensitivity with a simultaneously 100-fold shorter measurement time than in the hitherto state-of-the-art experiment (see chapter 4).

Up to this point, the dual comb spectroscopic realizations have only been performed in the near infrared region where only the overtone and, hence, weak rovibrational molecular bands can be found. In order to *transfer the powerful FC-FTS technique to the mid infrared region* where the fundamental and, hence, strong rovibrational transitions are located, an experiment with two $\text{Cr}^{2+}:\text{ZnSe}$ lasers has been carried out. Thanks to these recent femtosecond lasers, acetylene spectra at $2.4 \mu\text{m}$ could have been recorded with an NEA of $9 \cdot 10^{-7} \text{ cm}^{-1}\text{Hz}^{-1/2}$ (see chapter 5).

In order to transfer the innovative dual comb spectroscopy to all wavelength regions of spectroscopic interest, a *VUV/XUV frequency comb source has also been developed* in this thesis. By enhancing the output of an amplified, frequency-doubled Yb-fiber laser in an external cavity, intensities above $1.2 \cdot 10^{13} \text{ W/cm}^2$ were reached which in turn enabled harmonic generation in a gas jet. The frequency-doubling of the laser output should increase the efficiency of the conversion process in the noble gas. Harmonics up to the 9th order down to 57 nm could be generated. The high powers of the 3rd harmonic (@ 173 nm)

of 6.5 mW (relating to a conversion efficiency of 10^{-5}) and of the 5th harmonic (@ 104 nm) of 2.1 μ W (corresponding to a conversion efficiency of 10^{-8}) would already enable dual comb spectroscopy in the vacuum ultra violet with further improvement of the poor outcoupling efficiencies of 0.08 % for the 3rd and 4 % for the 5th harmonic, resulting in 3 μ W and 0.1 μ W of extracted power, respectively. For the implementation of XUV dual comb spectroscopy, the system would have to be duplicated. The generated powers of the 7th and 9th harmonic are weaker due to the ponderomotive regime. Nevertheless, the achieved conversion efficiency from the first green enhancement cavity generating XUV frequency combs already exceeds the results of the conversion efficiency in the experiments that introduced the Ti:sapphire and the Yb-fiber based systems (see chapter 6).

Even with these experimental realizations, it is possible to aim still higher. In principle, the experimental performance is mainly limited by the acquisition apparatus used in all presented experiments. Looking for a computer system with a larger working memory could extend the extreme resolution to a broader spectral region.

The analyzed spectra could be expanded by the implementation of spectrally broadening non-linear fibers in all shown experiments and chirped cavity mirrors in the experiment with the enhanced sensitivity (chapter 4) that compensate for the dispersion introduced by the other high reflecting cavity mirrors and the gas sample. In addition, the bandwidth of the phase locking loop for the cavity stabilization could be increased by an EOM what will enable to stabilize the following cavities on the highest resonance and, hence, would guarantee the broadest enhanced output. However, all these issues seem to be of vincible difficulty in their future implementation in the experiments since they all have been realized elsewhere but would have extended the development of the innovations presented here.

Only the $\text{Cr}^{2+}:\text{ZnSe}$ lasers used in the dual comb spectroscopic implementation in the MIR turned out to be only tolerably stable and would benefit of further development. These lasers are a very recent deployment and, hence, can still be improved. One could also think of alternative frequency comb sources in mid-infrared. For instance, there has most recently been a successful demonstration with pump light from an optical parametric oscillator injected into a micro toroid [113]. The MIR frequency comb is produced via third order Kerr nonlinearity in ultra-high Q ($\approx 10^9$) whispering-gallery-mode micro-resonators made out of crystalline MgF_2 . The generated comb spans more than 10 THz around the pumping wavelength of 2.5 μm of the OPO and the line spacing is observed to be 108

GHz. This large mode spacing potentially makes this new frequency comb generator an interesting tool for dual comb spectroscopy of dense media and for selective excitation since single comb lines may directly be accessed.

The further extension into the opposite wavelength direction, into the extreme ultraviolet, could be managed by the increase of higher driving intensities which in turn could be realized by a different cavity design (larger beam spots on the mirrors) and further development in the cavity mirror design for less sensitivities at high powers.

Since the UV experiment is running with a green cavity, it is planned to realize the first cavity enhanced dual comb spectroscopic experiment also in the visible wavelength range. In this region, spectroscopy with iodine could test the performance of the green dual comb spectrometer.

The most recent approach of adaptive sampling (see subsection *Extreme Resolutions* in chapter 3.2.3 and [90]) suggests an attractive alternative to the sophisticated and expensive method of stabilizing the combs onto a reference permitting every laboratory to tap the full potential of dual comb spectroscopy.

Appendix A

Specifications of the infrared cavity mirrors

Since the quality of the cavity mirrors is a crucial objective, their parameters in reflectivity and group delay dispersion are presented here.

Figure A.1 presents the theoretical reflectivity curves given by the manufacturer *Layertec* and the experimentally achieved data measured by a white light spectrometer. The actual transmission does not exactly follow the theoretical curves but this deviation can be neglected. The issue of constant transmission curves for the full laser wavelength range is much more important. As verified in the measurement, this is satisfactorily met for the important range of 1020 nm to 1080 nm (compare with the amplified laser spectrum in 4.2.2). Only the measured curve of the input coupler starts to deviate from the specified curve for longer wavelengths. The input coupler was measured at a later time when the large wavelength range white light spectrometer was not available any longer. The utilized spectrometer that was used here ranges only to 1100 nm which means a lower spectral intensity converging wavelengths and hence a larger error in the measurement.

The total group delay dispersion introduced by the cavity mirrors is depicted in figure A.2. The GDD values of six high reflecting mirrors (four plane and two concave mirrors), one input coupler with $R_{IC} = 99.74\%$ and one output coupler with $R_{OC} = 99.86\%$ add up to a total cavity dispersion that does not exceed +10 and -35 fs² for the amplified laser range (FWHM). In this calculation, the GDD introduced by the gas sample is not yet considered since it is different for each studied gas and chosen gas pressure.

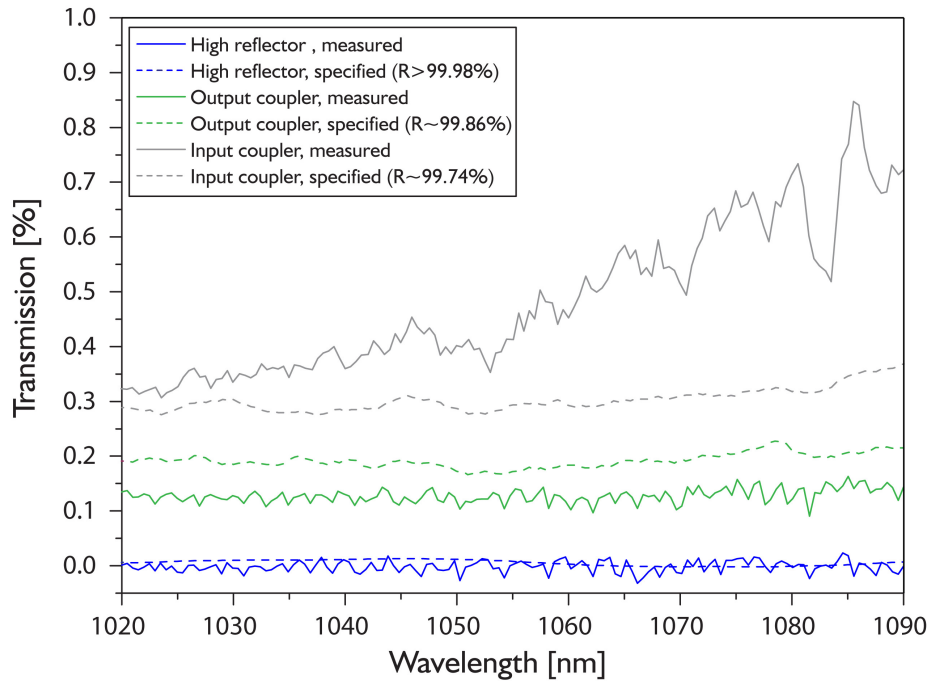


Figure A.1: Specified (dashed lines) and measured (continuous lines) reflectivity curves of the infrared cavity mirrors. Especially the crucial high reflector mirrors meet the specifications well.

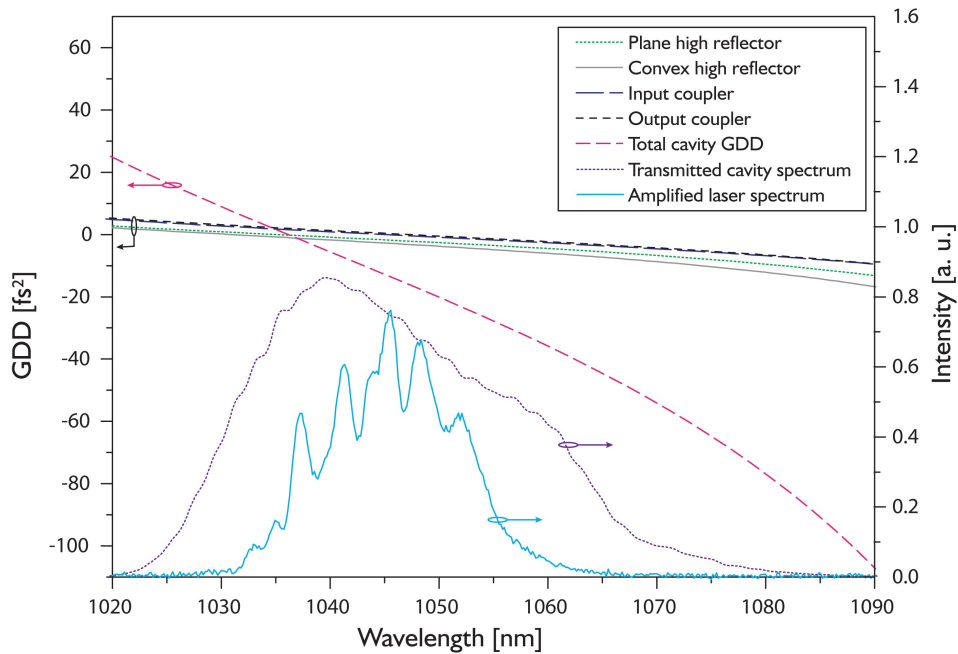


Figure A.2: Group delay dispersion curves of all cavity mirrors and the resulting total cavity dispersion (dotted violet). The amplified laser spectrum and the achieved cavity transmission are shown for comparison with the actually needed wavelength range.

Appendix B

Specifications of the green cavity mirrors

The green cavity could not achieve such a high finesse as the infrared cavity configuration. The reflectivity for the high reflectors were specified to be $\approx 99.998\%$ between 490 and 550 nm. Figure B.1 shows the specified and our measured reflectivity curves. While the input coupler's specifications are met well, the high reflectors show a higher transmission than specified. This becomes especially obvious in the logarithmically plotted inset in figure B.1: since the reflectivity is almost two orders of magnitude worse than the specified value, the overall losses are increased by the same amount limiting the power enhancement of the cavity. Since the total transmission value is very small, errors in the measurement can have a strong distorting effect. In order to prevent possible measuring faults, the transmission measurements were repeated 100 times for the high reflectors and 20 times for the input coupler. Figure B.1 shows the averaged curves out of the multiple scans with the white light spectrometer.

A general deterioration of high reflectors in the green wavelength region in comparison with high reflectors in the infrared region can be explained by the higher sensitivity of the surface quality: the smaller driving wavelength can be influenced also by smaller surface roughnesses.

The theoretical group delay dispersion (GDD) of the cavity mirrors was aimed to be much smaller compared to the infrared case (see figure B.2 a). This results in a total cavity GDD that is dominated by the Brewster window (see figure B.2 b). The cavity GDD is composed of the dispersion of 5 high reflecting mirrors, one input coupler and the Brewster plate, adding up to about 8.2 fs^2 for the full injected spectrum and, hence, reasonably small.

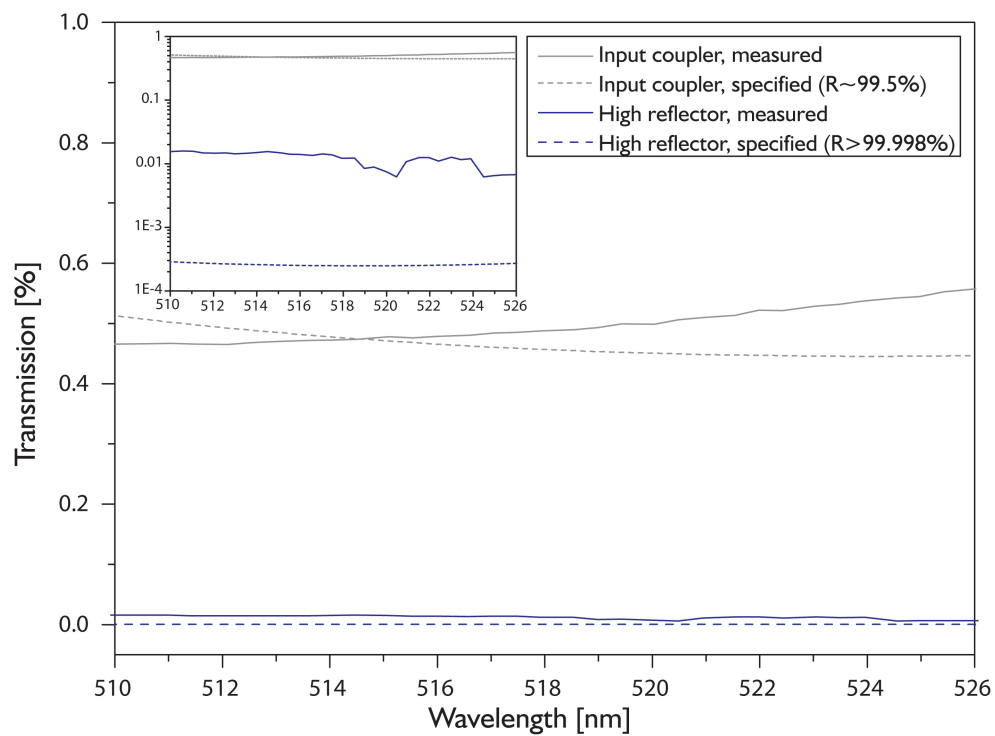


Figure B.1: Specified and measured reflectivity of the green cavity mirrors. The inset shows the identical curves logarithmically plotted disclosing even better the discrepancy of the actual reflectivity of the high reflectors from the specified values.

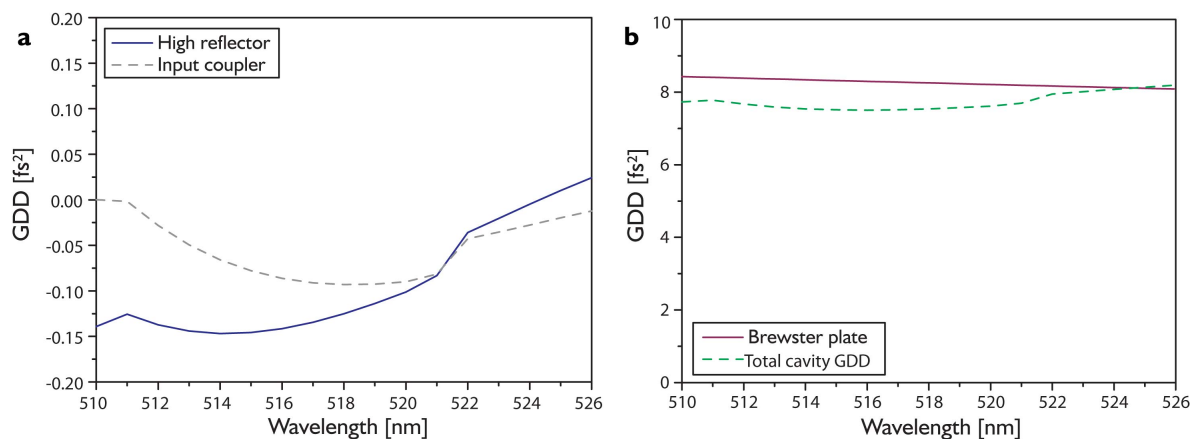


Figure B.2: Theoretical group delay dispersion of the cavity mirrors (a) and the Brewster plate (b). The resulting total GDD of the cavity is also shown (dashed green line).

Bibliography

- [1] C. W. Chou, D. B. Hume, J. C. J. Koelemeij, D. J. Wineland, and T. Rosenband, “Frequency comparison of two high-accuracy Al^+ optical clocks,” *Phys. Rev. Lett.* **104**, 070802 (2010).
- [2] T. Udem, J. Reichert, R. Holzwarth, and T. W. Hänsch, “Absolute optical frequency measurement of the cesium D_1 line with a mode-locked laser,” *Phys. Rev. Lett.* **82**, 3568–3571 (1999).
- [3] S. A. Diddams, T. Udem, K. R. Vogel, C. W. Oates, E. A. Curtis, R. S. Windeler, A. Bartels, J. C. Bergquist, and L. Hollberg, “A compact femtosecond-laser-based optical clockwork,” in “Laser Frequency Stabilization, Standards, Measurement, and Applications,” , vol. 4269, J. Hall and J. Ye, eds. (Proc. SPIE, 2001), pp. 77–83.
- [4] T. W. Hänsch, “The impact of frequency combs,” *Nature Photon.* **5**, 193 (2011).
- [5] Kungl. Vetenskapsakademien, “Quantum-mechanical theory of optical coherence - laser-based precision spectroscopy and optical frequency comb techniques,” Kungl. Vetenskapsakademien - The royal swedish academy of sciences, Advanced information on the Nobel Prize in Physics 2005 (2005).
- [6] T. Steinmetz, T. Wilken, C. Araujo-Hauck, R. Holzwarth, T. W. Hänsch, L. Pasquini, A. Manescau, S. D’Odorico, M. T. Murphy, T. Kentischer, W. Schmidt, and T. Udem, “Laser frequency combs for astronomical observations,” *Science* **321**, 1335–1337 (2008).
- [7] L. S. Rothman, I. E. Gordon, A. Barbe, C. Benner, P. F. Bernath, M. Birk, V. Boudon, L. R. Brown, A. Campargue, J. P. Champion, K. Chance, L. H. Coudert, V. Dana, V. M. Devi, S. Fally, J. M. Flaud, R. R. Gamache, A. Goldman, D. Jacquemart, I. Kleiner, N. Lacome, W. J. Lafferty, J. Y. Mandin, S. T. Massie, S. N.

- Mikhailenko, C. E. Miller, N. M. Ahmadi, O. V. Naumenko, A. V. Nikitin, J. Orphal, V. I. Perevalov, A. Perrin, A. P. Cross, C. P. Rinsland, M. Rotger, M. Simecková, M. A. H. Smith, K. Sung, S. A. Tashkun, J. Tennyson, R. A. Toth, A. C. Vandaele, and J. V. Auwera, “The HITRAN 2008 molecular spectroscopic database,” *Journal of Quantitative Spectroscopy and Radiative Transfer* **110** (2009).
- [8] J. Mandon, G. Guelachvili, and N. Picqué, “Fourier transform spectroscopy with a laser frequency comb,” *Nature Photon.* **3**, 99–102 (2009).
- [9] A. Michelson and E. Morley, “On the relative motion of the earth and the luminiferous ether,” *American Journal of Science* **203**, 333–345 (1887).
- [10] P. R. Griffiths and J. A. de Haseth, *Fourier Transform Infrared Spectrometry, Second Edition* (John Wiley and Sons, Inc., Hoboken, NJ, USA, 2007).
- [11] G. Guelachvili, “Near infrared wide-band spectroscopy with 27 MHz resolution,” *Appl. Opt.* **16**, 2097–2101 (1977).
- [12] G. Guelachvili, “High accuracy doppler-limited 10^6 samples Fourier transform spectroscopy,” *Appl. Opt.* **17**, 1322–1326 (1978).
- [13] R. C. M. Learner and A. P. Thorne, “Wavelength calibration of Fourier-transform emission spectra with applications to Fe I,” *J. Opt. Soc. Am. B* **5**, 2045–2059 (1988).
- [14] G. Guelachvili, “Distortions in Fourier spectra and diagnosis,” in “Spectrometric techniques,” , vol. 2, G. Vanasse, ed. (Academic Press New York, 1981).
- [15] R. E. Murphy and H. Sakai, “Application of Fourier spectroscopy technique to the study of relaxation phenomena,” in “Aspen International Conference on Fourier Spectroscopy (Air Force Cambridge Research Labs),” (1971), pp. 301–304.
- [16] N. Picqué and G. Guelachvili, “High-information time-resolved Fourier transform spectroscopy at work,” *Appl. Opt.* **39**, 3984–3990 (2000).
- [17] J. U. White, “Very long optical paths in air,” *J. Opt. Soc. Am.* **66**, 411–416 (1976).
- [18] M. Mérienne, A. Jenouvrier, C. Hermans, A. C. Vandalee, M. Carleer, C. Clebaux, P. H. Coheur, R. Colin, S. Fally, and M. Bach, “Water vapour line parameters in the 13000–9250 cm^{-1} region,” *J. Quant. Spectrosc. and Radiat. Transfer* **82**, 99–117 (2003).

- [19] S. N. Mikhailenko, V. L. G. Tyuterev, V. I. Starikov, K. K. Albert, B. P. Winnewisser, M. Winnewisser, G. Mellau, C. Camy-Peyret, R. Lanquetin, J.-M. Flaud, and J. W. Brault, “Water spectra in the region 13000-9250 cm^{-1} , extended analysis of $\nu_1 + \nu_2$, $\nu_2 + \nu_3$ and $3\nu_2$ bands and confirmation of highly excited states from flame spectra and from atmospheric long-path observations,” *J. Mol. Spectrosc.* **213**, 91–121 (2002).
- [20] Y. Ding, V. I. Perevalov, S. Tashkun, J.-L. Teffo, S. Hu, E. Bertseva, and A. Campargue, “Weak overtone transitions of N_2O around 1.05 μm by ICLAS-VECSEL,” *J. Mol. Spectrosc.* **220**, 80–86 (2003).
- [21] M. Ibrahimi, A. Babay, B. Lemoine, and F. Rohart, “Pressure-induced frequency lineshifts in the ν_2 band of ammonia: an experimental test of the Rydberg-Ritz principle,” *J. Mol. Spectrosc.* **193**, 277–284 (1999).
- [22] H. Bürger, J. Cosléou, J. Demaison, C. Gerke, H. Harder, H. Mäder, M. Paplewski, D. Papousek, K. Sarka, and J. K. G. Watson, “Radiofrequency, microwave, submillimeterwave, and high resolution infrared spectra of the $\nu_6 = 1$ vibrational state of CDF_3 ,” *J. Mol. Spectrosc.* **182**, 34–49 (1997).
- [23] P. L. Chapovsky, J. Cosléou, F. Herlemont, M. Khelkhal, and J. Legrand, “Separation and conversion of the nuclear spin isomers of ethylene,” *Chem. Phys. Lett.* **322**, 424–428 (2000).
- [24] G. M. Tino, “Testing the symmetrization postulate of quantum mechanics and the spin-statistics connection,” *Fortschr. Phys.* **48**, 537–543 (2000).
- [25] W. Pauli, “The connection between spin and statistics,” *Phys. Rev.* **58**, 716–722 (1940).
- [26] O. W. Greenberg, “Example of infinite statistics,” *Phys. Rev. Lett.* **64**, 705–708 (1990).
- [27] G. Modugno, M. Inguscio, and G. M. Tino, “Search for small violations of the symmetrization postulate for spin-0 particles,” *Phys. Rev. Lett.* **81**, 4790–4793 (1998).
- [28] A. Y. Ignatiev, “X-rays test the pauli exclusion principle,” *Rad. Phys. Chem.* **79**, 2090–2096 (2006).

- [29] A. Arking, "Absorption of solar energy in the atmosphere: discrepancy between the model and observations," *Science* **273**, 779–782 (1996).
- [30] R. Tipping and Q. Ma, "Theory of the water vapor continuum and validations," *Atmos. Res.* **36**, 69–94 (1995).
- [31] T. Kuhn, A. Bauer, M. Godon, S. Bühler, and K. Künzi, "Water vapour continuum: absorption measurements at 350 GHz and model calculations," *J. Quant. Spectrosc. and Radiat. Transfer* **74**, 545–562 (2002).
- [32] F. Thibault, V. Menoux, R. L. Doucen, L. Rosenmann, J.-M. Hartmann, and C. Boulet, "Infrared collision-induced absorption by O₂ near 6.4 μm for atmospheric applications: measurements and empirical modeling," *Appl. Opt.* **36**, 563–567 (1997).
- [33] A. Borysow and L. Frommhold, "Collision induced rototranslational absorption spectra on N₂-N₂ pairs for temperatures from 50 to 300 K," *The Astrophysical Journal* **311**, 1043–1057 (1986).
- [34] C. Boulet, "Collisional effects on spectral line-shapes," *C.R. Physique* **5**, 201–214 (2004).
- [35] R. Schermaul, R. C. M. Learner, A. A. D. Canas, J. W. Brault, O. L. Polyansky, D. Belmiloud, N. F. Zobov, and J. Tennyson, "Weak line water vapour spectra in the region 13200-15000 cm^{-1} ," *J. Mol. Spectrosc.* **211**, 169–178 (2002).
- [36] S. Spuler, M. Linne, A. Sappey, and S. Snyder, "Development of a cavity ringdown laser absorption spectrometer for detection of trace levels of mercury," *Appl. Opt.* **39**, 2480–2486 (2000).
- [37] D. Crisp, R. M. Atlas, F.-M. Breon, L. R. Brown, J. P. Burrows, P. Ciais, B. J. Connor, S. C. Doney, I. Y. Fung, D. J. Jacob, C. E. Miller, D. O'Brien, S. Pawson, J. Randerson, P. Rayner, R. J. Salawitch, S. Sander, B. Sen, Z. Kuang, B. Chudasama, G. Sprague, B. Weiss, R. Pollock, D. Kenyon, and S. Schroll, "The orbiting carbon observatory (OCO) mission," *Advances in Space Research* **34**, 700–709 (2003).
- [38] K. Skeldon, L. McMillan, C. Wyse, S. Monk, G. Gibson, C. Patterson, T. France, C. Longbottom, and M. Padgett, "Application of laser spectroscopy for measurement

- of exhaled ethane in patients with lung cancer,” *Respiratory Medicine* **100**, 300–306 (2006).
- [39] E. Wahl, S. Tan, S. Koulikov, B. Kharlamov, C. Rella, E. Crosson, D. Biswell, and B. Paldus, “Ultra-sensitive ethylene post-harvest monitor based on cavity ring-down spectroscopy,” *Opt. Exp.* **14**, 1673–1684 (2006).
- [40] D. S. Moore, “Instrumentation for trace detection of high explosives,” *Rev. Sci. Instrum.* **75**, 2499–2512 (2004).
- [41] H. H. Funke, M. W. Raynor, K. A. Bertness, and Y. Chen, “Detection of trace water vapor in high-purity phosphine using cavity ring-down spectroscopy,” *Appl. Spectrosc.* **61**, 419–423 (2007).
- [42] M. Todd, R. A. Provencal, T. G. Owano, B. A. Paldus, A. Kachanov, K. L. Vodopyanov, M. Hunter, S. L. Coy, J. I. Steinfeld, and J. T. Arnold, “Application of mid-infrared cavity-ringdown spectroscopy to trace explosives vapor detection using a broadly tunable (6–8 μm) optical parametric oscillator,” *Appl. Phys. B* **75**, 367–376 (2002).
- [43] H. Waechter, J. Mohn, B. Tuzson, L. Emmenegger, and M. W. Sigrist, “Determination of N_2O isotopomers with quantum cascade laser based absorption spectroscopy,” *Opt. Express* **16**, 9239–9244 (2008).
- [44] H. Schnatz, B. Lipphardt, J. Helmcke, F. Riehle, and G. Zinner, “First phase-coherent frequency measurement of visible radiation,” *Phys. Rev. Lett.* **76**, 18–21 (1996).
- [45] S. A. Diddams, D. J. Jones, J. Ye, S. T. Cundiff, J. L. Hall, J. K. Ranka, R. S. Windeler, R. Holzwarth, T. Udem, and T. W. Hänsch, “Direct link between microwave and optical frequencies with a 300 THz femtosecond laser comb,” *Phys. Rev. Lett.* **84**, 5102–5105 (2000).
- [46] R. Holzwarth, T. Udem, T. W. Hänsch, J. C. Knight, W. J. Wadsworth, and P. S. J. Russell, “Optical frequency synthesizer for precision spectroscopy,” *Phys. Rev. Lett.* **85**, 2264–2267 (2000).

- [47] T. Udem, J. Reichert, R. Holzwarth, and T. W. Hänsch, “Accurate measurement of large optical frequency differences with a mode-locked laser,” *Opt. Lett.* **24**, 881–883 (1999).
- [48] S. Diddams, L. Hollberg, L.-S. Ma, and L. Robertsson, “Femtosecond-laser-based optical clockwork with instability $\leq 6.3 \times 10^{-16}$ in 1 s,” *Opt. Lett.* **27**, 58–60 (2002).
- [49] N. R. Newbury and B. R. Washburn, “Theory of the frequency comb output from a femtosecond fiber laser,” *IEEE J. Quantum Electron* **41**, 1388–1402 (2005).
- [50] A. Ozawa, J. Rauschenberger, C. Gohle, M. Herrmann, D. R. Walker, V. Pervak, A. Fernandez, R. Graf, A. Apolonski, R. Holzwarth, F. Krausz, T. W. Hänsch, and T. Udem, “High harmonic frequency combs for high resolution spectroscopy,” *Phys. Rev. Lett.* **100**, 253901(1–4) (2008).
- [51] D. C. Yost, T. R. Schibli, and J. Ye, “Efficient output coupling of intracavity high-harmonic generation,” *Opt. Lett.* **33**, 1099–1101 (2008).
- [52] I. T. Sorokina, E. Sorokin, and T. Carrig, “Femtosecond pulse generation from a SESAM mode-locked $\text{Cr}^{2+}:\text{ZnSe}$ laser,” in “Conference on Lasers and Electro-Optics/Quantum Electronics and Laser Science Conference and Photonic Applications Systems Technologies,” (Optical Society of America, 2006), p. CMQ2.
- [53] S. M. Foreman, D. J. Jones, and J. Ye, “Flexible and rapidly configurable femtosecond pulse generation in the mid-IR,” *Opt. Lett.* **28**, 370–372 (2003).
- [54] Q. Fu, G. Mak, and H. M. V. Driel, “High-power, 62-fs infrared optical parametric oscillator synchronously pumped by a 76-MHz Ti:sapphire laser,” *Opt. Lett.* **17**, 1006–1008 (1992).
- [55] T. J. Kippenberg, S. M. Spillane, and K. J. Vahala, “Kerr-nonlinearity optical parametric oscillation in an ultrahigh-Q toroid microcavity,” *Phys. Rev. Lett.* **93**, 083904(1–4) (2004).
- [56] P. Del’Haye, A. Schliesser, O. Arcizet, T. Wilken, R. Holzwarth, and T. J. Kippenberg, “Optical frequency comb generation from a monolithic microresonator,” *Nature* **450**, 1214–1217 (2007).

- [57] J. Alnis, A. Matveev, N. Kolachevsky, T. Udem, and T. W. Hänsch, “Subhertz linewidth diode lasers by stabilization to vibrationally and thermally compensated ultralow-expansion glass fabry-pérot cavities,” *Phys. Rev. A* **77**, 053809 (2008).
- [58] R. J. Jones and J. Ye, “High-repetition-rate coherent femtosecond pulse amplification with an external passive optical cavity,” *Opt. Lett.* **29**, 2812–2814 (2004).
- [59] T. W. Hänsch and B. Couillaud, “Laser frequency stabilization by polarization spectroscopy of a reflecting reference cavity,” *Opt. Commun.* **35**, 441–444 (1980).
- [60] R. Drever, J. Hall, F. Kowalski, J. Hough, G. Ford, A. Munley, , and H. Ward, “Laser phase and frequency stabilization using an optical resonator,” *Appl. Phys. B* **31**, 97–105 (1983).
- [61] F. Helbing, G. Steinmeyer, J. Stenger, H. Telle, and U. Keller, “Carrier-envelope-offset dynamics and stabilization of femtosecond pulses,” *Applied Physics B: Lasers and Optics* **74**, s35–s42 (2002).
- [62] A. Apolonski, A. Poppe, G. Tempea, C. Spielmann, T. Udem, R. Holzwarth, T. W. Hänsch, and F. Krausz, “Controlling the phase evolution of few-cycle light pulses,” *Phys. Rev. Lett.* **85**, 740–743 (2000).
- [63] A. Poppe, R. Holzwarth, A. Apolonski, G. Tempea, C. Spielmann, T. Hänsch, and F. Krausz, “Few-cycle optical waveform synthesis,” *Applied Physics B: Lasers and Optics* **72**, 373–376 (2001).
- [64] D. Walker, T. Udem, C. Gohle, B. Stein, and T. Hänsch, “Frequency dependence of the fixed point in a fluctuating frequency comb,” *Applied Physics B: Lasers and Optics* **89**, 535–538 (2007).
- [65] V. Gerginov, C. E. Tanner, S. A. Diddams, A. Bartels, and L. Hollberg, “High-resolution spectroscopy with a femtosecond laser frequency comb,” *Opt. Lett.* **30**, 1734–1736 (2005).
- [66] P. Fendel, S. D. Bergeson, T. Udem, and T. W. Hänsch, “Two-photon frequency comb spectroscopy of the 6s-8s transition in cesium,” *Opt. Lett.* **32**, 701–703 (2007).
- [67] Y. Baklanov and V. Chebotayev, “Narrow resonances of two-photon absorption of super-narrow pulses in a gas,” *Applied Physics A: Materials Science and Processing* **12**, 97–99 (1977).

- [68] R. Teets, J. Eckstein, and T. W. Hänsch, “Coherent two-photon excitation by multiple light pulses,” *Phys. Rev. Lett.* **38**, 760–764 (1977).
- [69] G. Hagel, C. Nesi, L. Jozefowski, C. Schwob, F. Nez, and F. Biraben, “Accurate measurement of the frequency of the 6s-8s two-photon transitions in cesium,” *Opt. Commun.* **160**, 1–4 (1999).
- [70] M. J. Thorpe, K. D. Moll, R. J. Jones, B. Safdi, and J. Ye, “Broadband cavity ringdown spectroscopy for sensitive and rapid molecular detection,” *Science* **311**, 1595–1599 (2006).
- [71] M. J. Thorpe, D. Balslev-Clausen, M. S. Kirchner, and J. Ye, “Cavity-enhanced optical frequency comb spectroscopy: application to human breath analysis,” *Opt. Express* **16**, 2387–2397 (2008).
- [72] F. Adler, M. J. Thorpe, K. C. Cossel, and J. Ye, “Cavity-enhanced direct frequency comb spectroscopy: Technology and applications,” *Annual Review of Analytical Chemistry* **3**, 175–205 (2010).
- [73] C. Gohle, B. Stein, A. Schliesser, T. Udem, and T. Hänsch, “Frequency comb Vernier spectroscopy for broadband, high-resolution, high-sensitivity absorption and dispersion spectra,” *Phys. Rev. Lett.* **99**, 263902(1–4) (2007).
- [74] S. Diddams, L. Hollberg, and V. Mbele, “Molecular fingerprinting with the resolved modes of a femtosecond laser frequency comb,” *Nature* **445**, 627–630 (2007).
- [75] S.-J. Lee, B. Widiyatmoko, M. Kouroggi, and M. Ohtsu, “Ultrahigh scanning speed optical coherence tomography using optical frequency comb generators,” *Japanese Journal of Applied Physics* **40**, L878–L880 (2001).
- [76] S. Schiller, “Spectrometry with frequency combs,” *Opt. Lett.* **27**, 766–768 (2002).
- [77] I. Coddington, W. C. Swann, and N. R. Newbury, “Coherent multiheterodyne spectroscopy using stabilized optical frequency combs,” *Phys. Rev. Lett.* **100**, 013902(1–4) (2008).
- [78] A. Schliesser, M. Brehm, F. Keilmann, and D. van der Weide, “Frequency-comb infrared spectrometer for rapid, remote chemical sensing,” *Opt. Express* **13**, 9029–9038 (2005).

- [79] T. Yasui, E. Saneyoshi, and T. Araki, “Asynchronous optical sampling terahertz time-domain spectroscopy for ultrahigh spectral resolution and rapid data acquisition,” *Applied Physics Letters* **87**, 061101 (2005).
- [80] P. Giaccari, J.-D. Deschênes, P. Saucier, J. Genest, and P. Tremblay, “Active Fourier-transform spectroscopy combining the direct RF beating of two fiber-based mode-locked lasers with a novel referencing method,” *Opt. Express* **16**, 4347–4365 (2008).
- [81] P. Jacquet, J. Mandon, B. Bernhardt, R. Holzwarth, G. Guelachvili, T. W. Hänsch, and N. Picqué, “Frequency comb Fourier transform spectroscopy with kHz optical resolution,” in “Fourier Transform Spectroscopy,” (Optical Society of America, 2009), p. FMB2.
- [82] C. E. Shannon, “Communication in the presence of noise,” reprint in *Proc. IEEE* **86**, 447–457 (1998).
- [83] K. Tamura, J. Jacobson, E. P. Ippen, H. A. Haus, and J. G. Fujimoto, “Unidirectional ring resonators for self-starting passively mode-locked lasers,” *Opt. Lett.* **18**, 220–222 (1993).
- [84] MenloSystems, “Test report on the oscillators SN060+LH106 and SN058+LH107,” Tech. rep., MenloSystems GmbH Martinsried, Germany (2008).
- [85] B. Bernhardt, T. W. Hänsch, and R. Holzwarth, “Implementation and characterization of a stable optical frequency distribution system,” *Opt. Express* **17**, 16849–16860 (2009).
- [86] S. T. Cundiff and J. Ye, “Phase stabilization of mode-locked lasers,” *Journal of modern optics* **52**, 201–219 (2005).
- [87] J. Stenger, H. Schnatz, C. Tamm, and H. R. Telle, “Ultraprecise measurement of optical frequency ratios,” *Phys. Rev. Lett.* **88**, 073601 (2002).
- [88] J. Mandon, “Spectroscopie de Fourier par peignes de fréquences femtosecondes,” Ph.D. thesis, Université Paris Sud XI, U.F.R. Scientifique d’Orsay, Laboratoire de Photophysique Moléculaire (2009).
- [89] F. Helbing, G. Steinmeyer, and U. Keller, “Carrier-envelope offset phase-locking with attosecond timing jitter,” *Selected Topics in Quantum Electronics, IEEE Journal of* **9**, 1030 – 1040 (2003).

- [90] T. Ideguchi, A. Poisson, G. Guelachvili, T. W. Hänsch, and N. Picqué, “Dual-comb spectroscopy with adaptive sampling,” in “Conference on Lasers and Electro-Optics,” (2011).
- [91] Agilent, “Accuracy calculator for frequency counters,” <http://www.home.agilent.com> (2004).
- [92] G. Guelachvili, “Experimental Doppler-limited spectra of the ν_2 bands of H_2^{16}O , H_2^{17}O , H_2^{18}O , and HDO by Fourier-transform spectroscopy: secondary wave-number standards between 1066 and 2296 cm^{-1} ,” *J. Opt. Soc. Am.* **73**, 137–150 (1983).
- [93] M. S. Burberry, J. A. Morrell, A. C. Albrecht, and R. L. Swofford, “Local mode overtone intensities of C-H stretching modes in alkanes and methyl substituted benzenes,” *J. Chem. Phys.* **70**, 5522–5526 (1979).
- [94] B. Bernhardt, A. Ozawa, P. Jacquet, M. Jacquy, Y. Kobayashi, T. Udem, R. Holzwarth, G. Guelachvili, T. W. Hänsch, and N. Picqué, “Cavity-enhanced dual-comb spectroscopy,” *Nature Photonics* **4**, 55–57 (2010).
- [95] D. Höfling, “Ytterbium-Faserlaser für Frequenzkamm-Applikationen,” Master’s thesis, Technische Universität Berlin (2008).
- [96] L. F. Mollenauer, R. H. Stolen, and J. P. Gordon, “Experimental observation of picosecond pulse narrowing and solitons in optical fibers,” *Phys. Rev. Lett.* **45**, 1095–1098 (1980).
- [97] F. O. Ilday, J. R. Buckley, W. G. Clark, and F. W. Wise, “Self-similar evolution of parabolic pulses in a laser,” *Phys. Rev. Lett.* **92**, 213902 (2004).
- [98] M. Herman, T. Huet, and M. Vervloet., “Spectroscopy and vibrational couplings in the $3\nu_3$ region of acetylene,” *Mol. Phys.* **66**, 333–353 (1989).
- [99] P. Irwin, S. Calcutt, K. Sihra, F. Taylor, A. Weir, J. Ballard, and W. Johnston, “Band parameters and k coefficients for self-broadened ammonia in the range 4000–11 000 cm^{-1} ,” *Journal of Quantitative Spectroscopy and Radiative Transfer* **62**, 193 – 204 (1999).
- [100] I. Kleiner, G. Tarrago, C. Cottaz, L. Sagui, L. R. Brown, R. L. Poynter, H. M. Pickett, P. Chen, J. C. Pearson, R. L. Sams, G. A. Blake, S. Matsuura, V. Nemtchinov,

- P. Varanasi, L. Fusina, and G. D. Lonardo, “NH₃ and PH₃ line parameters: the 2000 HITRAN update and new results,” *Journal of Quantitative Spectroscopy and Radiative Transfer* **82**, 293 – 312 (2003). The HITRAN Molecular Spectroscopic Database: Edition of 2000 Including Updates of 2001.
- [101] A. Ozawa, “Frequency combs in the extreme ultraviolet,” Ph.D. thesis, Ludwig-Maximilians-Universität (2009).
- [102] F. Keilmann, C. Gohle, and R. Holzwarth, “Time-domain mid-infrared frequency-comb spectrometer,” *Opt. Lett.* **29**, 1542–1544 (2004).
- [103] P. Maddaloni, P. Malara, G. Gagliardi, and P. D. Natale, “Mid-infrared fibre-based optical comb,” *New Journal of Physics* **8**, 262 (2006).
- [104] F. Adler, K. C. Cossel, M. J. Thorpe, I. Hartl, M. E. Fermann, and J. Ye, “Phase-stabilized, 1.5 W frequency comb at 2.8–4.8 μm ,” *Opt. Lett.* **34**, 1330–1332 (2009).
- [105] M. El-Amraoui, J. Fatome, J. C. Jules, B. Kibler, G. Gadret, C. Fortier, F. Smektala, I. Skripatchev, C. Polacchini, Y. Messaddeq, J. Troles, L. Brilland, M. Szpulak, and G. Renversez, “Strong infrared spectral broadening in low-loss As-S chalcogenide suspended core microstructured optical fibers,” *Opt. Express* **18**, 4547–4556 (2010).
- [106] E. Sorokin, I. T. Sorokina, J. Mandon, G. Guelachvili, and N. Picqué, “Sensitive multiplex spectroscopy in the molecular fingerprint 2.4 μm region with a Cr²⁺:ZnSe femtosecond laser,” *Opt. Express* **15**, 16540–16545 (2007).
- [107] B. Bernhardt, E. Sorokin, P. Jacquet, R. Thon, T. Becker, I. T. Sorokina, N. Picqué, and T. W. Hänsch, “Mid-infrared dual-comb spectroscopy with 2.4 μm Cr²⁺:ZnSe femtosecond lasers,” *Applied Physics B-lasers and Optics* **100**, 3–8 (2010).
- [108] V. L. Kalashnikov and E. Sorokin, “Soliton absorption spectroscopy,” *Phys. Rev. A* **81**, 033840 (2010).
- [109] E. Sorokin and I. T. Sorokina, “Femtosecond operation and random quasi-phase-matched self-doubling of ceramic Cr²⁺:ZnSe laser,” in “Conference on Lasers and Electro-Optics,” (Optical Society of America, 2010), p. CTuGG2.
- [110] Z. Chen, A. J. Taylor, and A. Efimov, “Coherent mid-infrared broadband continuum generation in non-uniform ZBLAN fiber taper,” *Opt. Express* **17**, 5852–5860 (2009).

- [111] C. Erny, K. Moutzouris, J. Biegert, D. Kühlke, F. Adler, A. Leitenstorfer, and U. Keller, “Mid-infrared difference-frequency generation of ultrashort pulses tunable between 3.2 and 4.8 μm from a compact fiber source,” *Opt. Lett.* **32**, 1138–1140 (2007).
- [112] F. Adler, P. Masłowski, A. Foltynowicz, K. C. Cossel, T. C. Briles, I. Hartl, and J. Ye, “Mid-infrared fourier transform spectroscopy with a broadband frequency comb,” *Opt. Express* **18**, 21861–21872 (2010).
- [113] C. Y. Wang, T. Herr, P. Del’Haye, A. Schliesser, R. Holzwarth, T. W. Hänsch, N. Picqué, and T. J. Kippenberg, “Mid-infrared frequency combs based on microresonators,” in “Conference on Lasers and Electro-Optics Europe Postdeadline Papers,” (Optical Society of America, 2011), p. PDPA4.
- [114] L. Nahon, “SU5 on SOLEIL: Updated scientific case and aps of the transferred beamline,” Tech. rep., French national Synchrotron facility SOLEIL (2002).
- [115] A. P. Thorne, C. J. Harris, I. Wynne-Jones, R. C. M. Learner, and G. Cox, “A Fourier transform spectrometer for the vacuum ultraviolet: design and performance,” *Journal of Physics E: Scientific Instruments* **20**, 54 (1987).
- [116] A. P. Thorne, G. Cox, R. C. M. Learner, P. L. Smith, and W. H. Parkinson, “Fourier transform spectroscopy at vacuum ultraviolet wavelengths,” *Astron. Soc. Pac. Conf. Ser.* **81**, 235–236 (1995).
- [117] N. de Oliveira, M. Roudjane, D. Joyeux, D. Phalippou, J.-C. Rodier, and L. Nahon, “High-resolution broad-bandwidth Fourier-transform absorption spectroscopy in the VUV range down to 40 nm,” *Nature Photon.* **5**, 149–153 (2011).
- [118] <http://www.synchrotron-soleil.fr/>, “French national synchrotron facility SOLEIL,” (2011).
- [119] P. Rupper and F. Merkt, “Intense narrow-bandwidth extreme ultraviolet laser system tunable up to 20 eV,” *Review of Scientific Instruments* **75**, 613–622 (2004).
- [120] L. Piticco, F. Merkt, A. A. Cholewinski, F. R. McCourt, and R. J. L. Roy, “Rotational structure and potential energy function of the $X0^+$ ground electronic state of ArXe,” *Journal of Molecular Spectroscopy* **264**, 83 – 93 (2010).

- [121] M. Grütter, J. M. Michaud, and F. Merkt, “Photoelectron spectroscopic study of the $E \otimes e$ Jahn–Teller effect in the presence of a tunable spin–orbit interaction. I. Photoionization dynamics of methyl iodide and rotational fine structure of CH_3I^+ and CD_3I^+ ,” *The Journal of Chemical Physics* **134**, 054308 (2011).
- [122] C. Gohle, T. Udem, M. Herrmann, J. Rauschenberger, R. Holzwarth, H. A. Schuessler, F. Krausz, and T. W. Hänsch, “A frequency comb in the extreme ultraviolet,” *Nature* **436**, 234–237 (2005).
- [123] S. Witte, R. T. Zinkstok, W. Ubachs, W. Hogervorst, and K. S. E. Eikema, “Deep-ultraviolet quantum interference metrology with ultrashort laser pulses,” *Science* **307**, 400–403 (2005).
- [124] J. Lee, J. Paul, and J. Jones, “High power femtosecond laser system for intracavity high harmonic generation,” in “Conference on Lasers and Electro-Optics,” (Optical Society of America, 2010), p. CThQ2.
- [125] A. Ruehl, M. E. Fermann, I. Hartl, A. Cingöz, D. C. Yost, and J. Ye, “High power fiber laser frequency combs for xuv spectroscopy,” in “Fiber Laser Applications,” (Optical Society of America, 2011), p. FWB4.
- [126] R. T. Zinkstok, S. Witte, W. Ubachs, W. Hogervorst, and K. S. E. Eikema, “Frequency comb laser spectroscopy in the vacuum-ultraviolet region,” *Phys. Rev. A* **73**, 061801 (2006).
- [127] D. Z. Kandula, C. Gohle, T. J. Pinkert, W. Ubachs, and K. S. E. Eikema, “Extreme ultraviolet frequency comb metrology,” *Phys. Rev. Lett.* **105**, 063001 (2010).
- [128] <http://www.munich-photonics.de/>, “Munich centre for advanced photonics map - cluster of excellence of the German Research Foundation (DFG),” (2011).
- [129] C. Gohle, “A coherent frequency combs in the extreme ultraviolet,” Ph.D. thesis, Ludwig-Maximilians-Universität (2006).
- [130] A. McPherson, G. Gibson, H. Jara, U. Johann, T. S. Luk, I. A. McIntyre, K. Boyer, and C. K. Rhodes, “Studies of multiphoton production of vacuum-ultraviolet radiation in the rare gases,” *J. Opt. Soc. Am. B* **4**, 595–601 (1987).

- [131] J. L. Krause, K. J. Schafer, and K. C. Kulander, “High-order harmonic generation from atoms and ions in the high intensity regime,” *Phys. Rev. Lett.* **68**, 3535–3538 (1992).
- [132] P. B. Corkum, “Plasma perspective on strong field multiphoton ionization,” *Phys. Rev. Lett.* **71**, 1994–1997 (1993).
- [133] K. C. Kulander, K. J. Schafer, and J. L. Krause, “Super intense laser atom physics,” in “NATO Advanced Study Institute, Series B,” , vol. 316 (Plenum Press, New York, 1993), p. 95.
- [134] M. Lewenstein, P. Balcou, M. Y. Ivanov, A. L’Huillier, and P. B. Corkum, “Theory of high-harmonic generation by low-frequency laser fields,” *Phys. Rev. A* **49**, 2117–2132 (1994).
- [135] J. G. Eden, “High-order harmonic generation and other intense optical field-matter interactions: review of recent experimental and theoretical advances,” *Progress in Quantum Electronics* **28**, 197 – 246 (2004).
- [136] E. Constant, D. Garzella, P. Breger, E. Mével, C. Dorrer, C. Le Blanc, F. Salin, and P. Agostini, “Optimizing high harmonic generation in absorbing gases: Model and experiment,” *Phys. Rev. Lett.* **82**, 1668–1671 (1999).
- [137] A. Paul, R. Bartels, R. Tobey, H. Green, S. Weiman, I. Christov, M. Murnane, H. Kapteyn, and S. Backus, “Quasi-phase-matched generation of coherent extreme-ultraviolet light,” *Nature* **421**, 51–54 (2003).
- [138] P. Balcou, C. Cornaggia, A. S. L. Gomes, L. A. Lompre, and A. L’Huillier, “Optimizing high-order harmonic generation in strong fields,” *Journal of Physics B: Atomic, Molecular and Optical Physics* **25**, 4467 (1992).
- [139] A. L’Huillier, K. J. Schafer, and K. C. Kulander, “Theoretical aspects of intense field harmonic generation,” *Journal of Physics B: Atomic, Molecular and Optical Physics* **24**, 3315 (1991).
- [140] J. Jones, “Intracavity high harmonic generation with fs frequency combs,” in “High Intensity Lasers and High Field Phenomena,” (Optical Society of America, 2011), p. HFB5.

- [141] T. Ditmire, J. K. Crane, H. Nguyen, L. B. DaSilva, and M. D. Perry, “Energy-yield and conversion-efficiency measurements of high-order harmonic radiation,” *Phys. Rev. A* **51**, R902–R905 (1995).
- [142] E. L. Falcão-Filho, V. M. Gkortsas, A. Gordon, and F. X. Kärtner, “Analytic scaling analysis of high harmonic generation conversion efficiency,” *Opt. Express* **17**, 11217–11229 (2009).
- [143] K. Boller, R.-P. Haelbich, H. Hogrefe, W. Jark, and C. Kunz, “Investigation of carbon contamination of mirror surfaces exposed to synchrotron radiation,” *Nuclear Instruments and Methods in Physics Research* **208**, 273 – 279 (1983).
- [144] K. Yamada, T. Yamazaki, N. Sei, R. Suzuki, T. Ohdaira, T. Shimizu, M. Kawai, M. Yokoyama, T. Mikado, T. Noguchi, S. Sugiyama, and H. Ohgaki, “Saturation of cavity-mirror degradation in the UV FEL,” *Nuclear Instruments and Methods in Physics Research Section A: Accelerators, Spectrometers, Detectors and Associated Equipment* **393**, 44 – 49 (1997). *Free Electron Lasers 1996*.
- [145] <http://de.wikibooks.org>, “Tabellensammlung Chemie/ Enthalpie und Bindungsenergie,” (2011).
- [146] F. Dageförde and R. Gruehn, “Zum chemischen Transport von ZrO_2 und HfO_2 mit den Transportmitteln Cl_2 und $TeCl_4$,” *Zeitschrift für anorganische und allgemeine Chemie* **611**, 103–106 (1992).
- [147] E. Moeller, *Handbuch Konstruktionswerkstoffe - Auswahl, Eigenschaften, Anwendung* (Hanser Verlage, 2007).
- [148] E. D. Palik, “Handbook of optical constants of solids,” Academic Press, New York **1** (1991).
- [149] A. Ozawa, A. Vernaleken, W. Schneider, I. Gotlibovych, T. Udem, and T. W. Hänsch, “Non-collinear high harmonic generation: a promising outcoupling method for cavity-assisted XUV generation,” *Opt. Express* **16**, 6233–6239 (2008).
- [150] K. D. Moll, R. J. Jones, and J. Ye, “Output coupling methods for cavity-based high-harmonic generation,” *Opt. Express* **14**, 8189–8197 (2006).

- [151] J. Weitenberg, P. Rußbüldt, T. Eidam, and I. Pupeza, “Transverse mode tailoring in a quasi-imaging high-finesse femtosecond enhancement cavity,” *Opt. Express* **19**, 9551–9561 (2011).
- [152] B. Henke, E. Gullikson, and J. Davis, “X-ray interactions: photoabsorption, scattering, transmission, and reflection at $E=50\text{--}30000$ eV, $Z=1\text{--}92$,” *Atomic Data and Nuclear Data Tables* Vol. **54**, 181–342 (1993).
- [153] D. Freeman, K. Yoshino, J. Esmond, and W. Parkinson, “High resolution absorption cross section measurements of SO_2 at 213 K in the wavelength region 172–240 nm,” *Planetary Space Science* **32**, 1125–1134 (1984).
- [154] K. Yoshino, D. Freeman, and W. Parkinson, “High resolution absorption cross section measurements of N_2O at 295–299 K in the wavelength region 170–222 nm,” *Planetary Space Science* **32**, 1219–1222 (1984).
- [155] K. Yoshino, W. Parkinson, K. Ito, and T. Matsui, “Absolute absorption cross-section measurements of Schumann-Runge continuum of O_2 at 90 and 295 K,” *Journal of Molecular Spectroscopy* **229**, 238 – 243 (2005).
- [156] K. Yoshino, D. Freeman, J. Esmond, and W. Parkinson, “Absolute absorption cross-section measurements of ozone in the wavelength region 238–335 nm and the temperature dependence,” *Planetary and Space Science* **36**, 395 – 398 (1988).
- [157] P. L. Smith, K. Yoshino, W. Parkinson, K. Ito, and G. Stark, “High-resolution, VUV (147–201 nm) photoabsorption cross sections for C_2H_2 at 195 and 295 K,” *Journal of Geophysical Research* **96**, 17529–17533 (1991).
- [158] V. Batteiger, private communication (2011).
- [159] A. Ozawa and Y. Kobayashi, “Intracavity high harmonic generation driven by Yb-fiber based MOPA system at 80MHz repetition rate,” in “Conference on Lasers and Electro-Optics,” (Optical Society of America, 2011), p. CThB4.
- [160] NIST, “National Institute for Standards and Technology - Far Ultraviolet Physics Group / Synchrotron Ultraviolet Radiation Facility SURF III,” <http://physics.nist.gov/MajResFac/SURF/SURF/sr.html> (2011).

-
- [161] A. L. Cavalieri, E. Goulielmakis, B. Horvath, W. Helml, M. Schultze, M. Fieß, V. Per-
vak, L. Veisz, V. S. Yakovlev, M. Uiberacker, A. Apolonski, F. Krausz, and R. Kien-
berger, “Intense 1.5-cycle near infrared laser waveforms and their use for the gener-
ation of ultra-broadband soft-x-ray harmonic continua,” *New Journal of Physics* **9**,
242 (2007).
- [162] Bruker, “IFS 125,” <http://www.brukeroptics.com/ifs125.html?&L=> (2011).

Curriculum Vitae

Birgitta Catarina Bernhardt
Max-Planck-Institute for Quantum Optics
Hans-Kopfermann-Straße 1
85748 Garching
Tel.: 0049 89 32905-295
Birgitta.Bernhardt@mpq.mpg.de

Personal Data

Date of birth: 05.04.1981
Place of birth: Erlangen
Citizenship: German
Marital status: unmarried

Education

- 11/2006 - present Graduate student in the group of Theodor W. Hänsch at the Max-Planck-Institute for Quantum Optics, Garching, Germany
- 07/2005 - 06/2006 Diploma Thesis in the group of Theodor W. Hänsch at the Max-Planck-Institute for Quantum Optics, Garching, Germany
Subject: Implementation and characterization of a stable frequency distribution system
- 10/2000 - 07/2005 Undergraduate studies in physics at the Ludwig-Maximilians-Universität München, Germany
Focused Studies: Laser Physics and Quantum Optics
- 06/2000 Abitur (high school graduation) in Munich

Extra-educational experience

- 01/2005 - 07/2006 Working student at MenloSystems GmbH
- 09/2004 - 10/2004 Working student in the group of Karl-Ludwig Kompa at the Max-Planck-Institute for Quantum Optics
- 08/2003 - 10/2003 Working student in the group of Karl-Ludwig Kompa at the Max-Planck-Institute for Quantum Optics
- 08/2000 - 09/2000 Temporary personnel at the European Patent Office, Munich

Acknowledgments

Bei **Theodor W. Hänsch** bedanke ich mich sehr für die Möglichkeit in seiner Gruppe diese spannende Doktorarbeit gemacht haben zu dürfen, für all die Freiheiten und die guten Einfälle, die mir auf Durststrecken neue Anstöße gegeben haben, aber vor allem auch für die ansteckende Begeisterung, die er immer wieder für die „einfachen“ optischen Phänomene im Labor gezeigt hat, zum Beispiel bei den flitzenden Staubteilchen im grünen Überhöhungsresonator.

J'ai eu la meilleure chance avec l'arrivée de **Nathalie Picqué**. J'ai eu le plaisir de passer la plupart du temps avec elle dans le laboratoire, au déjeuner et dans les pauses-café, par quoi je pourrais apprendre si beaucoup de leur. Entretiens elle signifie une bonne amie pour moi (je suis désolée pour mon français).

Thomas und **Ronald** danke ich für ihre Expertise in allen Frequenzkammfragen und für die Ungebundenheiten, die ich beim Experimentieren hatte.

A special *domo arigato* is going to **Akira** from whom I learned the most about enhancement cavities and who enriched our group so much with his nice nature which includes his open mind for the Bavarian way of living.

Andreas möchte ich danken, für seine Hilfe bei der finalen Harmonischenmessung, für das Durchsehen des XUV-Kapitels und dass er mich so schön als Freddy in Kathas Pulli durch den Flur gejagt hat.

Ich möchte mich bei **Ioachim, Jan** und **Johannes** bedanken, den nettesten Diskussionspartnern, nicht nur bezüglich Cavities.

Katha danke ich, dass sie eine so liebe Bürogenossin war und ist, mit der ich schon während des Studiums viel erleben und während der letzten Jahre auch filmisch kreativ werden durfte.

Danke an **Elisabeth** und **Sascha**, meine Lieblingslaborgenossen. Alleine Musik hören im Labor macht mir ohne Euch gar keinen Spaß, habe ich festgestellt.

Christian, Peter, Max, Chris G., Guido, Tino, Sebastian, Tobi, Tobias und **Randolf** waren nicht nur immer wieder perfekte Gentlemen in ihrer Hilfsbereitschaft, mit ihnen war's auch immer lustig im Labor, auf Parties und im Biergarten.

Arthur, Janis und **Camille** danke ich auch für ihre wiederholte Hilfe und diverse lustige Unterhaltungen.

I want to especially thank **Albert, Remi, Pascal, Georg, Jens, Tobias, Stefan** and **Christine** for nice conference trips or even post-conference trips. Sad that only a few of

you are left at the MPQ.

Thanks to **Takuro**, **Axel** and **Antonin**, the "freshmen", who match well into the sympathetic group.

Peter und seinen Jungs danke ich genauso für ihre liebe Hilfsbereitschaft und ihren Humor.

Wolfgang, **Charly** und der **MPQ Werkstatt** gebührt besonderer Dank für die vielen Werkstücke, die ein Experiment letztendlich zum Laufen bringen, zusammen mit den Photodioden, Lockboxen etc. von **Helmut**, Danke!

Dem **Einkauf** und der **Warenannahme** danke ich genauso für die immerwährend schnellen Bestellungen/Lieferungsbescheide diverser Komponenten, die für die Experimente unerlässlich waren.

Bei **Frau Gschwendtner** und **Frau Hermann** möchte ich mich für die durchgehend freundliche Hilfe bei allen bürokratischen Angelegenheiten bedanken.

Bei der **gesamten Belegschaft des MPQs** bedanke ich mich für die schöne Atmosphäre am Institut und das freudige Mitwirken bei unseren Weihnachtsfilmen, die die beste „ausgleichende“ Nebentätigkeit darstellte, die ich mir so vorstellen kann.

Über die Jahre ist mir das Institut sehr ans Herz gewachsen und ich freue mich besonders, dass ich in **Martin**, **Ivanka**, **Wolfi**, **Reini** und **Tom** während meiner Doktorarbeit so liebe Freunde am MPQ gefunden habe.